The Effects of Laser and Electron Beam Spot Size in Additive Manufacturing Processes

Submitted in partial fulfillment of the requirements for
the degree of
Doctor of Philosophy
In
Mechanical engineering

Zachary Ryan Francis

B.S. Mechanical Engineering, The Pennsylvania State University
M.S. Mechanical Engineering, Carnegie Mellon University

Carnegie Mellon University
Pittsburgh, PA

May 2017

Dedication

This dissertation is dedicated to:

To my parents,

John and Dorothy

and

my fiancé, Kelly

Acknowledgements

The completion of this thesis was made possible through the support of many people known both academically and personally. I would like to thank my advisor, Dr. Jack Beuth, for advice and guidance throughout my pursuits at Carnegie Mellon University. I would also like to thank the other members of my committee, Dr. Fred Higgs, Dr. Jonathan Malen, and Dr. Tony Rollett. Their suggestions and input have shaped and improved the work in this dissertation. I would also like to acknowledge members of the staff in the department of Mechanical Engineering for their support.

I am also grateful to the organizations providing financial support throughout my Ph.D. This research was funded by America Makes (The National Additive Manufacturing Innovation Institute), and Sandia National Laboratories.

I would like to thank the members of Dr. Beuth's research group who have helped shape my work: Brian Fisher, Jason Fox, Joy Gockel, Colt Mongomery, Sneha Narra, and Luke Scime. They have all provided valuable input and helped overcome difficulties that were presented by the research. I would also like to extend a special thanks to Sneha Narra who helped plan and run countless experiments.

Collaborators in various organizations have also helped me progress my research by providing important process insight. I must acknowledge collaborators Ted Reutzel of Penn State ARL, Scott Stecker of Sciaky Inc., and Bradley Jared of Sandia National Laboratories. They have helped organize and set up many experiments that helped build the findings of this thesis.

I would like to thank my fiancé, Kelly, who has supported me throughout my time at Carnegie Mellon. Her loving support has made my pursuit of a Ph.D. much easier, and her great friendship has made my time in grad school much more enjoyable.

Last, but not least, I would like to thank my parents, John and Dorothy. They have been supporting my academic endeavors for over 20 years, and have been an integral part to my success both inside and outside of the classroom. Without their guidance and encouragement, this work would not be possible.

Abstract

In this work, melt pool size in process mapped in power-velocity space for multiple processes and alloys. In the electron beam wire feed and laser powder feed processes, melt pool dimensions are then related to microstructure in the Ti-6Al-4V alloy. In the electron beam wire feed process, work by previous authors that related prior beta grain size to melt pool area is extended and a control scheme is suggested. In the laser powder feed process, in situ thermal imaging is used to monitor melt pool length. Real time melt pool length measurements are used in feedback control to manipulate the resulting microstructure.

In laser and electron beam direct metal additive manufacturing, characteristics of the individual melt pool and the resulting final parts are a product of a variety of process parameters. Laser or electron beam spot size is an important input parameter that can affect the size and shape of a melt pool, and has a direct influence on the formation of lack-of-fusion and keyholing porosity. In this work, models are developed to gain a better understanding of the effects of spot size across different alloys and processes. Models are validated through experiments that also span multiple processes and alloys. Methods to expand the usable processing space are demonstrated in the ProX 200 laser powder bed fusion process. In depth knowledge of process parameters can reduce the occurrence of porosity and flaws throughout processing space and allow for the increased use of non-standard parameter sets.

Knowledge of the effects of spot size and other process parameters can enable an operator to expand the usable processing space while avoiding the formation of some types of flaws. Based on simulation and experimental results, regions where potential problems may occur are identified and process parameter based solutions are suggested. Methods to expand the usable processing space are demonstrated in the ProX 200 laser powder bed fusion process. In depth knowledge of process parameters can reduce the occurrence of porosity and flaws throughout processing space and allow for the increased use of non-standard parameter sets.

Table of Contents

Table of Figures

Nomenclature

A – Melt pool cross sectional area

A_0 – Melt pool cross sectional area produced by a point heat source in simulations

c_p – specific heat

D – Melt pool depth

D_0 – Melt pool depth produced by a point heat source in simulations

EB-PBF – Electron beam powder bed fusion process

EBWF – Electron beam wire feed process

FL – Melt pool full length

k – Thermal conductivity

L – Melt pool length from the point of maximum depth (or latent heat of fusion)

L_0 – Melt pool length from the point of maximum depth produced by a point heat source in simulations

L-PBF – Laser powder bed fusion process

LPF – Laser powder feed process

n – Operating parameter in Eagar-Tsai Model ($n=qv/(4\pi\alpha^2\rho c_p(T_{melting}-T_0))$)

q – Power input

R – Distance from heat source ($R=(w^2+y^2+z^2)^{1/2}$)

T – Temperature

T_0 – Initial or background temperature

t – Time

u – Dimensionless distribution parameter in Eager-Tsai Model ($u=(v\sigma)/(2\alpha)$)

v – Velocity

w – Distance in x-direction in a moving coordinate system ($w=x-vt$)

W – Melt pool width

W_0 – Melt pool width produced by a point heat source in simulations

x – Distance in x-direction

y – Distance in y-direction

z – Distance in z-direction

z_0 – Offset of beam focal point from z=0 at nominal settings

α – Thermal diffusivity

ζ – Dimensionless distance z

θ – Dimensionless temperature ($\theta=(T-T_0)/(T_{melting}-T_0)$)

ξ – Dimensionless distance in moving coordinate ($\xi=vw/(2\alpha)$)

ρ – Density

σ – Spot size

σ_0 – Spot size at the beam focal point

τ – Dimensionless time

ψ – Dimensionless distance y

Chapter 1: Introduction

1.1 Additive Manufacturing

Additive manufacturing (AM) is an automated manufacturing method that builds up parts by adding one layer at a time until completion. This method of manufacturing consists of processes ranging from desktop plastic 3D printers to industrial metal processes capable of producing final production parts. In most methods, the process begins with a computer aided design (CAD) model that is sliced into two dimensional layers before deposition paths and settings are generated. Deposition is accomplished by a few different methods which can affect the build rate, resolution, part quality, and more [1]. Work outlined in this thesis will focus on direct metal additive manufacturing processes (i.e. laser powder bed fusion, electron beam powder bed fusion, laser powder feed, and electron beam wire feed).

Laser powder bed fusion (L-PBF) and electron beam powder bed fusion (EB-PBF) are similar process that spread thin layers of metal powder over each layer before using a laser or electron beam to melt and fuse material. Differences between the processes go beyond the heat source used to melt the powder. Electron beam powder bed fusion generally has higher deposition rates and scan speeds when compared to laser powder bed fusion, but has poorer surface finish and resolution [1] [2]. Additionally, electron beam powder bed fusion uses a high preheat before melting that helps reduce residual stress that may build up in parts deposited with laser powder bed fusion. The process also differs in alloys available for processing. Laser powder bed fusion equipment manufacturers allow for the use of a wide range of alloys including titanium alloys, steels, aluminum and more while electron beam powder bed fusion is only limited to a few alloys [3] [4]. Both processes are capable of generating final parts that require little to no post processing.

Laser powder feed and electron beam wire feed processes generate near net shape parts and can have higher deposition rates when compared to the powder bed processes. Electron beam wire feed processes create a melt pool on the substrate using an electron beam, and wire stock to feed material into the melt pool. This process can create melt pools that can be over one inch in width and is primarily used to create larger near net shape parts [5]. The laser powder feed processes use a laser to create a melt pool on the substrate where inert gas blows powdered metal to add material [6]. This process creates near net shape parts on a smaller scale than the electron beam wire feed process and can also be used to repair existing parts [7] [8]. Both processes offer a wide range of alloys that can be used to produce parts [9] [10]. Power and velocity of the heat source are the most influential factors on individual melt pool size, and all four processes outlined above inhabit different regions when plotted in power-velocity space as shown in Figure 1-1.

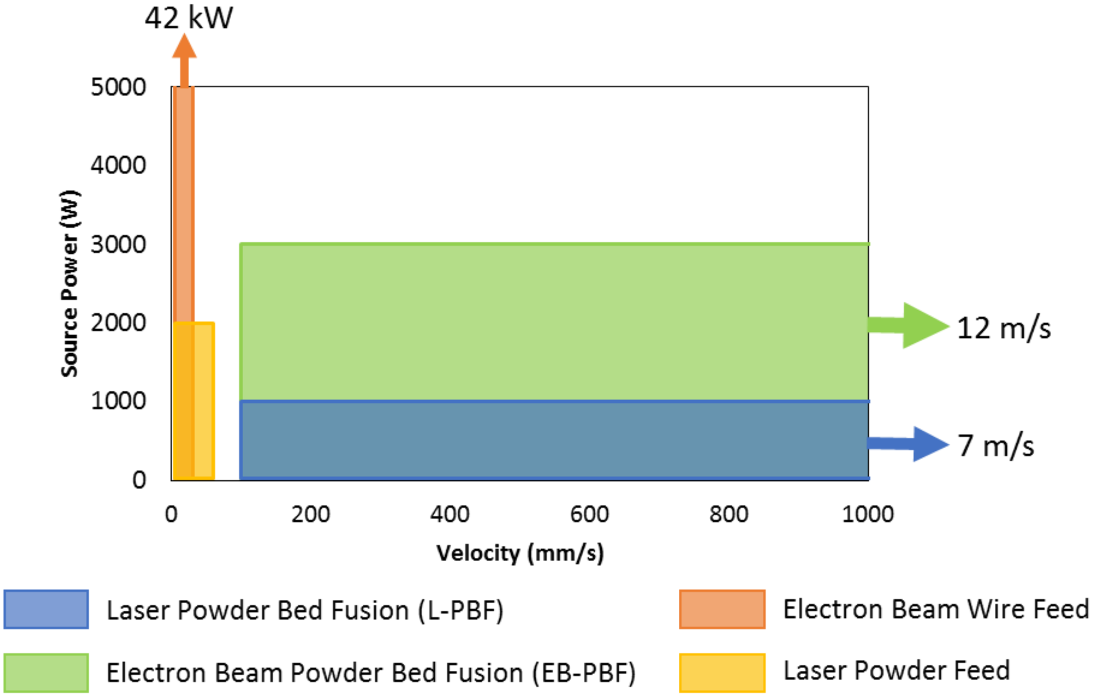

Figure 1-1: Major direct metal additive manufacturing processes in power-velocity space

Direct metal additive manufacturing has seen its earliest adoption in the aerospace and biomedical industries [2]. In the biomedical industry, this technology is especially useful because of the ability to create custom implants or braces for individual people and individual injuries. The aerospace industry's interest in additive manufacturing stems from the ability of the technology to manufacture more complex geometries that can help reduce weight, improve efficiency, and improve lead times [11]. Examples in industry have shown how additive manufacturing can combine multiple pieces into one part all while decreasing weight and increasing efficiency [12]. For these reasons, many other industries have shown interest in adopting the technology.

1.2 Motivation

Increased use of direct metal additive manufacturing in industry and the desire to use it for final production parts has highlighted a need to better understand how process parameters can affect the final product. The most influential process parameters include power, velocity, laser/electron beam spot size, preheat, hatch spacing, and more. The multitude of parameters directly affects process outcomes like melt pool size, aspect ratio, resulting microstructure, and porosity among others. The effects of a process parameter on certain process outcomes is generally known; however, if a specific process outcome is desired, significant trial and error is currently required. Due to a lack of specific knowledge about the effects of many process parameters, part qualification can require a large amount of time and money [12] [13] [14].

The process parameters that have the biggest effect on deposition are the power and velocity of the heat source. Significant work in that area has shown how the two variables affect melt pool size. However, power and velocity alone can lead to unacceptable deposits in some regions of processing space. In these regions, spot size adjustments are needed to ensure consistent results and the melt pool size must be balanced with hatch spacing and layer thickness, or material feed rate, to result in complete fusion between layers. Expanding the usable region of processing space can allow designers to use higher deposition rates, modified microstructure, improved surface finish, and more.

Knowledge of how the different process parameters affect the resulting deposition can also be used to modify microstructure throughout a part. Since AM builds parts one melt pool at a time, microstructure can be tailored to the designer’s needs in different regions of the design [15] [16]. This unique capability can only be realized if relations between process parameters, melt pools, and microstructure are well understood.

1.3 Literature Review

1.3.1 The Effects of Process Parameters

Research into the effects of process parameters has been key to the development of additive manufacturing since its inception. Process parameters affect the melt pool geometry, microstructure, flaw formation and more. Process mapping is the method of plotting process outcomes in terms of process parameters and was originally used in additive manufacturing to show how thermal gradients, melt pool size, and residual stress is affected by parameters in the laser powder feed process [17] [18] [19] [20] [21] [22]. Process mapping has since been used to relate melt pool size to process variables in various alloys and processes [23] [24] [25] [26] [27] . In addition to melt pool dimensions, microstructure has been process mapped for its relationship to process parameters [28] [29] .

The effects of process parameters has been analyzed outside of the realm of process mapping and has given insights to a number of other process outcomes. Porosity in AlSi10Mg parts was analyzed for different hatch spacings, scan speeds, and scan strategies in the Realizer GmbH laser powder bed fusion process. It was found that smaller hatch spacing and lower scanning speed reduced porosity, and that a scanning strategy with a pre-sinter step produced parts with the greatest density [30]. Montgomery et al. found that typical powder layer thicknesses had a minimal effect on melt pool dimensions [25]. Process parameters were related to flaws in both the laser powder bed fusion and electron beam powder bed fusion processes for Ti-6Al-4V. Additionally, regions of processing space were labelled to show regions of appropriate, excessive, and insufficient energy input to avoid flaws [31]. In laser welding, Tzeng related process parameters to surface quality of the bead and found velocity, power, pulse duration, and power density to be the most influential factors [32]. Safdar et al. compared surface roughness values in experiments varying wall thickness, power, velocity, and spot size in Ti-6Al-4V with the Arcam electron beam powder bed fusion process [33]. Hann related enthalpy values to melt pool size and shape for laser welding [34]. Fatigue and fracture characteristics have also been analyzed in different regions of processing space [35].

1.3.1.1Effects of Spot Size

Beam spot size is a process parameter that has been identified as important to the size and shape of melt pools; however, minimal research has been done to methodically track its effects. Differences in single bead tracks for different power distributions has been analyzed and found that higher power density at the center of a Gaussian beam helped avoid insufficient melting at low powers when compared to a tophat and inverse Gaussian distributions [36] [37]. Roehling et al. investigated the effects of elliptical beam profiles and found elliptical shapes left rougher, discontinuous tracks with equiaxed grains when compared to a circular, Gaussian beam [38]. Other work in additive manufacturing identified some of the effects of changing spot size. Mudge and Wald noted that spot size should be increased with power to increase deposition rate in the laser powder feed process, but that the change in process parameters would result in a coarser surface finish [39]. Miller et al. designed a laser powder bed fusion workstation with variable spot size to be able to increase deposition rate [40]. Bi et al. observed that a defocused beam decreases the melt pool surface temperature [41]. Increasing spot size was found to decrease the surface roughness of thin walls in thin wall structures in the electron beam powder bed fusion process [33]. The good processing window for IN 718 in the electron beam powder bed fusion process moves to a higher velocity region when the spot size is decreased. In the same process and material, the columnar grain structure was more consistent when a defocused beam was used [42]. In welding, research has been done to identify the effects of spot size on weld penetration depth, a smaller spot size yields a deeper weld [43] [44].

Spot size has also been shown to have an effect on the formation of potential flaws both in welding and additive manufacturing. In welding, keyholing porosity can be avoided by expanding the beam size [45] [46]. Norris et al. proposed that keyhole porosity can be avoided when the beam radius to keyhole depth ratio is greater than 0.15 [45]. In additive manufacturing, proposed normalized enthalpy thresholds to avoid keyhole took into consideration the beam power, velocity, and spot size [47]. Dinwiddie et al. was able to identify porosity or incomplete melting on the surface of newly melted layer in the electron beam powder bed fusion process and observed that a more diffuse beam had an increase in flaws in layers above an overhang [48]. Gong et al. measured increased porosity if spot size was either too large or too small, suggesting operators must find an optimum value to balance with other parameters [31].

1.3.2 Process Monitoring and Control

Process monitoring gives insights into the details of additive manufacturing processes and can help identify flaws when they occur. When monitoring is used in real time, control algorithms can be put in place to repair flaws or ensure desired outcomes are produced [49]. The laser powder feed process is a common process for real time monitoring due to its relatively low travel speeds. Early work in monitoring of the LENS process looked at temperatures within the melt pool to identify cooling rates that gave insight into the resulting microstructure [50]. Other work in the LENS laser powder feed process monitored the temperatures in the melt pool and modified power to maintain constant temperature to avoid additional oxidation [41]. Hu and Kovacevic used process monitoring in the laser powder feed process to control melt pool size to reduce variation and improve dimensional accuracy [51]. Monitoring has also been used to modify power to control layer height in addition to modifying melt pool temperature to follow defined paths [52] [53].

Although monitoring is generally easier in the laser powder feed process, work is continuing on monitoring different aspects of the other additive manufacturing processes. Melt pool monitoring in the laser powder bed fusion process has been used in feedback control to maintain consistent melt pool surface area [54] [55]. In the electron beam powder bed process, monitoring is taking place to detect porosity on the surface of parts to give insights on the effects of process parameters [48]. Mireles et al. used thermal imaging in the Arcam electron beam powder bed fusion process to identify pores in each layer before re-melting areas where a pore was identified [56]. Thermal imaging has also been used on a layer by layer basis to control process parameters to maintain consistent surface temperature as build height increases [57]. Layer by layer imaging has also been used to identify flaws in powder spreading that can result in flaws upon melting [55]

[58] [59]. Process monitoring and feedback control has been used for many aspects of additive manufacturing and gives users greater confidence in the resulting part quality [60].

1.3.3 Deposition Flaws

Deposition flaws occur for a number of different reasons, but all have the ability to negatively impact the build quality and performance of additively manufactured parts. Two of the most common sources of flaws are porosity from lack of fusion and keyholing. Keyholing, often a desirable quality in welding due to an increased penetration depth, occurs when the beam energy density is high enough to vaporize material in the melt pool. Keyholing is more variable and can leave behind porosity, causing problems in additively manufactured parts. Significant research has been done in the welding community on the development of keyhole pores [43] [45] [61] [62] [63] [64]. Additionally, observations have been made noting increased variability when a keyholing melt pool is produced [45] [64] [65]. Detailed models of the keyholing process have been developed to gain a better understanding of the phenomenon [66] [67]. In additive manufacturing, King et al. proposed a method to avoid keyholing by proposing normalized enthalpy thresholds could signal when keyholing starts [47]. In addition to creating pores, vaporized material in keyhole melt pools can cause preferential loss of some alloying elements [43] [65] [68]. Porosity was analyzed across processing in both the EOS L-PBF and Arcam EB-PBF processes and showed how process parameters and resulting melt pools can influence the occurrence of different types of porosity [69] [70].

Lack of fusion flaws occur when the heat source does not sufficiently melt into the previous layer, or when the hatch spacing is too large. Previous work has identified methods to predict the occurrence of lack of fusion flaws based on melt pool dimensions [71]. Other work has observed lack of fusion flaws as it related to various process parameters [30] [31]. Seifi et al. analyzed fracture toughness and fatigue crack growth in samples from the electron beam powder bed fusion process and found evidence of lack of fusion on the fracture surface [35].

Another major source of flaws in additively manufactured parts is related to fluid flow within the melt pools. Flow in weld pools not only influences variability in melt pool dimensions, but can also contribute to flaws that may occur [72]. Nemchinsky suggested thermocapillary instability arising from gradients in temperature and subsequently surface tension in melt pools could result in increased variability and flaws [73]. The bead-up phenomenon that is occasionally seen in additive manufacturing has been described as a result of Rayleigh instabilities in the melt pool where a liquid cylinder breaks up a continuous bead. The magnitude of these effects has been related to width to length ratio of the melt pool [74]. A width to length threshold has been suggested to avoid bead up in additive manufacturing [75]. In welding, Kou et al. found that the direction of fluid flow at the back of the melt pool can affect the development of porosity [76].

1.3.4 Microstructure

A strong understanding of the development of microstructure in additive manufacturing is critical for process parameter selection and the tailoring of mechanical properties throughout parts. . Kobryn identified the effects of power and velocity on grain size in Ti-6Al-4V [77] [28]. Other work process mapped cooling rates and thermal gradients. Information from thermal gradients and cooling rates was used to identify grain morphology that would develop in the deposition [78] [79] [80]. In more recent years, microstructure itself was related to melt pool area [81] [82] [83]. Accompanied with process maps for melt pool dimensions, this related microstructure to process parameters and allowed microstructure to be controlled directly from real time monitoring.

Microstructure development has also been investigated in laser keyhole welding and insights to how microstructure forms in keyholing with additive manufacturing can be drawn [84].

Microstructure has been simulated and measured across many different additive manufacturing processes to add to the collective knowledge base. In the laser powder feed process, cooling rates were simulated and microstructure was analyzed [11] [85]. Kelly simulated the laser powder feed process and the development of Ti-6Al-4V microstructure to show how bands of colony alpha microstructure form do to heat cycles from following layers [86]. Lin et al. noted differences in grain structures between the laser powder bed fusion process and the electron beam powder bed fusion process [87]. Antonysamy measured Ti-6Al-4V prior beta grains in the laser powder bed and electron beam powder bed process and also produced tensile bars in the processes to compare to wrought properties [88]. Narra et al. demonstrated how to produce different regions in different areas of an additively manufactured part [89]. Murr et al. did tensile testing for the Arcam electron beam powder bed system and found properties similar to wrought material [90].

1.3.5 Modeling

Modelling the additive manufacturing process shares many similarities with models produced for welding. One of the most fundamental models for welding, is that of a simple moving point heat source [91]. The analytical model derived by Rosenthal can still give insights into the additive manufacturing process today. Christensen made improvements to the Rosenthal model by developing a dimensionless form [92]. Using superposition, Eagar and Tsai used these analytical models to create a model of a moving heat source with a Gaussian distribution [93]. A major limitation of these models, however, is the use of constant thermal properties.

Early work in additive manufacturing improved on the understanding of processes and how process parameters may influence the melt pool and deposition [85] [94]. It was found that for a surface temperature of 2000K, less than 6% of the power is dissipated my mechanisms other than conduction. At 3080K, evaporation becomes a more important factor, but conduction still accounts for 80% of power dissipation [95]. With increasing computing power came more detailed models. Wang simulated a thin wall part to find a power program that would maintain a more consistent melt pool size as more layers were added [96]. Other multi-layer models were used to predict residual stress in the resulting part [97] [98]. Very complex models that take into account a large number of variables that include heat transfer, fluid flow, powder, and more have been developed to gain a better understanding of how the process works and how flaws may form [99] [100].

Microstructure modelling has also been insightful for the progress of additive manufacturing. In the laser powder feed process, Kelly modeled and identified how additional layers affected microstructure existing depositions [86]. Nie modeled microstructure evolution during solidification of IN 718. The model was used to produce results for various thermal gradient-cooling rate combinations and compared to results from actual depositions with good agreement [101]. Zinoviev modeled 316 stainless steel microstructure development in the laser powder bed process [102]. The model yielded grain behaviors that are commonly seen in additive manufacturing.

1.4 Organization

This thesis is organized into seven different chapters. The first chapter introduces additive manufacturing and the four primary direct metal additive manufacturing processes that are of primary interest. Motivation is given for the work before a literature review summarizes work pertinent to this dissertation. The literature review covers effects of process parameters including spot size, monitoring and control, deposition flaws, microstructure, and modeling.

The second chapter covers projects involving the process mapping and microstructure control of Ti-6Al-4V in the laser powder feed and electron beam wire feed processes. Finite element models are used to generate process maps for melt pool cross sectional area. Experiments are related to the process maps generated with finite element models via an effective absorptivity. In each process, methods to control microstructure via melt pool monitoring are proposed.

Chapter three covers the effects of beam spot size on melt pool geometry in detail. Models based on the finite element method and the Rosenthal solution are used to systematically ascertain the effects of spot size. Normalization is used to plot melt pool dimensions to collapse a variety of results to simpler curves for each dimension. Experiments are shown to back up models results across multiple alloys, processes, and process parameters.

Chapter four analyzes the effects of spot size on the occurrence of porosity in additively manufactured parts. Keyholing is identified in experimental melt pools and a method for avoiding the phenomena is presented. Guidance is also given on how to avoid lack of fusion flaws by balancing melt pool dimensions with hatch spacing and layer thickness. Experimental results of multi-layer deposits are presented.

Chapter five extends work in previous chapters to identify if spot size has an effect on the resulting microstructure. Normalized cooling rates from simulations are presented and compared to both single layer and multi-layer experiments.

The sixth chapter combines work done in this thesis to present a method to expand the available processing space. Methods for doing so are presented and used to improve usability of a laser powder bed fusion process for multiple alloys. Experiments are completed for both single layer and multi-layer deposits.

Chapter seven summarizes the conclusions and contributions of this work. Recommendations for future work related to the subjects in this thesis are provided.

Chapter 2: Process Mapping and Microstructure Control of Ti-6Al-4V in Laser Powder Feed and Electron Beam Wire Feed Processes

2.1 Overview

This chapter explores process mapping and microstructure control in the electron beam wire feed and laser powder feed processes. Knowledge about changes in melt pool geometry enables operators to correctly balance spot size, hatch spacing, and other parameters to build a part successfully. Operating outside of standard parameters can result in a preferred deposition rate, resolution, microstructure, or other outcomes. Previous work has been done outlining how optimal parameter sets can be found in processing space [103].

Methods to control microstructure for Ti-6Al-4V in these processes is also investigated. The focus of analysis in this work is centered on the size of prior beta grains. The alpha phase dominates most material properties (e.g. yield strength), but the alpha structure can be modified through post-build heat treatment. Beta grains are an important factor for mechanical properties such as toughness [104] [105]. Additionally, the beta phase has an influence on the development of the alpha phase and therefore is important to measure in additive manufacturing [106] [107]. Relations are built in this chapter to relate melt pool dimensions to prior beta grain size for use with thermal imaging and feedback control systems.

2.2 Methods

2.2.1 Process Mapping Approach

Process mapping is a method that allows a user to easily relate input parameters to desired process outcomes. There can be more than 100 process parameters for a particular additive manufacturing process, but a limited subset of those have a significant effect on the process outcomes. The process mapping approach isolates primary process variables and identifies how key process outcomes are affected. Plots are created that feature lines of constant melt pool dimensions, microstructure, susceptibility to flaw formation, or other key quantities. Figure 2-1 is an example of a process map showing lines of constant melt pool cross sectional area from finite element simulation data.

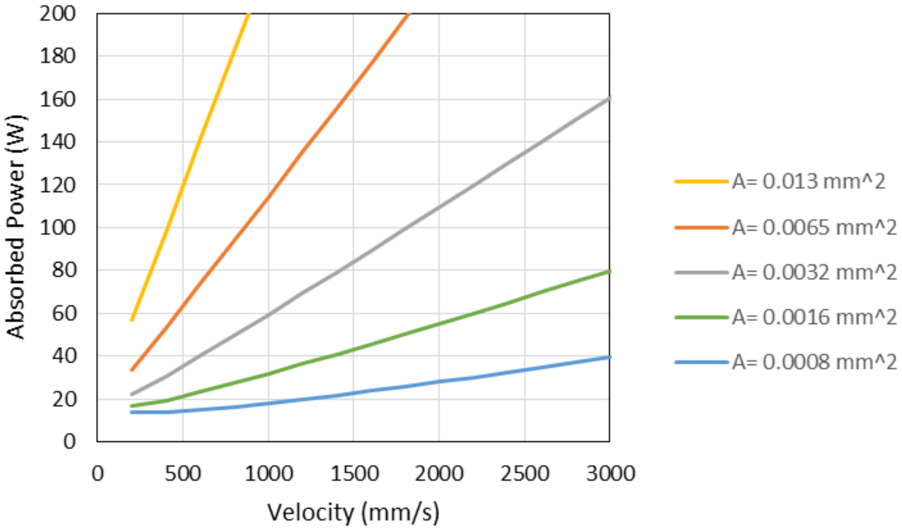

Figure 2-1: Power-velocity process map for melt pool cross-sectional area for 316L stainless steel in the L-PBF process

To verify process maps, simple experiments that cover the range of processing space are completed and analyzed. In this case, melt pool cross-sectional areas can be measured and related to simulation data via an effective absorptivity. In some cases, different lines of constant melt pool area may have different effective absorptivities if keyholing melt pools are present. Melt pools in the keyholing regime can have an increased absorptivity due to internal reflections in the keyhole cavity [108].

2.2.2 Finite Element Model

Numerical models were developed in the ABAQUS software package to simulate a single deposition pass of the additive manufacturing processes used in this chapter. The models are similar in structure to the model of a moving heat source developed by Rosenthal [91]. The models used in this work are modified versions of those used by Fox [23]. Improvements on the Rosenthal model include temperature dependent properties, variable spot size, latent heat, and more.

Temperature dependent properties for Ti-6Al-4V include thermal conductivity, specific heat, and density [109] [110]. Convection, radiation, fluid flow, powder effects and evaporation are neglected in these models as their influence has been shown to be minimal [95]. The sides of the model are given adiabatic boundary conditions and the base of the model is held at the prescribed preheat temperature. A symmetric boundary condition is used down the centerline of the melt pool.

The model progresses by stepping a distributed flux heat source in the positive X –direction in defined time steps to match the velocity prescribed by the user. The heat source travels through a fine mesh region to establish a well-defined steady state melt pool where cooling rate and melt pool dimensions can be measured. Biased elements are used to extend the substrate out far enough in all directions to prevent edge effects. For the electron beam wire feed process, added material is included to model the wire being fed into the melt pool. This is accomplished by initializing all elements before deactivating the elements representing added material. Added material elements are activated ahead of the applied flux in each time step until the end of the simulation. An example of the meshed substrate used to model the laser powder feed process is shown in Figure 2-2. A finite element melt pool is displayed in Figure 2-3 with some key dimensions labeled.

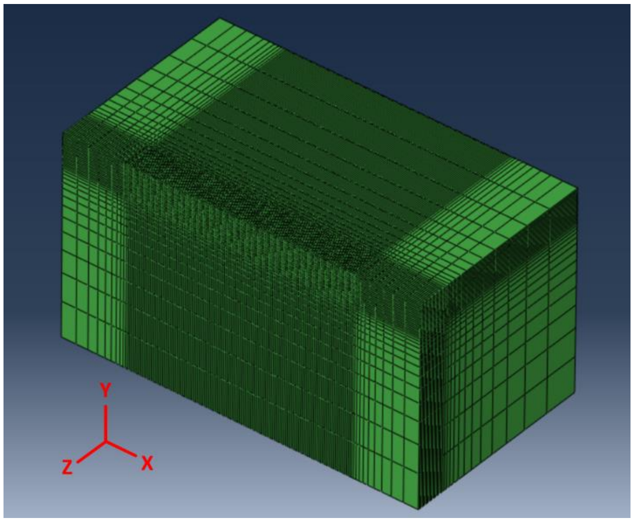

Figure 2-2: 3D model used for finite element simulation in the ABAQUS software package

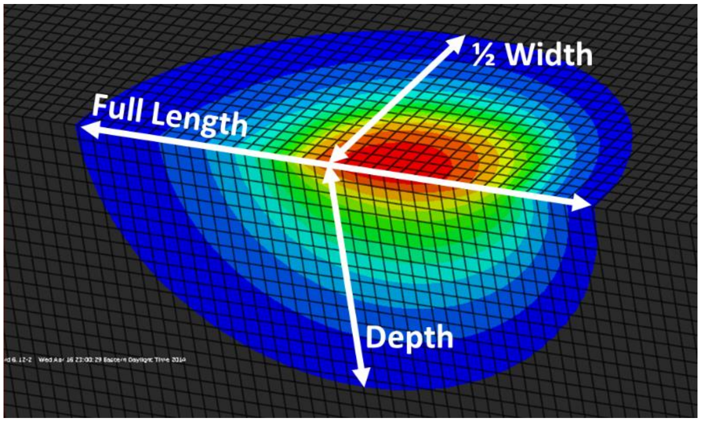

Figure 2-3: Key melt pool dimensions measured from finite element simulations

The ABAQUS software package models the moving heat source problem by solving the heat equation (Eq. 2-1). The heat equation balances energy stored in the material with energy leaving and energy being added.

Eq. 2-1

$$\frac{\partial}{\partial x}\left(k\frac{\partial T}{\partial x}\right)+\frac{\partial}{\partial y}\left(k\frac{\partial T}{\partial y}\right)+\frac{\partial}{\partial z}\left(k\frac{\partial T}{\partial z}\right)=\rho c_p\frac{\partial T}{\partial t}$$

When latent heat is considered, the equation becomes:

Eq. 2-2

$$\frac{\partial}{\partial x}\left(k\frac{\partial T}{\partial x}\right)+\frac{\partial}{\partial y}\left(k\frac{\partial T}{\partial y}\right)+\frac{\partial}{\partial z}\left(k\frac{\partial T}{\partial z}\right)=\rho c_p\frac{\partial T}{\partial t}+\ \rho L$$

ABAQUS uses a backward difference algorithm in the time domain for its simplicity and well-understood behavior. It is conditionally stable, but avoids oscillations that can be present in unconditionally stable methods, like the central difference method. ABAQUS uses a modified Newton-Raphson method to solve the resulting equation [111].

Key melt pool dimensions that can be gathered from simulation results include cross sectional area, width, depth, full length, length from maximum depth, and more. Completing a series of simulations throughout processing space can give insight to melt pool sizes and trends that can expected for different melt pool dimensions. Work presented in this chapter generally focuses on melt pool cross sectional area.

2.2.3 Experiment Design and Measurement

Single bead process mapping experiments are deposited at power-velocity sets that form a grid throughout the available processing space. This design is able to give information about the different regions of processing space, and the flaws that may occur. In the LENS laser powder feed process, sixteen power-velocity combinations spanned 150-450 watts and 15-45 in/min. Three powder feed rate schemes were also used for single bead experiments in the LENS process. The nominal case for the process was given as 450 W, 25 in/min, and 3 grams per minute (gpm) feed rate. The first was the most simplistic, a no-added material case that compared directly to the simulations for the laser powder feed process. The second used the nominal powder feed rate of 3gpm throughout the entire processing space, and the third scaled powder feed rate from the nominal case with velocity. An image of a depositions from the LENS process with single bead experiments is shown in Figure 2-4. Single beads were deposited in straight lines 2.5 inches long to ensure steady state melt pool conditions have formed. Alternate geometries were also deposited at nominal parameters (450 W, 25 in/min, 3 gpm) for analysis of how melt pools and resulting microstructure differ for different geometries.

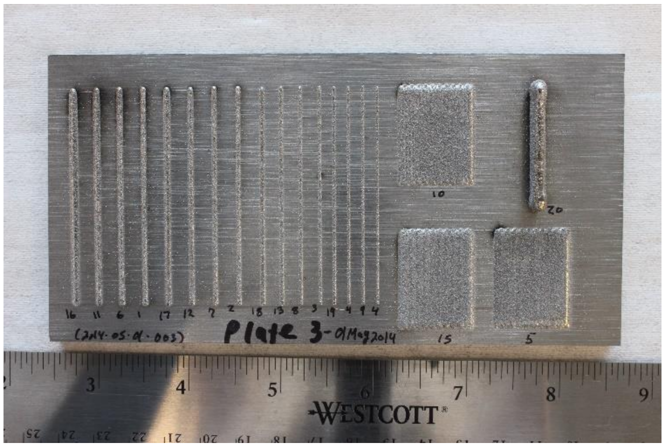

Figure 2-4: LENS processed plate including single bead deposits and scaled powder feed rate

Thermal imaging was used to control melt pool length for microstructure control experiments in the laser powder stream process. The camera, provided by Stratonics, was a two wavelength imaging pyrometer with a temperature range of 1000 to 2000 Celsius, capturing four frames per second. Figure 2-5 shows the steps used to maintain a consistent melt pool length. The process of controlling melt pool length begins with process deposition at a prescribed set point. Thermal imaging gathers information about temperatures in and around the melt pool and a melt pool length measurement can be taken from this processed data. The length measurement is compared to a desired value and power is controlled to achieve the specified value. In these experiments, a 10.5 inch single bead deposit was created. At each 3.5 inch interval, a different desired length was input to the controller. A proportional controller was used to change the melt pool length. At the time of these experiments, the integral and derivative portions of the controller had not yet been developed by Stratonics. At low specified lengths, some instability was seen in the control algorithm as is observed in the "Power control" plot in Figure 2-5.

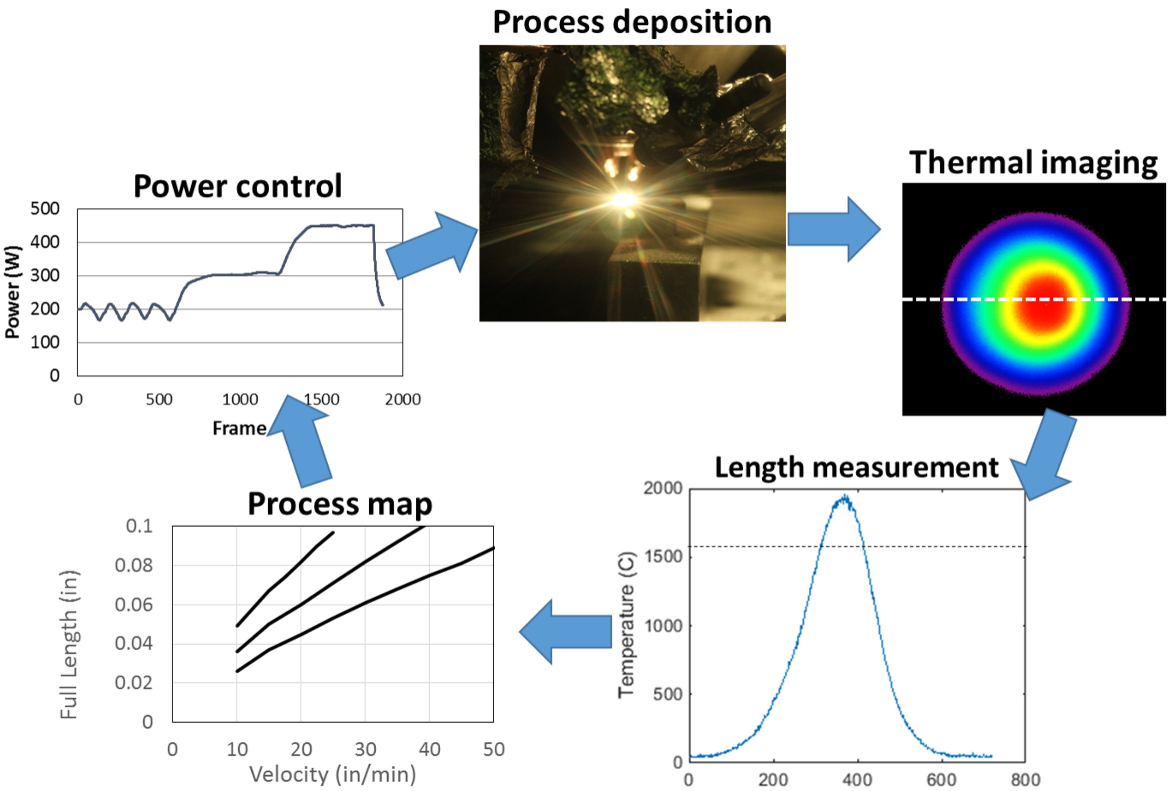

Figure 2-5: Thermal imaging process control

Process mapping experiments in the electron beam wire feed process were designed to extend the process map created by Fox to higher powers [23]. A nominal case for the Sciaky electron beam wire feed process was given as 10 kW, 30 in/min, and 15 lbs/hr. Experiments for process mapping ranged from 10-25 kW and 30-60 in/min. Feed rate was scaled with the anticipated melt rate, which can be calculated with Eq. 2-3. Additionally, multi-layer experiments were completed at select points in processing space. The experiment plan with both single bead and multi-layer deposits in the electron beam wire feed process is shown in Figure 2-6.

Eq. 2-3

$$Melt\ Rate = A \times v$$

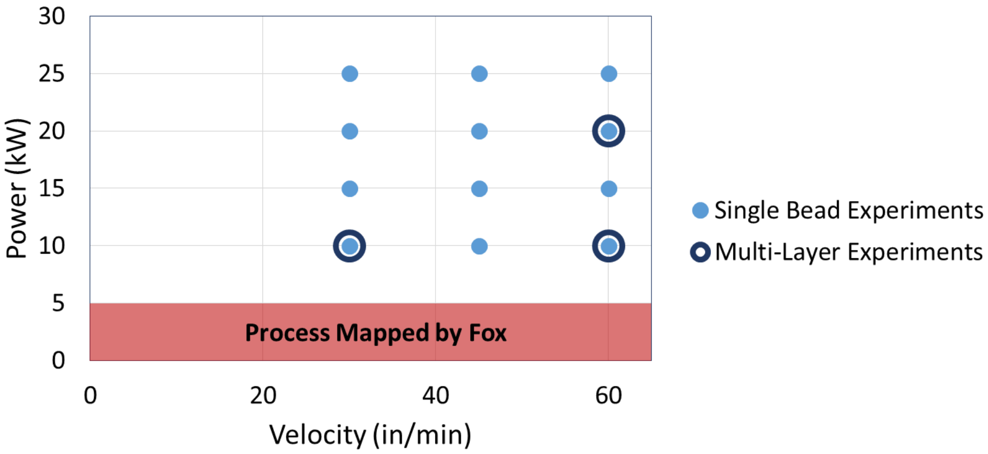

Figure 2-6: Sciaky electron beam wire feed process experiment plan

Single layer beads were deposited across a 24” x 12” x 1” Ti-6Al-4V plate. Single beads were deposited along a 22” stretch where process parameters were changed 11” into the deposit. This allowed for an increased number of melt pools to be deposited and with enough space to reach steady state melt pool dimensions. Single and multi-layer pads were built in either 21” or 10” blocks depending on the expected melt pool length. Multi-layer pads were created fifteen layers high, which was tall enough to reach steady state conditions in the z direction. A limitation of the machine required all deposits to be completed parallel to each other and in the same direction. Figure 2-7 shows three plates with single bead deposits, single layer pads, and multi-layer pads.

The long pad on the left plate was stopped due to incorrect process parameters and built correctly on a later plate.

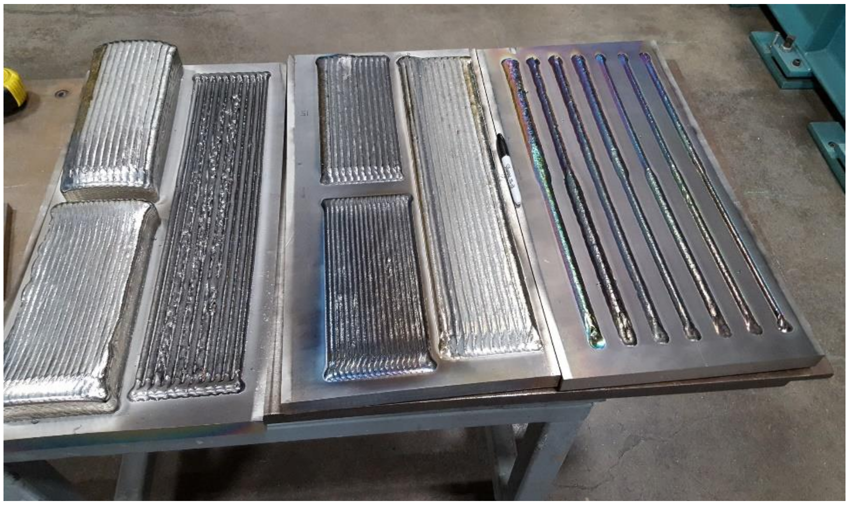

Figure 2-7: Experiments plates deposited in the Sciaky process

Once experiments are completed, samples are prepared for analysis. Samples are cross-sectioned, polished, and etched using Kroll’s etchant. Procedures for polishing and etching can be found in Appendix 1. Samples are then imaged using an Alicona Infinite Focus optical microscope. Melt pool cross-sectional dimensions and average prior beta grain width can be measured. Prior beta grain size is measured using the intercept method [112]. Prior beta grains in these processes are columnar in nature so prior beta grain width is the dimension of focus in this study. A horizontal line is drawn perpendicular to the growth direction of columnar grains, and grains are counted then the total is divided by the length of the line. The process is repeated throughout the sample and all lines are averaged.

Multi-layer pads were built to a height of 50 mm for the 10 kW, 30 in/min case, 40 mm for the 10 kW, 60 in/min case, and 15 mm for the 20 kW, 60 in/min case. Prior beta grain width measurements in the 10 kW cases are measured at three height locations, 5 mm apart in the center third of the deposit to determine if height is playing a role in prior beta grain width while avoiding any effects that may be caused by the edges of the deposit. The 20 kW, 60 in/min case was built at a reduced height due to limited availability of added material and only measured at a single height.

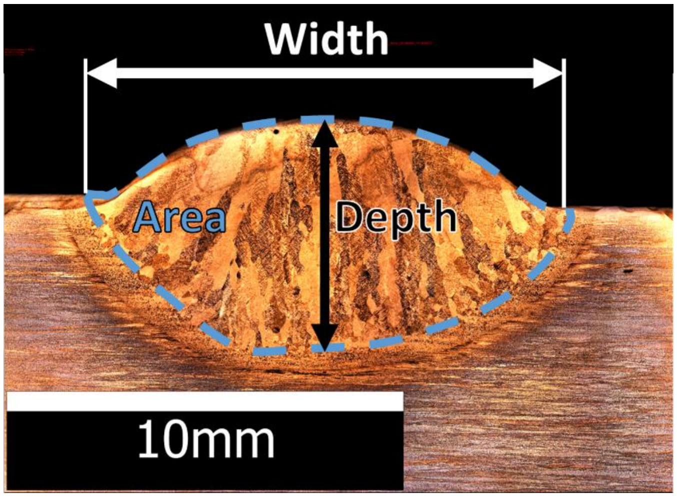

Figure 2-8: Key melt pool dimensions measured for a melt pool in from the Sciaky process

Figure 2-8 shows a melt pool cross section from the Sciaky process with key melt pool dimensions labeled. Cross-sectional width, depth and area are essential to the selection of process parameters like hatch spacing and material feed rate or layer thickness. Determination of melt pool boundaries can be difficult in some processes and alloys. In Ti-6Al-4V, this is because the beta transus temperature is much lower than the melting temperature causing significant microstructural transformations in the heat affected zone. To capture this uncertainty, the edge of prior beta grain growth can be used as an outer limit for the possible melt pool boundary. An inner limit for possible melt pool boundary can be formed by identifying the start of columnar growth in prior beta grains. A “Best Guess” measurement of the melt pool boundary is also taken. This boundary begins at where the straight edge of the substrate is interrupted by the melt pool. The boundary continues through grains of similar size and shape to the other edge of the melt pool. Placement of these three boundaries are demonstrated in Figure 2-9.

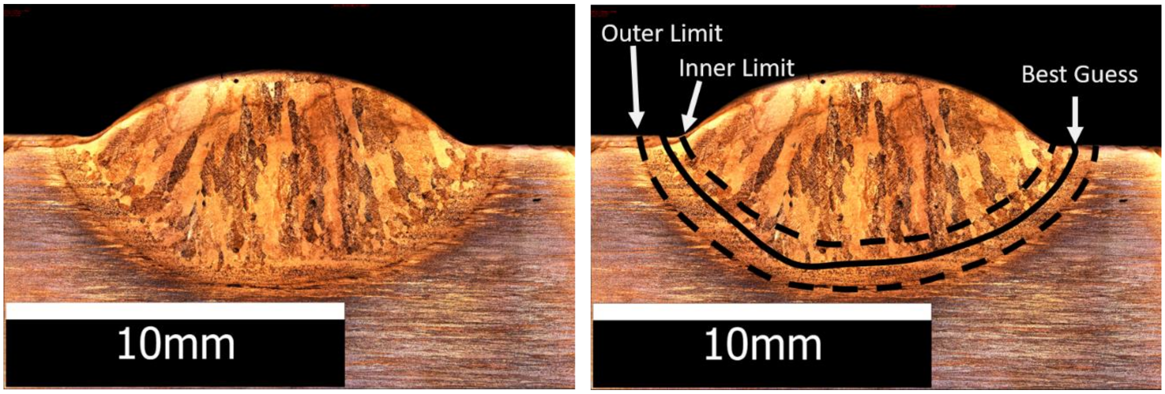

Figure 2-9: Measurement of uncertainty in melt pool area

Since serial sectioning can be prohibitively time consuming especially when a high number of samples are required, variability in this study has only been found for melt pool width. Variability for melt pool width can be found by imaging the single bead melt track from above and tracing the edges of the melt pool as seen from above. Figure 2-10 shows a melt pool viewed from above before and after the extents of melt pool width are traced in red. The traced image is run through a MATLAB script that measures the distance between the two red lines at every pixel moving from left to right. From these measurements, average melt pool width and standard deviation can be calculated.

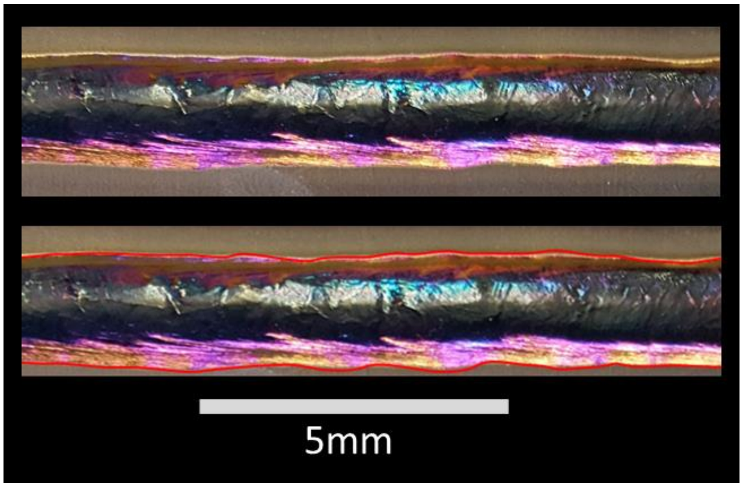

Figure 2-10: Tracing of melt pool width for calculation of standard deviation

2.3 Results

This section presents Ti-6Al-4V process maps for cross-sectional melt pool dimensions in the Sciaky electron beam wire feed and LENS laser powder feed processes along with methods to control prior beta grain width. In the electron beam wire feed process, cross-sectional width, depth and area are process mapped with good agreement with finite element simulation results. Variations are observed between lines of constant melt pool depth and width. Trends in prior beta grain width follow those found in work by Gockel [81] for single bead deposits, and are compared with results from multi-layer pads. Process maps in the laser powder feed process again show good agreement between simulation and experimental results. Comparisons are made between different feed rate schemes, and effects of feed rate on geometry are explored. A method to control prior beta grain width with the use of thermal imaging is presented.

2.3.1 Process Mapping the Sciaky Electron Beam Wire Feed Process

Direct metal additive manufacturing processes tend to have recommended parameter sets that the machine manufacturers suggest for producing successful parts; however, these do not take advantage of the full capacity of the technology. Process mapping of melt pool area gives insights into the parameters that can be used to modify resolution, deposition rate, or other process outcomes. Cross-sectional area process maps are displayed with lines of constant melt pool area that show where different melt pool sizes can be found in power-velocity processing space.

Figure 2-11 displays the power-velocity process map generated for the Sciaky electron beam wire feed process. Data from finite element simulations is presented as solid lines. Experimental "Best guess" measurements are represented by circular data points and measurement uncertainty is displayed as dotted lines around each cross-sectional area value. To find locations of the desired melt pool area from experiments, measurements at deposited power-velocity combinations were piecewise linearly interpolated. An effective absorptivity of 0.89 minimized the r^2 value to 0.9493 when matching experimental results to finite element results for all cross-sectional areas. This effective absorptivity matches well with values used in the past for this process [23]. Agreement between finite element results and experimental measurements can be improved if adjustments are made to maintain a consistent aspect ratio between melt pool depth and width. Details on the adjustments are discussed in Chapter 6:.

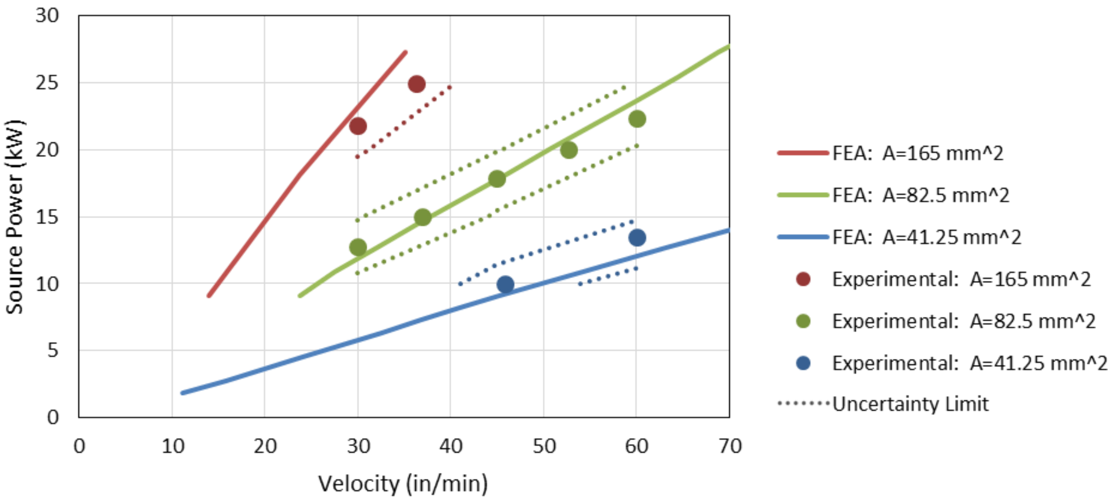

Figure 2-11: Power-velocity process map of melt pool cross-sectional area in the Sciaky process

Cross-sectional area is a useful melt pool dimension that provides valuable information about the melt pool, but melt pool width and depth can be more insightful when selecting parameters for a build. A process map of depth is shown in Figure 2-12 with uncertainty measured using the methods described in 2.2.3. Plotted depth values match cross-sectional area values used in Figure 2-11 if a semi-circular melt pool is assumed. Process mapped experimental points show a worse agreement with finite element results and an overall tighter grouping when compared to melt pool areas. This suggests that smaller changes in power are required to achieve a certain change in melt pool depth when compared to melt pool area.

Melt pool width is process mapped in Figure 2-13 using cross-sectional measurements. Dotted lines represent measurement uncertainty (see Figure 2-9) and values plotted match depth and area values in Figure 2-11 and Figure 2-12 for and assumed semi-circular melt pool. As with melt pool depths, processed mapped melt pool widths do not match finite element results well. As opposed to depth, a greater change in power is needed to yield a certain change in melt pool width. An explanation for differences in process map behavior is presented in Chapter 6:.

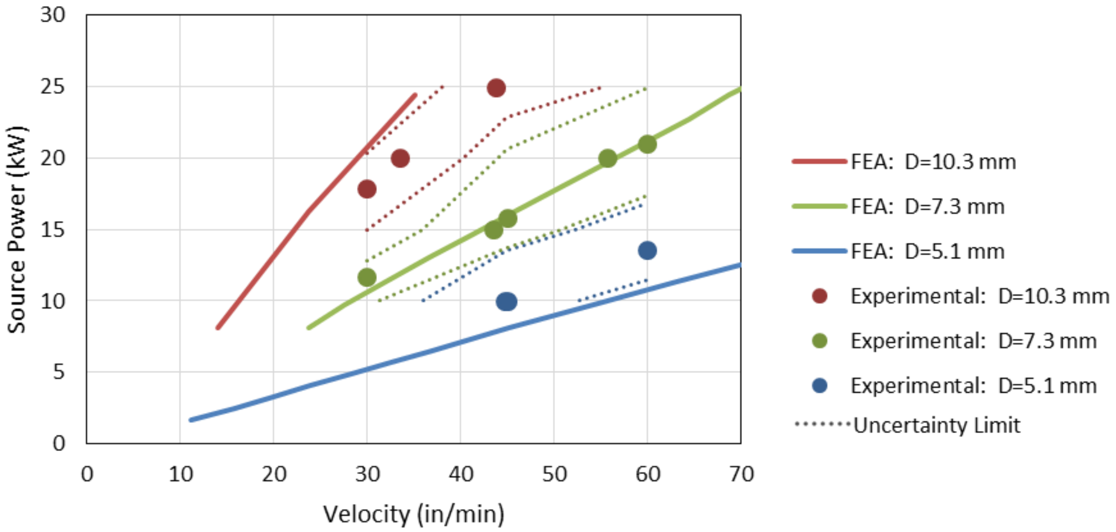

Figure 2-12: Power-velocity process map of melt pool depth in the Sciaky process

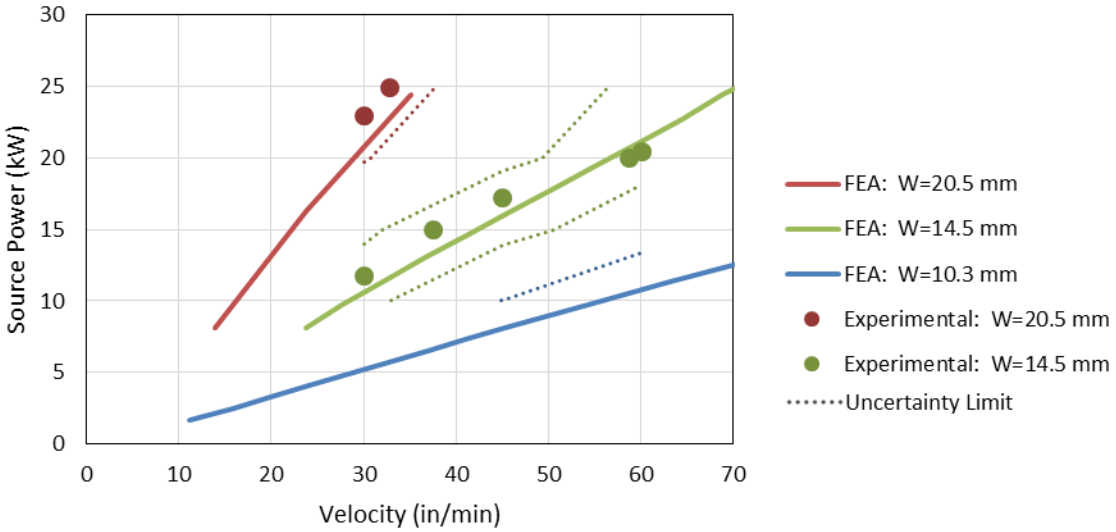

Figure 2-13: Power-velocity process map of melt pool width in the Sciaky process

Melt pool width can be measured via two methods for single bead deposits. Table 1 displays average melt pool width and standard deviation as measured from above along with the maximum and minimum limits measured from cross sections. In this process, the standard deviation of melt pool width was relatively insignificant when compared to the average width measured showing a stable melt pool. Ranges for uncertainty are also larger than the windows created using average values measured from above with two standard deviations.

Table 1: Melt pool width measurements in the Sciaky process

Melt Pool Width					
Power (kW)	Velocity (in/min)	"Best Guess" Width from Cross Section (mm)	Width Uncertainty from Cross Section (mm)	Average Width from Above (mm)	Standard Deviation from above (mm)
10	30	13.7	12.9 - 15.0	13.0	0.5
10	45	11.5	10.2 - 12.7	11.6	0.2
10	60	10.6	9.3 - 11.6	10.9	0.2
15	30	16.0	14.9 - 17.8	16.0	0.1
15	45	13.0	12.0 - 15.1	13.1	0.1
15	60	11.3	10.8 - 13.6	11.5	0.2
20	30	19.4	18.2 - 20.7	19.1	0.4
20	45	16.3	15.0 - 17.4	16.0	0.2
20	60	14.3	13.2 - 15.1	14.4	0.3
25	30	21.2	19.6 - 22.5	20.9	0.5
25	45	17.4	15.8 - 18.7	17.9	0.6
25	60	16.1	14.1 - 16.6	16.1	0.5

2.3.2 Process Mapping the LENS Laser Powder Stream Process

In the LENS laser powder feed process, a separate process map is generated for each powder feed scheme. The first scheme, which matches simulations most closely is the no added powder scheme. No powder added experiments and simulations give a more fundamental understanding of the melt pools being generated in the process because they involve fewer variables that affect the resulting geometry. No added material experiments (Figure 2-14) match up very well with finite element results using and effective absorptivity of 0.31 minimizing r^2 to 0.9539.

Scaled feed experiments adjusted material feed rate with velocity based on the nominal case at 25 in/min and 3 gpm. This provided the melt pool with a consistent amount of fed material per unit distance. Results for scaled feed rate are shown in Figure 2-15 with good agreement between finite element simulations at an effective absorptivity of 0.36 and an r^2 value of 0.9523. Constant 3 gpm feed rate experiments used 3 gpm powder feed throughout processing space and best matched finite element simulations with an effective absorptivity of 0.35 and an r^2 value of 0.8307. Regions of constant melt pool area for the 3 gpm case drops at the low velocity case (15 in/min), signaling that a lower power is required to produce the melt pool area at low velocities. Again, uncertainty is measured as described in section 2.2.3 and interpolated to make the dotted lines windowing the “best guess” measurements.

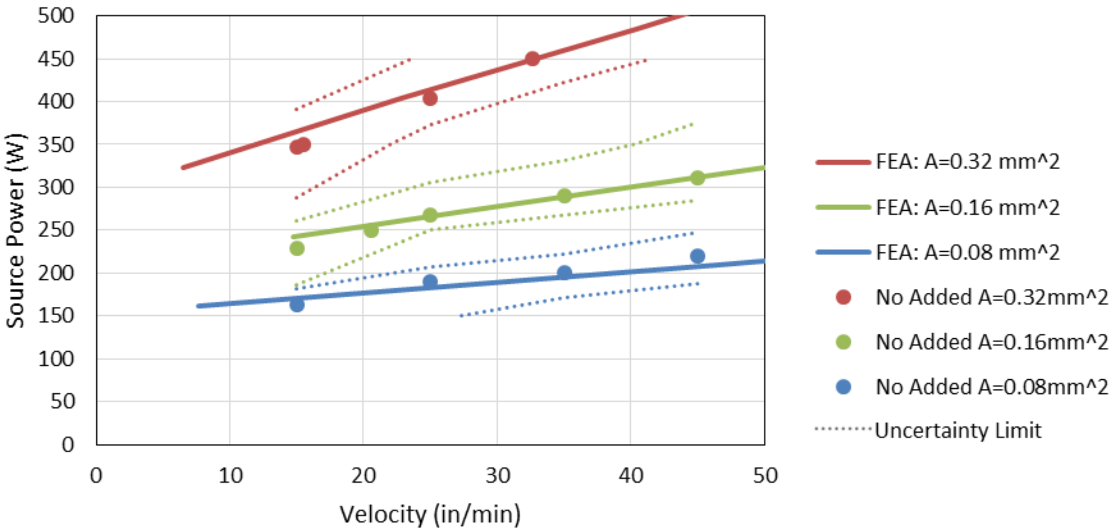

Figure 2-14: Power-velocity process map of melt pool cross-sectional area for the LENS process with no powder feed.

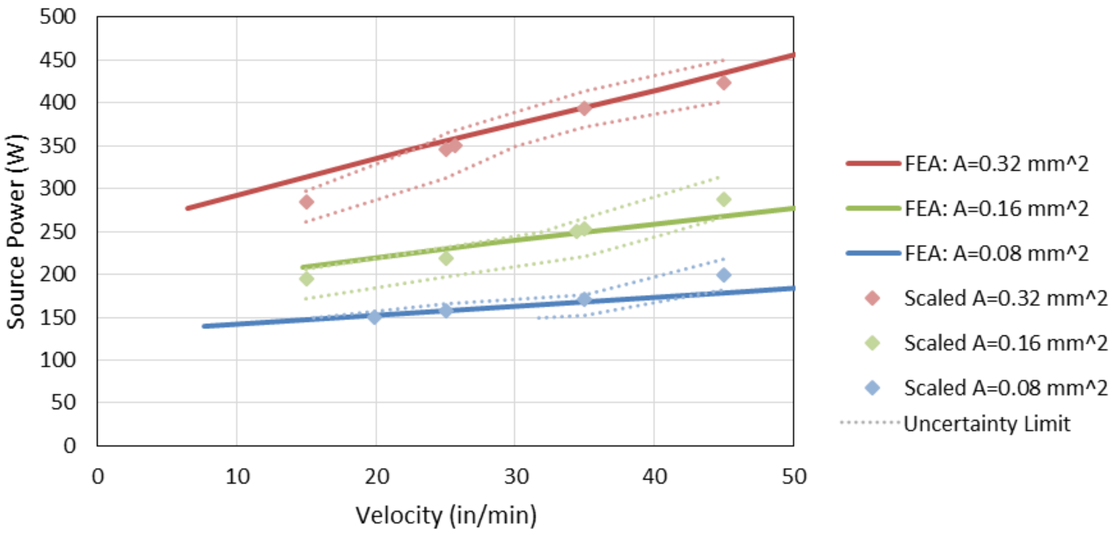

Figure 2-15: Power-velocity process map of melt pool cross-sectional area for the LENS process with scaled powder feed

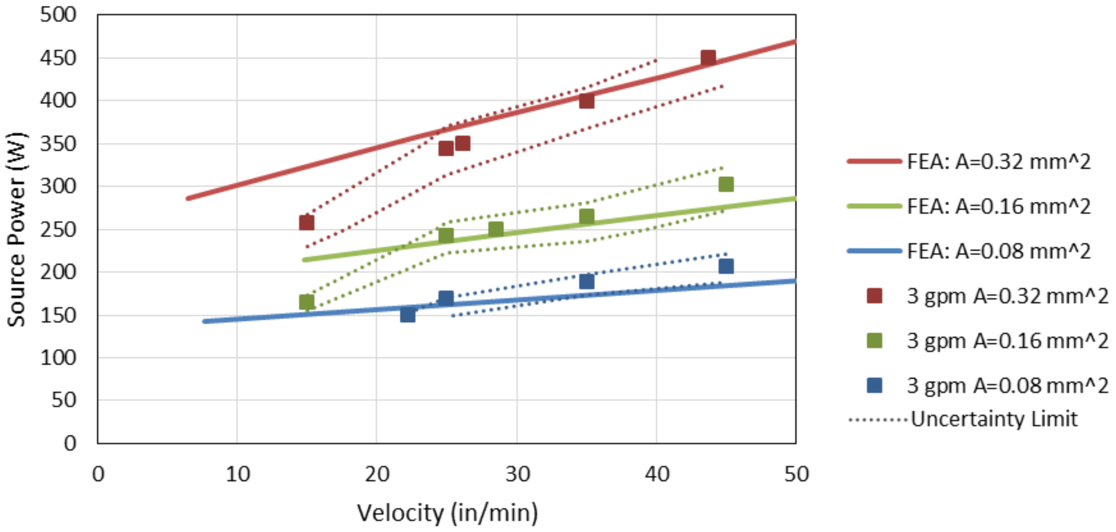

Figure 2-16: Power-velocity process map of melt pool cross-sectional area for the LENS process with constant 3 gpm feed

Comparison between the three different feed rate scenarios gives insights to the effects of powder feed rate. In all prescribed areas, the no-added material cases require more power to create an equivalent area. This suggests that increased material feed increases the resulting melt pool area. The notion is supported when comparing the scaled feed rate and constant 3 gpm schemes. At the low velocity case, lower powers are needed by the 3 gpm case to create an equivalent melt pool area when compared to the scaled feed scheme which used a feed rate of 1.8 gpm. At high velocity cases the opposite is true, the 3 gpm case produces smaller melt pools than the scaled feed scheme which is providing above 3 gpm of powder. The "best guess" measurement of all three feed rate schemes are compared in Figure 2-17. Scaling the powder feed rate had a more consistent melt pool shape when compared to the constant 3 gpm cases and had better agreement with both the finite element results and the no added material cases. While scaling powder feed rate with velocity proved better than no scaling, scaling feed rate with the expected melt rate ($Melt\ rate = A \times v$) may provide a further improvement. This would scale material feed rate with the rate that material is melted.

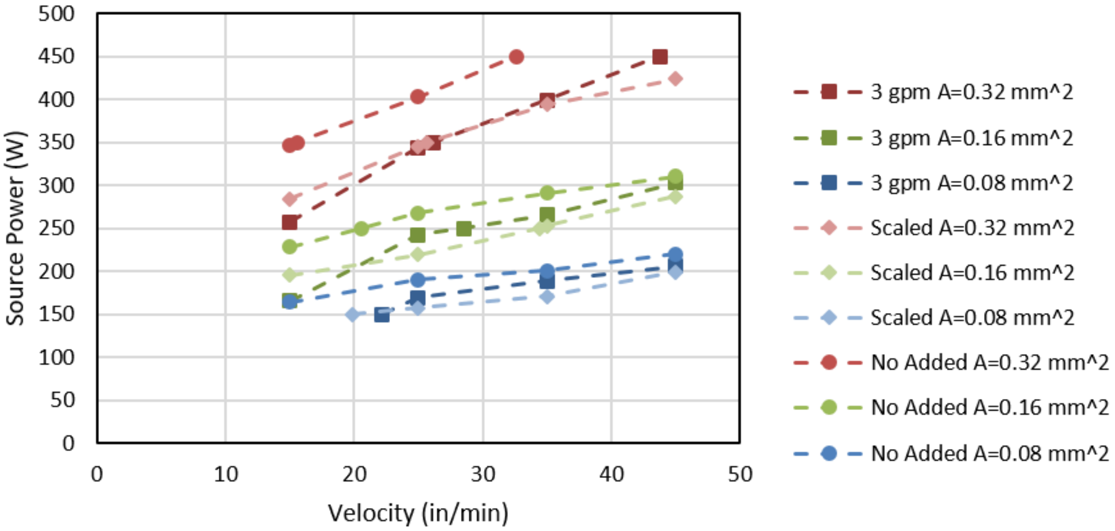

Figure 2-17: Power-velocity process map of melt pool cross-section area comparing different feed rate scenarios in the LENS process.

As with the Sciaky process, widths and depths have been process mapped for the LENS laser powder feed process. Figure 2-18 shows process maps of melt pool width on the left and melt pool depth on the right. From top to bottom, process maps show data for the constant 3 gpm feed rate, scaled feed rate, and no-added material. All values for constant width and depth match values used with melt pool area for an assumed semi-circular melt pool. Plotted points are found by linearly interpolating experimental "best guess" measurements and are bordered by dotted lines showing uncertainty from outer limit and inner limit boundaries for the melt pools.

Melt pool widths best matched finite element results with effective absorptivities of 0.59 for constant 3gpm, 0.56 for scaled feed, and 0.58 for no added material. R^2 values for the three cases are 0.8434, 0.9542, and 0.9311 respectively. These absorptivity values are significantly different than the values between 0.31 and 0.36 used in area measurements signaling that melt pool widths are larger than expected for the measured cross-sectional areas. In all cases, widths were too large to generate an experimental data set for the smallest constant width line of 0.45 mm. Different powder feed rates appear to have little to no effect on melt pool width.

Melt pool depth did not show consistent agreement with finite element results. The constant 3 gpm case, scaled feed rate case, and no added material case matched best with FEA results using effective absorptivities of 0.29, 0.31, and 0.21 respectively with r^2 values of the center width and depth cases (W=0.64 mm, D=0.32 mm) are 0.5846, 0.7133, and 0.7059. Comparison between the constant 3 gpm and scaled feed cases (3 gpm has higher feed below 25 in/min and lower feed above) indicates that increasing feed rate increases melt pool depth. As material is added to the surface of the melt pool and the deposition grows taller, conduction pathways to draw heat away from the melt pool become restricted. This allows the molten material to remain longer and more powder to be added to the surface of the melt pool, increasing its measured depth. Another phenomenon observed in melt pool depth process maps is comparatively poor alignment between experimental and finite element results in the constant 3 gpm case due to the feed rate not being properly balanced with melt pool size to give consistent results. Differences in absorptivities used for melt pool area, width, and depth are again contributed to small spot sizes and near semi-circular melt pools from simulations.

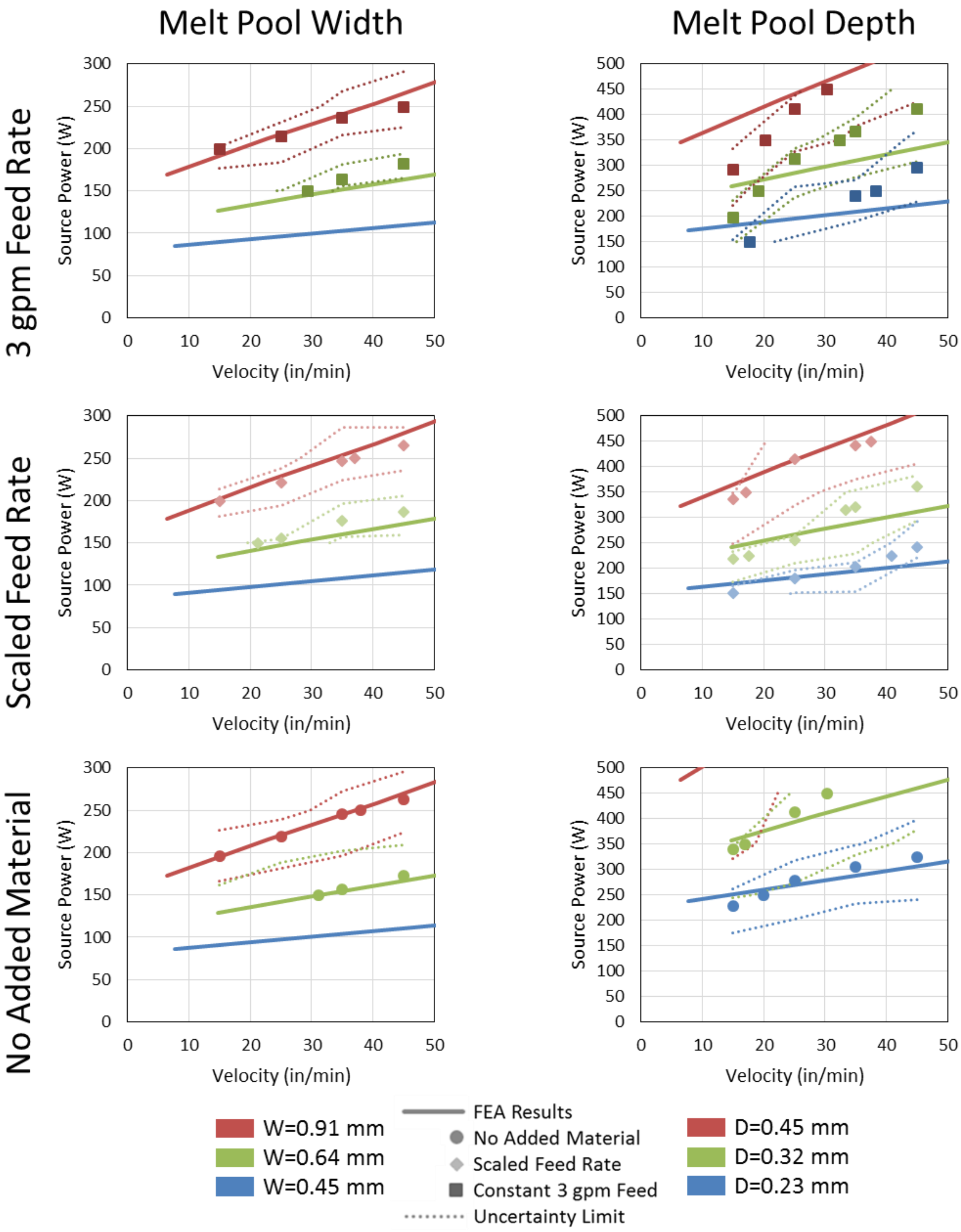

Figure 2-18: Process maps of melt pool widths and depths in the LENS process for different material feed rate scenarios

Variability was again captured for melt pool width by measuring melt pool widths as viewed from above. Appendix 2 contains data comparing width measurements from above and those from cross sections. Standard deviations measured from above widths are typically below 5% of the average melt pool width in all three feed rate schemes. This quantitatively backs up observations of smooth and consistent melt pools in single bead experiments from the laser powder feed process.

2.3.3 Microstructure Control in the Sciaky Electron Beam Wire Feed Process

Where process mapping of the Sciaky electron beam wire feed process was an extension Soylemez and Fox, control of microstructure in the process will look to apply the same relationships developed by Gockel [81]. This section will focus on relationships between melt pool dimensions and Ti-6Al-4V prior beta grain size initially in single bead deposits throughout processing space, then in a single layer and multi-layer pad deposits of select parameter combinations. Knowledge of how melt pool dimensions impact microstructure can work hand in hand with melt pool monitoring to control microstructure throughout parts built with AM. Results and trends are compared to those found by Gockel and Narra [81] [89].

Average prior beta grain width measurements are plotted against effective melt pool width to compare to the relationship previously developed by Gockel. Effective melt pool width is the melt pool width calculated from area assuming a semicircular melt pool. Figure 2-19 compares single bead results from this work to single beads measured by Gockel for NASA's EBF3 electron beam wire feed process. Both sets of experimental results show average prior beta grain size changing linearly with effective width; however, work by Gockel shows larger grain sizes for melt pools of similar melt pool width. Primary reasons for the disparity between the two experiment sets are the use of different electron beam spot scanning strategies or microstructural differences in the substrate. Error bars from this work show the uncertainty in effective width and the 95% confidence interval for grain width. Error bars in work by Gockel show variation from multiple melt pools in average grain size and effective width.

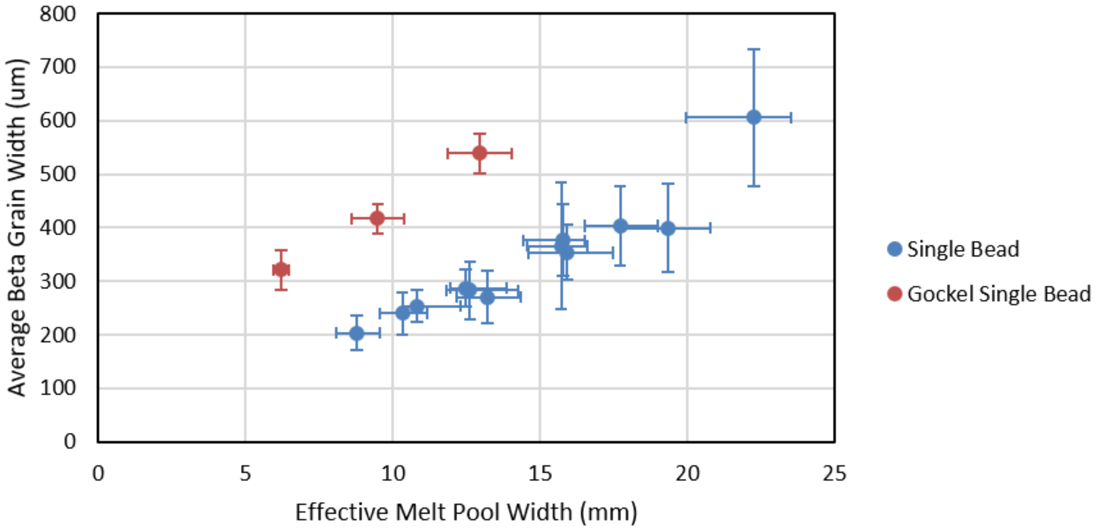

Figure 2-19: Relationship between prior beta grain width and effective melt pool width in electron beam wire feed processes

Experiments were also completed to identify if the trend observed in single bead deposits held up in bulk deposition geometries. Due to space constraints, only three power-velocity combinations were deposited and analyzed for single-layer and multi-layer pads. Figure 2-20 compares prior beta grain width measurements in single beads with those measured in pads. The error bars showing uncertainty in effective width for the pad deposits are based on single bead measurements at each respective power-velocity combination. Single layer pads saw a modest increase in prior beta grain width when compared to single bead results and appears to have a similar trend when compared to single beads. Prior beta grain width measurements similarly appears to follow the same trend, but with much higher grain widths. The consistency in trend and increase in grain width for multi-layer deposits was similarly observed in the Arcam EB-PBF process by Narra et al [89].

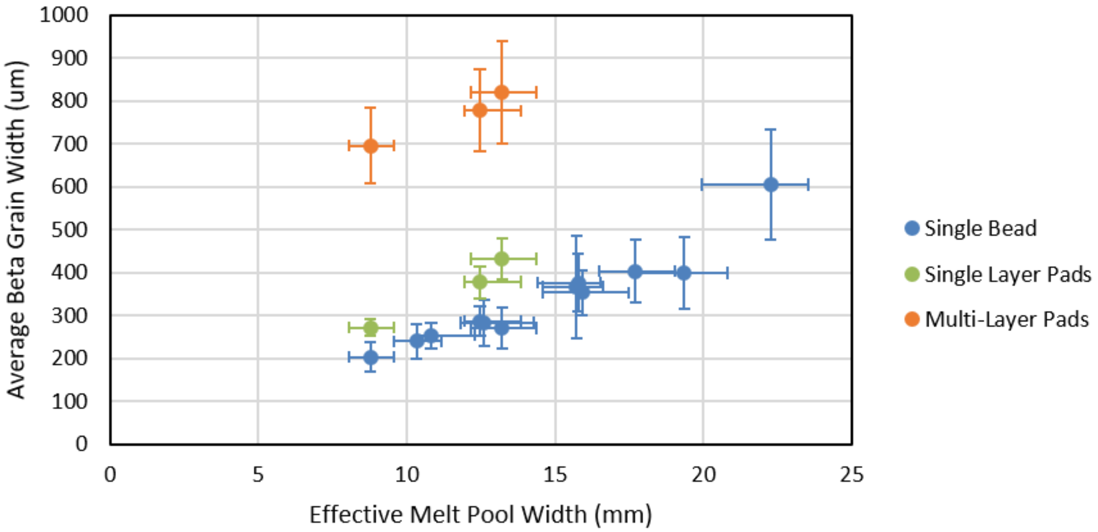

Figure 2-20: Relationship between prior beta grain width and effective melt pool width for different deposition geometries in the Sciaky electron beam wire feed process

2.3.4 Thermal Imaging and Microstructure Control in the LENS Process

Relationships between effective melt pool width and prior beta grain width in the electron beam wire feed and EB-PBF processes by Gockel do not hold up in the laser powder feed region of processing space. This is primarily due to a mismatch between trends of cooling rate and melt pool area near the origin on a power-velocity process map. Figure 2-21 displays experimental and simulation results showing a mismatch of cooling rate and prior beta grain size with melt pool area. At low velocities, melt pool area trends toward a y-axis intercept where a finite melt pool size is preset at zero velocity. Cooling rate trends toward the origin where a cooling of zero is present at zero velocity.

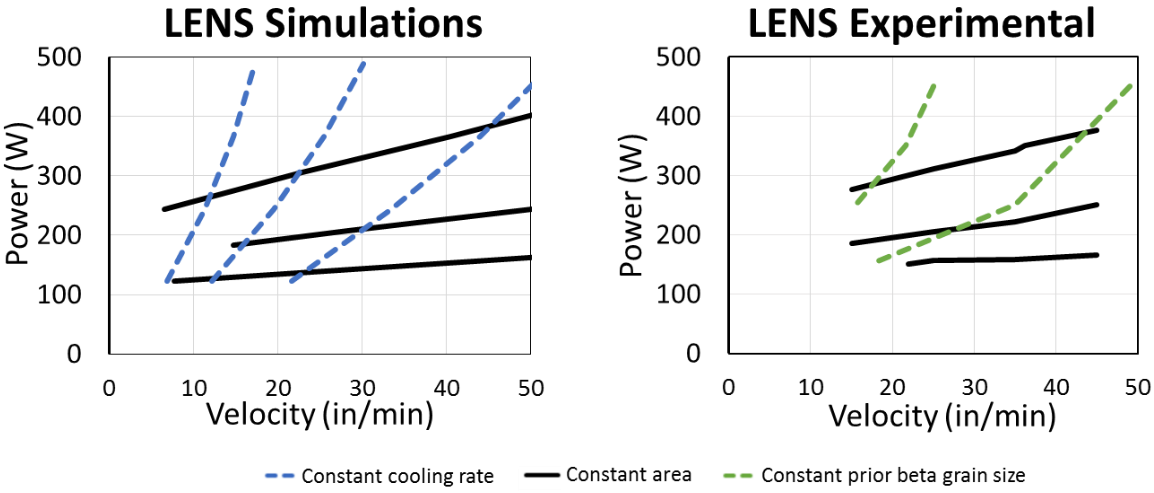

Figure 2-21: Trends for melt pool area, cooling rate, and prior beta grain size in the LENS laser powder feed process

Due to the inability to apply the previously used prior beta grain width-effective melt pool width relationship, a relationship between melt pool full length, velocity, and prior beta grain width was developed. Aspects of melt pool geometry viewed from above are particularly useful as they can be used with thermal imaging to monitor the melt pool during deposition. For this reason, full melt pool length was a desirable geometry when relations between melt pool width and microstructure were shown to be insufficient.

To test relationships between full length, velocity, and prior beta grain width, a thermal imaging feedback control system was set up by Stratonics at Penn State ARL on a LENS MR-7 machine. The system allowed a set full length to be controlled via changing laser power while at a fixed velocity. Experiments controlling melt pool length via thermal imaging were completed at 15 in/min, 30 in/min, and 45 in/min and lengths of 1.27, 1.78, and 2.29 mm. Figure 2-22 displays measured prior beta grain widths against full melt pool length for different lines of constant velocity.

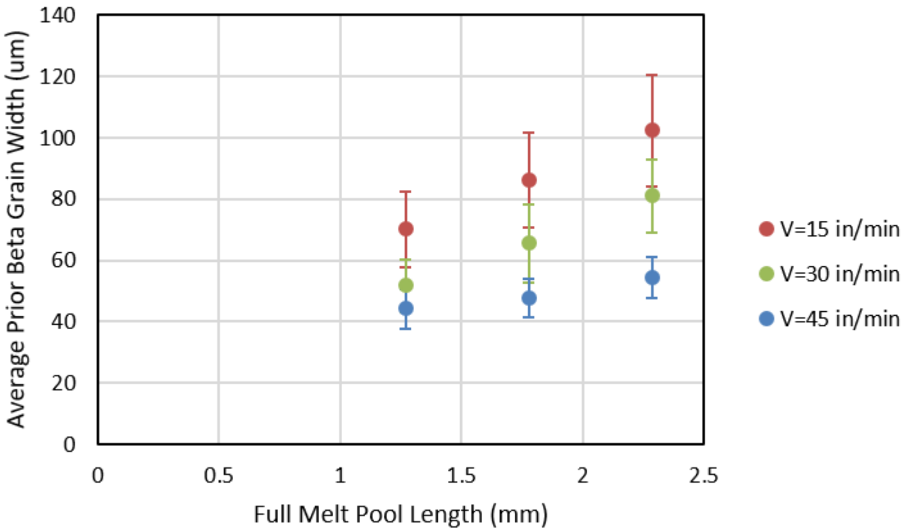

Figure 2-22: Prior beta grain width vs full melt pool length in the laser powder feed process

Error bars represent the 95% confidence interval for prior beta grain width. Unlike relationships used for the electron beam wire feed process, the relationships between melt pool geometry and microstructure in the laser powder feed process are also dependent on travel velocity. However, since velocity is a primary process parameter, prior beta grain size in Ti-6Al-4V can be indirectly controlled by directly controlling melt pool full length. This method and relationship has the potential to enable location specific microstructure control throughout actual parts.

2.4 Discussion

Key melt pool dimensions have been process mapped in the electron beam wire feed and laser powder feed process. In the electron beam wire feed process, experimental cross-sectional area measurements matched finite element results with an effective absorptivity of 0.89. When comparisons were made between cross-sectional area, width, and depth, there was a discrepancy between how sensitive the different dimensions were to power and velocity. Melt pool depth showed a greater sensitivity to the process parameters than area and melt pool width showed a lesser sensitivity. These differences in sensitivity are due to the use of a consistent spot size, the details of which are discussed later in Chapter 3:.

Process mapping in the laser powder feed process compared cross section dimensions in three different powder feed rate schemes. Experimental process maps of area matched no-added material finite element results well with effective absorptivities of 0.31 for no-added material, 0.36 for a scaled feed rate, and 0.35 for a constant 3 gpm feed rate. Increasing the powder feed rate was found to cause an increase in cross-sectional area. When process maps of depth and width were compared with area, similar differences in sensitivity to power and velocity were again observed. There were also significant differences in the effective absorptivities found for depth, width, and area showing that experimental melt pools are consistently shallower than the semi-circular melt pools created in simulations. Again, this can be contributed to spot size and is discussed in the following chapters. There were also larger variations in effective absorptivity across the different feed rate schemes for melt pool depth than melt pool width. This signals that feed rate has a significant effect on depth and has little effect on width.

Microstructure was analyzed in single bead and multi-layer deposits in the electron beam wire feed process and relations between melt pool geometry and prior beta grain width suggested by Gockel were verified. Measurements from single beads showed a linear relationship between prior beta grain width and effective melt pool width. The trend was generally parallel to results by Gockel, but shifted to lower grain sizes. The difference is likely due to differing substrate microstructure or other differences between the Sciaky process used in this work and NASA's EBF3 process used by Gockel. Measurements from single layer and multi-layer pads at three different power-velocity combinations showed similar trends at higher prior beta grain widths.

In the laser powder feed process trends found in the electron wire feed process were found to be non-applicable. New relationships between prior beta grain width, full melt pool length, and velocity were developed. Single bead deposits were generated by controlling laser power to maintain a desired full length at a specified velocity. Prior beta grain measurements formed different linear relationships between microstructure and full melt pool length for different velocities. The relationships developed were successfully used to guide a feedback control systems with the use of thermal imaging.

Chapter 3: The Effects of Spot Size on Melt Pool Dimensions

3.1 Overview

Spot size can play an important role in the development of melt pool geometry, the effects of which directly affect the quality of a part built using additive manufacturing. This chapter outlines how key melt pool dimensions change with increasing spot size independent of melt pool size, process, and alloy. Simulations are developed based on both analytical and finite element models for tophat and Gaussian beam profiles to understand melt pool behavior with different beam sizes. Experiments from various processes, alloys, and melt pool shapes show good agreement with simulation results to validate the models. Experiments can additionally be used to estimate spot sizes in different processes. The methods to estimate spot size are discussed and experimental results are fit to characteristic curves. Experimental estimates are also compared to beam measurements from the EOS M 290 process. Estimates of spot size can be used to guide focus changes to reliably predict melt pool geometry in additive manufacturing processes.

3.2 Methods

3.2.1 Modeling

Work in this chapter is a product of both finite element based and analytical based models. Finite element simulations used in spot size analysis are based on those used in Chapter 2:, and simulate top hat or Gaussian flux distributions. Analytically based models are evolutions of the Rosenthal model of a moving point heat source [91]. The Eagar-Tsai model simulates a moving heat source with a Gaussian heat source and is a modification of the Rosenthal model [93]. Another model was created to simulate a top hat heat source by using the principle of superposition with the original Rosenthal model. These models were used to identify how melt pool geometry changes with increasing spot size.

3.2.1.1 Finite Element Models

The finite element model used in this section was a slight modification on the model used for the laser powder feed process. The model simulates a distributed moving heat source on a large substrate that is long enough to reach steady state melt pool size and wide and deep enough to avoid edge effects and a symmetry boundary condition down the center of the melt pool. The heat flux is distributed across elements on the surface to make a semi-circular shape. The number of elements with applied heat flux is determined by stepping through elements in the X-direction and rounding to the nearest element in the Y-direction to create the correct shape. Two different flux distributions within the spot size were simulated. One model uses a tophat distribution where all flux values are set equal, and a second approximates a Gaussian distribution. The spot size value used from Gaussian distribution simulations follows the D86 width measurement technique commonly used to find laser beam diameter [113]. The distribution of the heat flux for a typical model is shown in Figure 3-1.

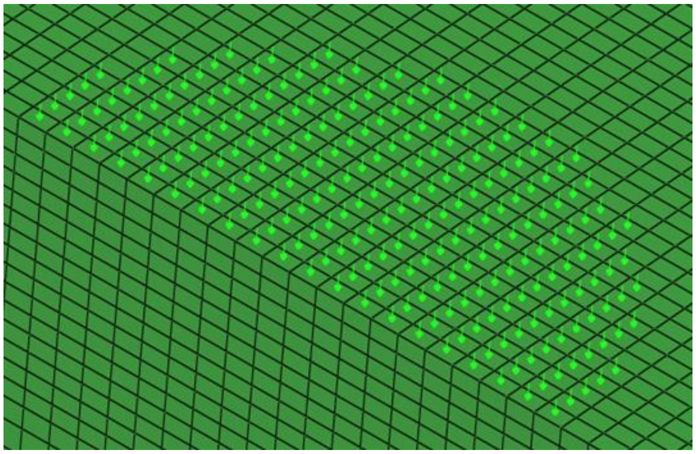

Figure 3-1: Flux distribution on the surface of a finite element model

The Gaussian heat source model extended the Gaussian profile out to two standard deviations, and amplitude is adjusted to provide the full power input. Since the Gaussian profile is fit onto a set of square elements, the smallest spot sizes used (4 element radius) had the largest percent error between the discrete and true distribution (25%). Other spot sizes simulated were multiples of 4 elements through the radius and have significantly decreased error in respect to modelling a Gaussian beam profile. Simulations of spot size span multiple processes and alloys. In all cases, the finite element models use temperature dependent thermal properties.

3.2.1.2 Rosenthal and Eagar-Tsai Models

In addition to finite element models, simpler models for tophat and Gaussian beam distributions were used to identify effects of increasing spot size. The models do not include temperature dependent properties or latent heat, but a solution can be found in a matter of seconds compared to hours or days. The first model, simulating a tophat distribution, is based off the moving heat source model developed by Rosenthal [91] shown in Eq. 3-1.

Eq. 3-1

$$T - T_0 = \frac{q}{2\pi k R} e^{-\frac{v(w+R)}{2\alpha}}$$

Where T is the temperature of the location of interest, T_0 is the preheat temperature, q is the input power, v is the travel velocity, k and α are thermal properties, and w and R specify the location. The equation gives the temperature at a specified location relative to a point heat source. To create a tophat heat source, multiple Rosenthal models are organized into a circular shape with 100 instances across the diameter. The principle of superposition is used to sum the solutions for a specified point in space. Melt pool boundaries are found by using the Newton-Raphson method and maximum width, depth, and area is found using the golden-section search method.

The Eagar-Tsai model was developed based on the Rosenthal model and simulates a moving heat source with a Gaussian distribution. Where the original Rosenthal model can be solved analytically, the derived Eagar-Tsai model in Eq. 3-2 must be solved numerically [93].

Eq. 3-2

$$\theta = \frac{n}{\sqrt{2\pi}} \int_0^{\frac{v^2 t}{2\alpha}} \frac{\tau^{-\frac{1}{2}}}{\tau + u^2} e^{-\frac{\xi^2+\psi^2+2\xi\tau+\tau^2}{2\tau+2u^2}-\frac{\zeta^2}{2\tau}} d\tau$$

Dimensionless temperature is represented by θ, and ξ, ψ, and ζ represent dimensionless distance in x, y, and z. Dimensionless time is represented by τ. *u* is a dimensionless heat source distribution parameter and *n* is an operating parameter that includes power, velocity, and thermal properties. The integral was solved numerically with the trapezoid method, and melt pool boundaries and maximum geometry values were found via the Newton-Raphson and golden-section search methods as with the tophat distribution model.

3.2.1.3 Model Settings used in Spot Size Simulations

Simulations were run for various processes, alloys, and process parameter settings. Table 2 shows the model settings used to generate results from simulations where spot size was varied. The provided L_0/D_0 value is the melt pool length to depth ratio found at a point heat source, the T_{prop} value is the temperature at which thermal properties are used for the Rosenthal and Eager-Tsai models. T_{prop} is left blank for finite element simulations since temperature dependent properties were used.

Table 2: Model settings used for simulations of spot size increases

L_0/D_0	Process	Alloy	Model	Power (W)	Velocity (mm/s)	Background Temp (K)	T_{prop} (K)
1.25	Laser powder bed fusion (L-PBF)	AlSi10Mg	Rosenthal/ Eagar-Tsai	100	845	308	500
1.25	Laser powder feed (LPF)	17-4 PH stainless steel	Rosenthal/ Eagar-Tsai	85	30	308	1000
1.25	Laser powder feed (LPF)	17-4 PH stainless steel	Finite Element	87.5	30	293	▨
1.25	Laser powder bed fusion (L-PBF)	AlSi10Mg	Finite Element	50	660	308	▨
2.5	Laser powder bed fusion (L-PBF)	Ti-6Al-4V	Rosenthal/ Eagar-Tsai	60	910	308	1800
2.5	Laser powder feed (LPF)	316L stainless steel	Rosenthal/ Eagar-Tsai	470	50	308	1000
2.5	Laser powder feed (LPF)	316L stainless steel	Finite Element	400	35	293	▨
2.5	Laser powder bed fusion (L-PBF)	Ti-6Al-4V	Finite Element	40	525	308	▨
5	Laser powder bed fusion (L-PBF)	CoCr	Rosenthal/ Eagar-Tsai	100	1075	308	950
5	Electron beam wire feed (EBWF)	IN 625	Rosenthal/ Eagar-Tsai	3000	21.2	293	1027
5	Electron beam wire feed (EBWF)	Ti-6Al-4V	Finite Element	3880	21.2	293	▨
5	Laser powder bed fusion (L-PBF)	CoCr	Finite Element	95	476	308	▨
10	Electron beam powder bed fusion (EB-PBF)	CoCr	Rosenthal/ Eagar-Tsai	500	450	1073	1175
10	Electron beam wire feed (EBWF)	Ti-6Al-4V	Rosenthal/ Eagar-Tsai	20000	18.2	293	935
10	Electron beam wire feed (EBWF)	Ti-6Al-4V	Finite Element	20000	17.3	293	▨
10	Electron beam powder bed fusion (EB-PBF)	Ti-6Al-4V	Finite Element	600	265	1073	▨
20	Electron beam wire feed (EBWF)	IN 625	Rosenthal/ Eagar-Tsai	25000	33.9	293	850
20	Electron beam powder bed fusion (EB-PBF)	Ti-6Al-4V	Rosenthal/ Eagar-Tsai	1500	1375	1073	1800
20	Electron beam powder bed fusion (EB-PBF)	Ti-6Al-4V	Finite Element	1430	423	1073	▨
20	Electron beam wire feed (EBWF)	Ti-6Al-4V	Finite Element	32000	42.3	293	▨

3.2.2 Experiments

Experiments were completed in five different processes and five different alloys shown in Table 3. In all cases, specific power-velocity combinations were chosen for single bead deposits, and spot size was varied incrementing from a focused to defocused beam. Measurements of melt pool cross section width, depth, and area are used to compare against models. Since trends are the most important aspect in this chapter, only the "best guess" measurements will be used as defined in section 2.2.3.

Table 3: Spot size experiment processes, alloys, and process parameters

Process	Alloy(s)	Power	Velocity	Focus Setting Range	Expected L_0/D_0
Sciaky Electron Beam Wire Feed	Ti-6Al-4V	10 kW	19.0 mm/s	0.12 to 0.27 in	15
		25 kW	12.7 mm/s	0.25 to 0.60 in	20
Arcam S12 EB-PBF	Ti-6Al-4V	670 W	270 mm/s	-20 to 38 mA	5
		670 W	1100 mm/s	0 to 26 mA	10
		670 W	3700 mm/s	0 to 21 mA	20
	IN718	670 W	90 mm/s	10 to 60 mA	5
		670 W	400 mm/s	-8 to 52 mA	10
		670 W	1300 mm/s	0 to 38 mA	20
3D Systems ProX 200 L-PBF	Stainless Steel (304, 316L, 17-4 PH)	300 W	500 mm/s	0 to 22 mm	5
		215 W	750 mm/s	0 to 15 mm	5
		130 W	1400 mm/s	0 to 5.5 mm	5
		300 W	2400 mm/s	0 to 8 mm	10
3D Systems ProX 300 L-PBF	Stainless Steel (304, 316L, 17-4 PH)	400 W	600 mm/s	0 to 6.5 mm	5
		205 W	1200 mm/s	0 to 21 mm	5
		400 W	3000 mm/s	0 to 11 mm	10
EOS M 290 L-PBF	Ti-6Al-4V	80 W	500 mm/s	0 to 14 mm	2.5
		370 W	450 mm/s	0 to 28.5 mm	5
		270 W	580 mm/s	0 to 19 mm	5
		170 W	910 mm/s	0 to 11.5 mm	5
		370 W	1900 mm/s	0 to 18 mm	7.5
		330 W	2150 mm/s	0 to 15.5 mm	7.5
		270 W	2550 mm/s	0 to 13 mm	7.5

Experiments in the Sciaky electron beam wire feed process held individual process parameters power, velocity, and deposition rate constant. Values under “Focus Setting Range” represent the actual spot size created by scanning a focused electron beam into concentric circles. To modify the spot size, the concentric circles are expanded or contracted. A problem encountered at large spot sizes and small melt pool depths is that the fed wire can become a limiting factor if it starts contacting the base of the substrate at the bottom of the melt pool. At small spot sizes, keyhole mode melting was present which is a phenomenon not modeled in this work. Keyholing melt pools are therefore not included in the analysis of spot size effects on geometry, but are discussed in Chapter 4:.

Experiments in the electron beam and laser powder bed fusion processes were all completed without a powder layer to remove an additional variable that may have an influence on the results. In the Arcam EB-PBF process, spot size can be adjusted by changing the focus offset parameter that changes the current in the focusing coils for the electron beam. Spot size was also affected by the power in this process, so all experiments were completed at the same power, 670 W. In the 3D systems ProX 200 and 300 L-PBF machines, a defocus parameter can be used to change the spot size. The parameter changes the focus plane of the laser and is changed in units of millimeters. The EOS M 290 machine does not have any spot size adjustments available to general users, but for single bead experiments, spot size can be increased by dropping the build plate. Therefore, “Focus setting range” refer to how far the build plate had been dropped to deposit the layer. While spot sizes are not an available parameter on the EOS M 290, it was an available parameter on older models.

Cross-sectional dimensions for no-added melt pools in the powder bed processes commonly distorts from the original shape due to fluid flow and surface forces. The melt pool area viewed from the cross section can also be increased or decreased by the bead up phenomenon [74]. In these cases the melt pool dimension measurement neglects the surplus or dearth of material present in the cross section. Figure 3-2 shows how melt pools with these conditions are measured in this work.

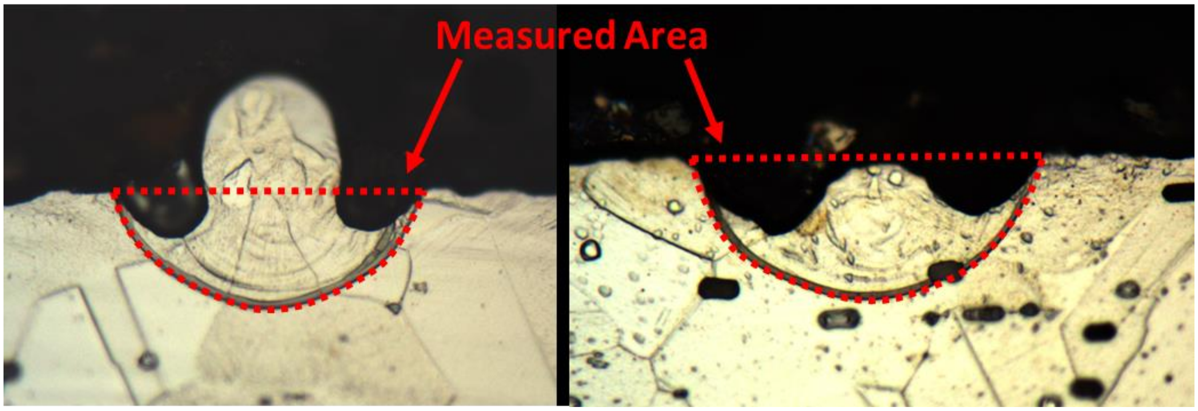

Figure 3-2: Melt pool area measurements for deformed no-added material melt pools

3.2.3 Normalization

In order to compare changes in dimensions across different melt pool sizes and alloys, melt pool dimensions (W, D, A, etc.) were normalized by their value at a point heat source (W_0, D_0, A_0, etc.). Spot size (σ) is normalized by the respective melt pool width at a point heat source. After normalization, geometry changes grouped together by melt pool aspect ratio, which can be represented by the length to depth ratio (L_0/D_0). Length in this case is measured from the point of maximum depth. For experiments, point source values are based on values from models, or if model results are unavailable, they can be determined from the melt pool cross section deposited with the smallest spot size that does not cause keyhole mode melting.

In the case of an unknown spot size, the depth to width ratio (D/W) of the melt pool cross section can be used to place experimental points on the normalized spot size (σ/W_0) axis (Figure 3-3). This method can also be used in conjunction with the point source melt pool width to back out estimates for actual spot sizes in the process. Estimated spot size values from the EOS M 290 experiments are compared against measured values in section 3.3.3.

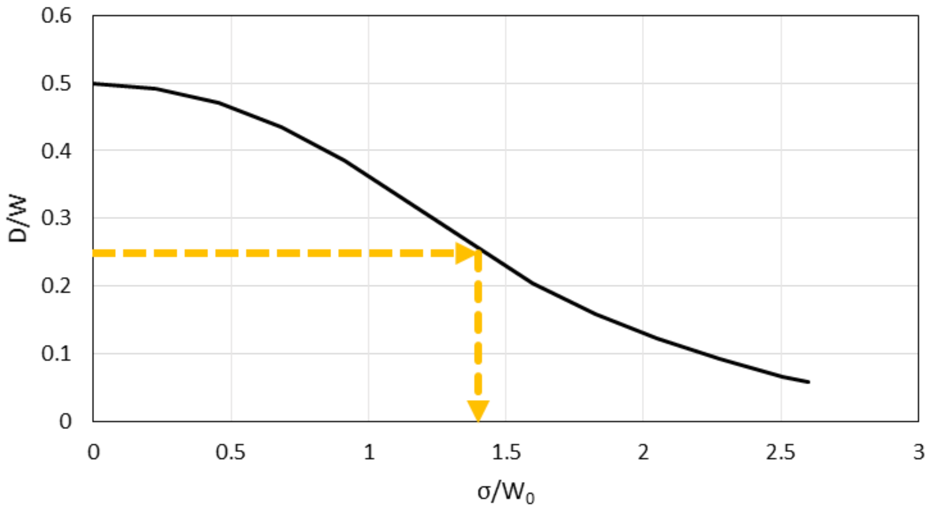

Figure 3-3: Example of identifying the normalized spot size based on width to depth ratio

3.3 Results

The focus of this chapter is on the relationships between certain melt pool dimensions and spot size. Trends in cross sectional width, depth, and area are developed for finite element and Rosenthal based models. Experimental measurements are compared against model results to verify the identified trends for different melt pool geometries. Backed-out spot size estimates based on experimental measurements and developed trends are compared to measurements in the EOS M290 and Sciaky processes. Additionally, estimated spot sizes are presented for the Arcam and 3D Systems processes.

3.3.1 Trends from Models

Simulations were completed for particular power-velocity combinations for selected processes and alloys to develop trends for how melt pool dimensions change with increasing spot size. Trends for normalized melt pool width from finite element and Rosenthal based models for tophat and Gaussian beam distributions are shown in Figure 3-4. Melt pool width (W) is normalized by the point source melt pool width (W_0). Spot size (σ) is also normalized by the point source melt pool width to create the normalized spot size parameter used throughout this section. For all models and L_0/D_0 ratios, melt pool width increases with increasing spot size before collapsing as material stops being melted. Different L_0/D_0 lines follow a similar initial trends before lower L_0/D_0 values break off from trends followed by higher length to depth ratios. Results from tophat models show a greater increase in melt pool width and a longer shared trend between different L_0/D_0 ratios. In general, the models show that width in melt pools of different alloys and processes follow the same trends with increasing spot size. Differences between lines of the same L_0/D_0 label are primarily due to slight differences between the actual L_0/D_0 values of the process parameters used in the models.

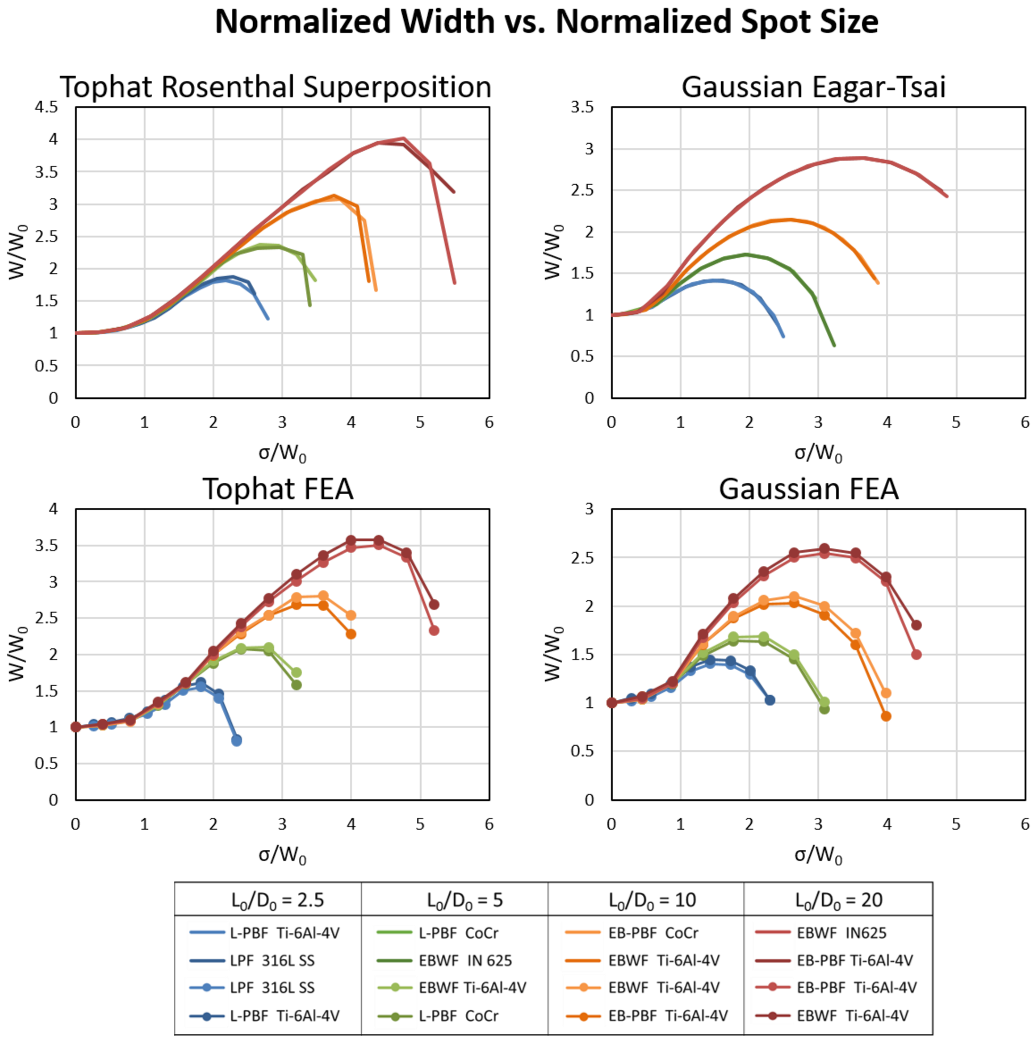

Figure 3-4: Normalized melt pool width vs. normalized spot size for different models

Melt pool depth is normalized by the point source depth (D_0) and plotted against normalized spot size in Figure 3-5. In all models and L_0/D_0 cases, normalized melt pool depth decreases continuously with increasing spot size. For normalized depth, tophat and Gaussian beam profiles give very similar results. As with normalized width results, melt pools with smaller L_0/D_0 values have a faster dropping normalized depth and larger L_0/D_0 values all follow a similar trend before separation. It should also be noted that in expanded spot sizes, the location of maximum depth and width occur at different locations in the melt pool. The point of maximum width occurred ahead of the point of maximum depth regardless of alloy, process, and L_0/D_0 ratio. The difference in location can be attributed to how the heat is applied to the two different areas. The width of the melt pool is influenced by the width of the beam inputting heat into the system. Maximum depth is an evolution of the maximum temperature found at the surface, which is located at the back of the beam spot where materials has been heated by the passing heat source. The maximum heat applied to the material in the direction of melt pool width occurs ahead of the point of maximum temperature, thus developing the maximum width ahead of the maximum depth.

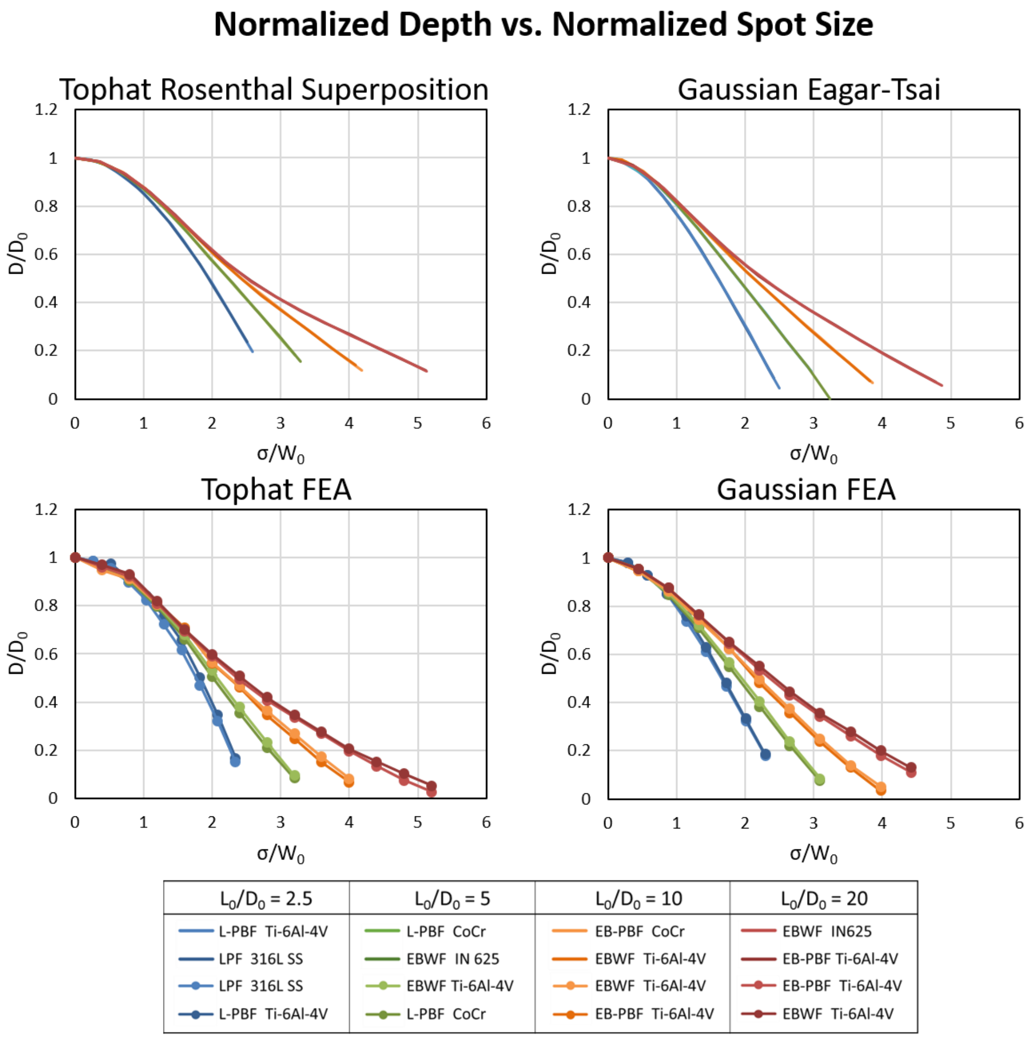

Figure 3-5: Normalized melt pool depth vs. normalized spot size for different models

Cross-sectional area is a combination of both melt pool width and depth. Since melt pool width and depth have differing trends with increasing spot size, normalized melt pool area exhibits a more mild response to normalized spot size (Figure 3-6). Melt pools with small L_0/D_0 ratios are relatively unaffected by increasing spot size before dropping. Melt pools with large L_0/D_0 ratios show an increase in melt pool area before decreasing, larger L_0/D_0 ratios have a greater increases in area. As seen in normalized width plots, a tophat heat source results in larger potential increases in area when compared to a Gaussian profile.

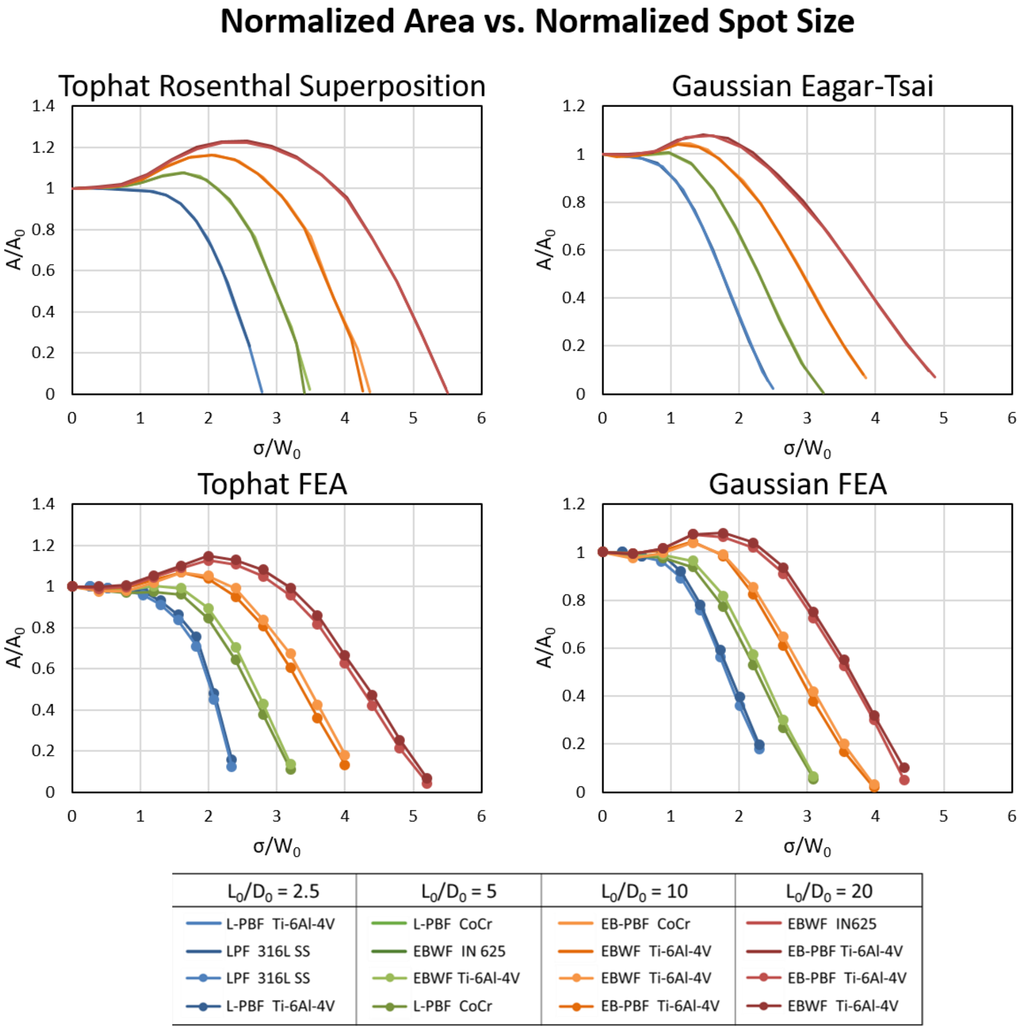

Figure 3-6: Normalized melt pool cross-sectional area vs. normalized spot size for different models

Depth to width ratios observed in model results are presented in Figure 3-7. Increases in width and decreases in depth combine to cause quick decreases in the depth to width ratios. All curves follow the same general trend until each L_0/D_0 lines approaches insufficient power density to melt. Since the y-axis in these plots does not require knowledge of a point source dimension, they can be very useful to determine a normalized spot size for experimental points when beam sized are unknown. These plots have been key to relating experimental and simulation results.

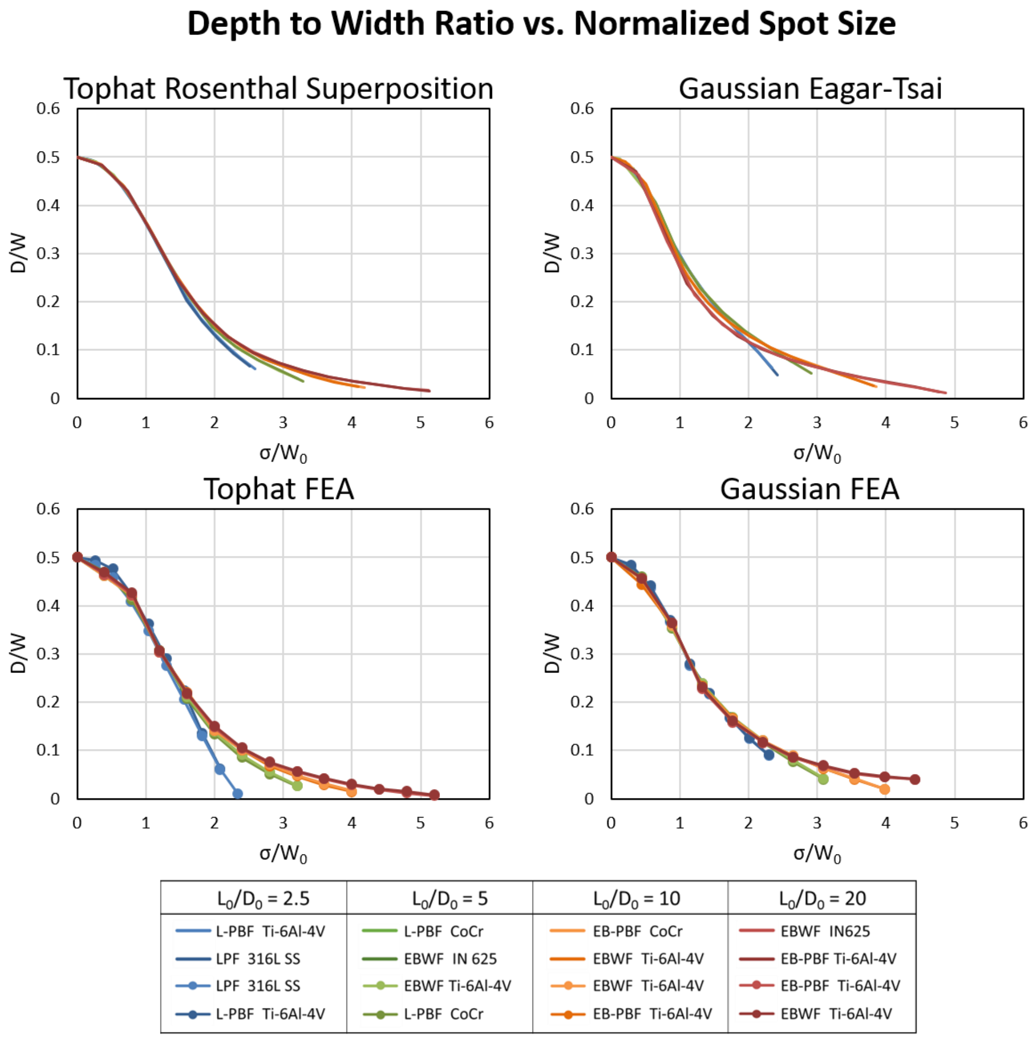

Figure 3-7: Width to depth ratio vs. normalized spot size for different models

3.3.2 Single Bead Experiments

Single bead experiments were deposited to verify the trends observed in simulations. In this section, all experiments are compared for the tophat and Gaussian beam profiles modeled in finite element simulations. This section will display experiments from L_0/D_0 ratios of 2.5, 5, 10, and 20. Additional experiment sets are plotted in Appendix 3. Error bars in this section show the uncertainty in point source dimensions (W_0, D_0, and A_0) that are used to normalize experimental width, depth, and area measurements.

Experiments from the EOS Ti-6Al-4V, 80W, 500 mm/s, and expected 2.5 L_0/D_0 case were measured and normalized based on a W_0 value of 113 µm. Spot sizes for these experiments are based on measurements taken at 40 W in the EOS M 290 machine at CMU [114] [115]. The normalized experimental measurements are compared against finite element results in Figure 3-8, Figure 3-9, and Figure 3-10. Across the three measured melt pool dimensions, experiments match poorly with trends created from an assumed tophat beam distribution. Better agreement is seen between experimental measurements and simulation results from an assumed Gaussian beam profile. While there is some mismatch in the normalized depth and width experiments and simulation results, experimental results for normalized area closely matched simulation results.

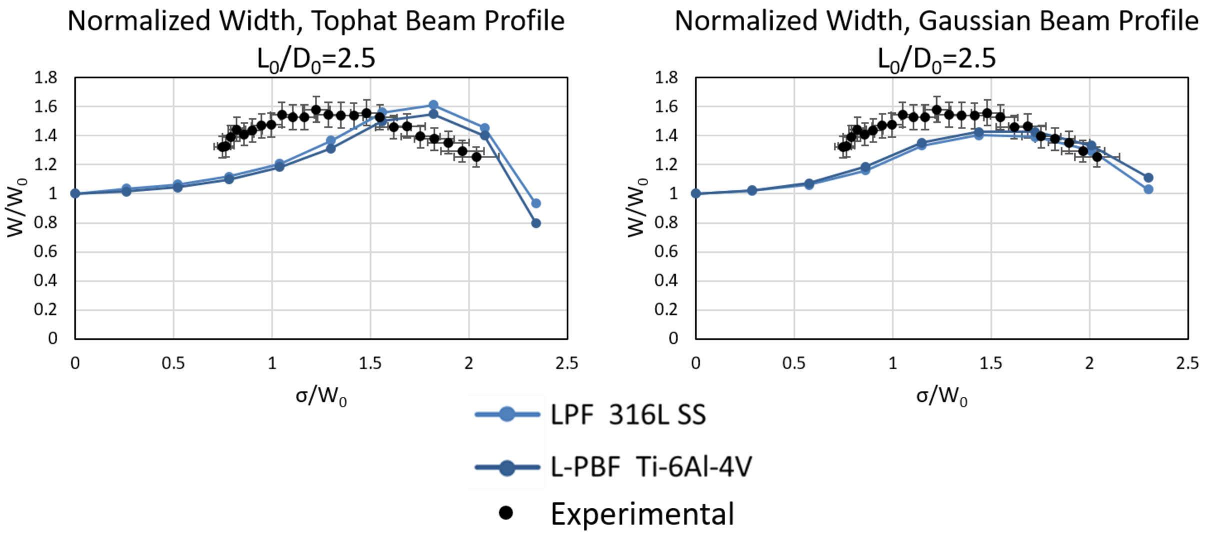

Figure 3-8: EOS L-PBF, Ti-6Al-4V, 80W, 500 mm/s experimental normalized width measurements compared with finite element results for an L_0/D_0 ratio of 2.5

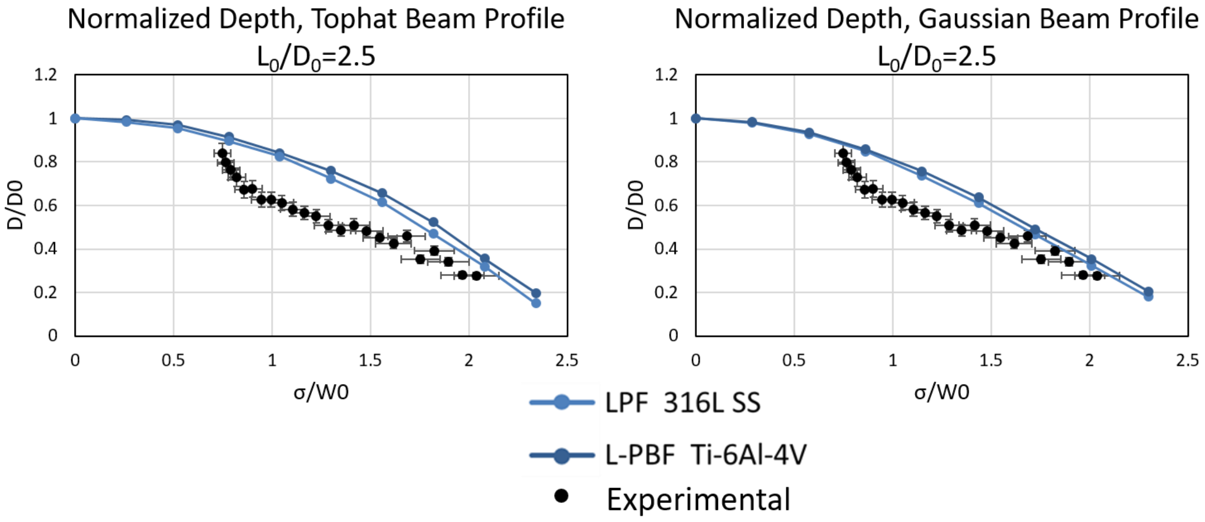

Figure 3-9: EOS L-PBF, Ti-6Al-4V, 80W, 500 mm/s experimental normalized depth measurements compared with finite element results for an L_0/D_0 ratio of 2.5

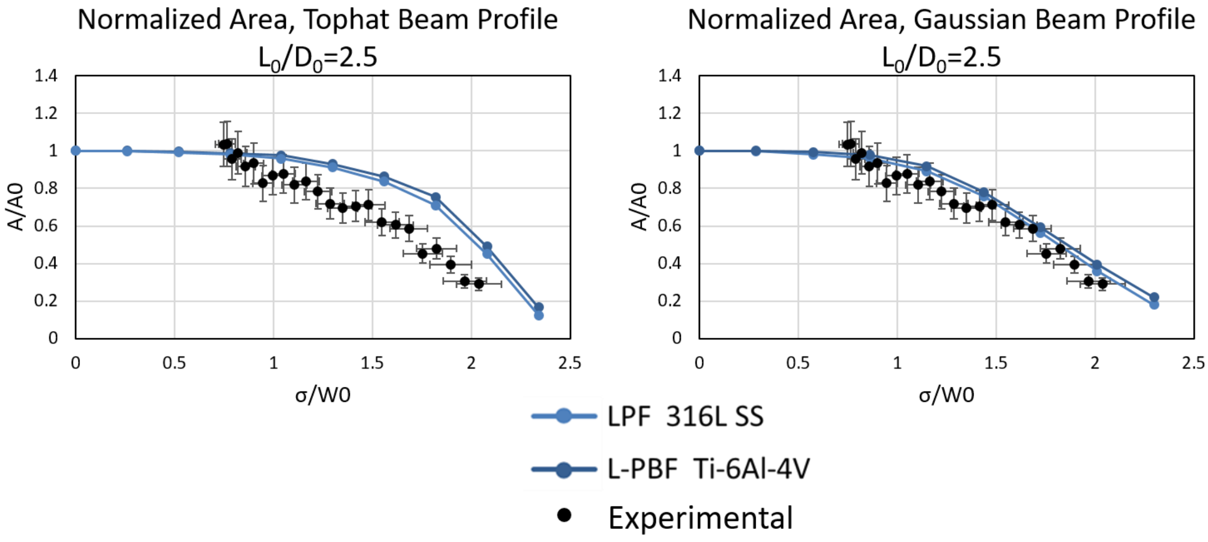

Figure 3-10: EOS L-PBF, Ti-6Al-4V, 80W, 500 mm/s experimental normalized area measurements compared with finite element results for an L_0/D_0 ratio of 2.5

Experiments from the Arcam S12 EB-PBF Ti-6Al-4V 670W, 1100 mm/s case had a projected L_0/D_0 and were measured and normalized based on a W_0 value of 835 µm. Experimental spot size values in these plots are based on trends created from backed out spot sizes from six experiment sets in the process. The backed out values and best fit is discussed in section 3.3.3. Comparison between normalized experimental and finite element results for width, depth, and area are presented in Figure 3-11, Figure 3-12, and Figure 3-13.

In the plots for normalized melt pool width, experimental measurements follow similar trends to those observed in simulations. For normalized melt pool width and depth, experimental measurements agree well with simulation results from both an assumed tophat and Gaussian beam intensity profile. In the case of melt pool area, good agreement is again observed for both a tophat and Gaussian beam profile, but agreement with a Gaussian profile is slightly improved. In general, trends from finite element simulations do a very good job of describing changes in melt pool dimensions for this experiment set.

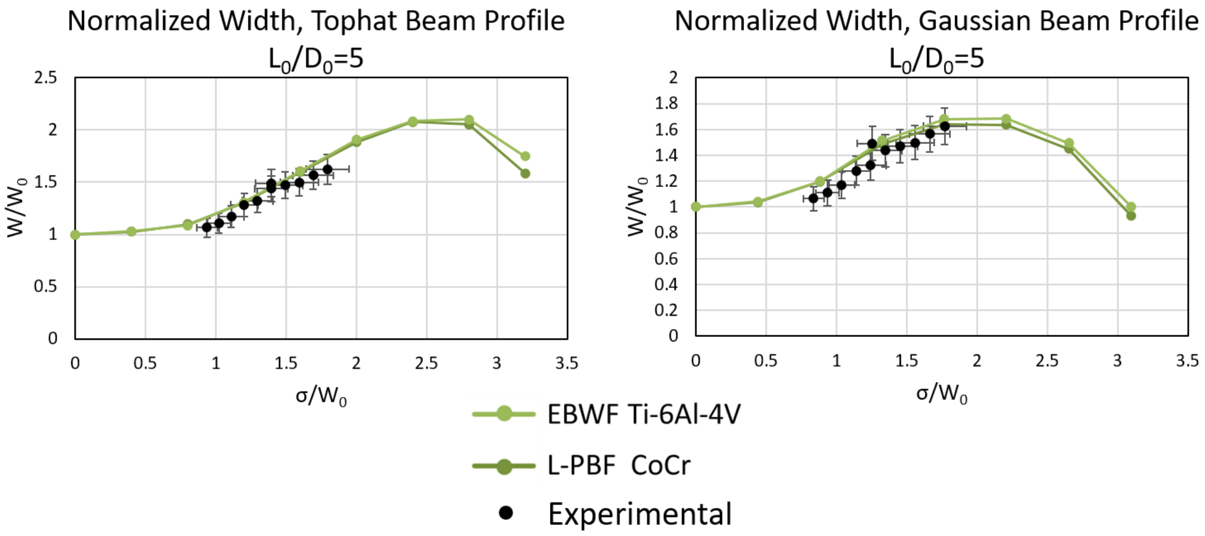

Figure 3-11: Arcam S12 EB-PBF, Ti-6Al-4V, 670W, 1100 mm/s experimental normalized width measurements compared with finite element results for an L_0/D_0 ratio of 5

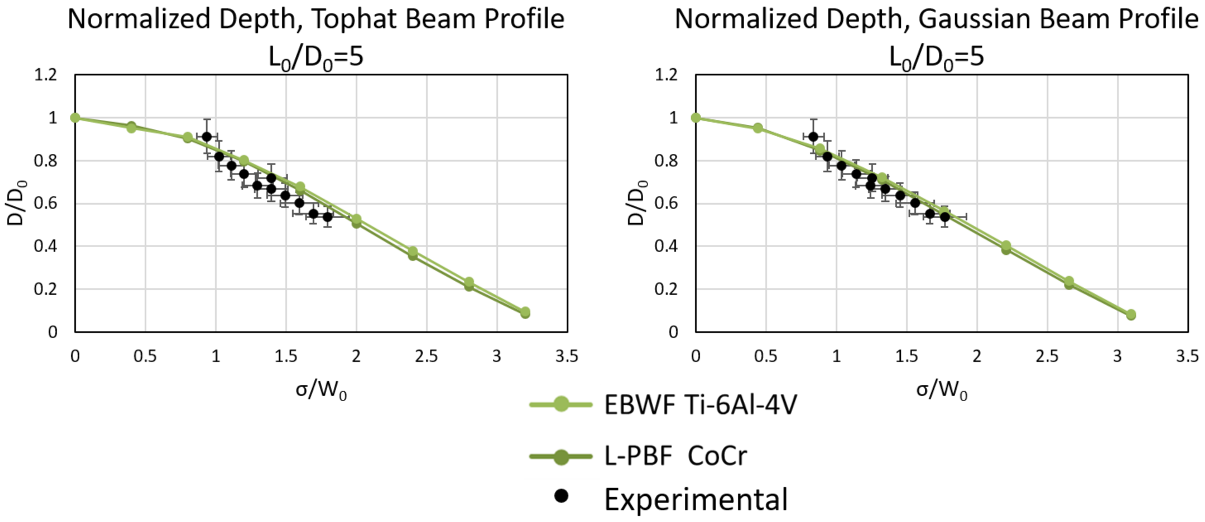

Figure 3-12: Arcam S12 EB-PBF, Ti-6Al-4V, 670W, 1100 mm/s experimental normalized depth measurements compared with finite element results for an L_0/D_0 ratio of 5

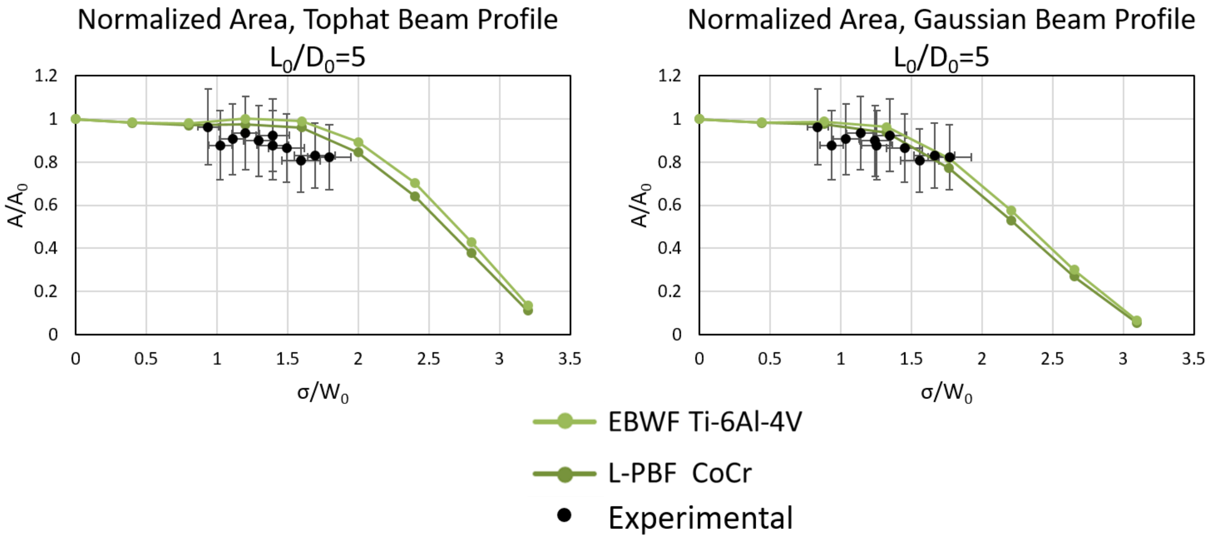

Figure 3-13: Arcam S12 EB-PBF, Ti-6Al-4V, 670W, 1100 mm/s experimental normalized area measurements compared with finite element results for an L_0/D_0 ratio of 5

Experiments from the 3D Systems ProX 200 L-PBF process performed at 300 W and 1400 mm/s with an expected L_0/D_0 of 10, were measured and normalized based on a W_0 value of 71 µm. Experimental spot size values in these plots are based on trends created from backed-out spot sizes from twelve experiment sets in the process. The backed-out values and best fit are discussed in section 3.3.3. Comparison between normalized experimental and finite element results for width, depth, and area are presented in Figure 3-14, Figure 3-15, and Figure 3-16.

For normalized width, experimental results are a poor match with simulation results based on a tophat beam profile. However, good agreement is observed between experiments and simulations results using a Gaussian beam profile. For normalized melt pool depth, good agreement is seen between experimental measurements and simulation results for both a tophat and Gaussian beam distribution. Normalized melt pool area again shows improved agreement between experiments and Gaussian simulation results when compared to tophat simulation results.

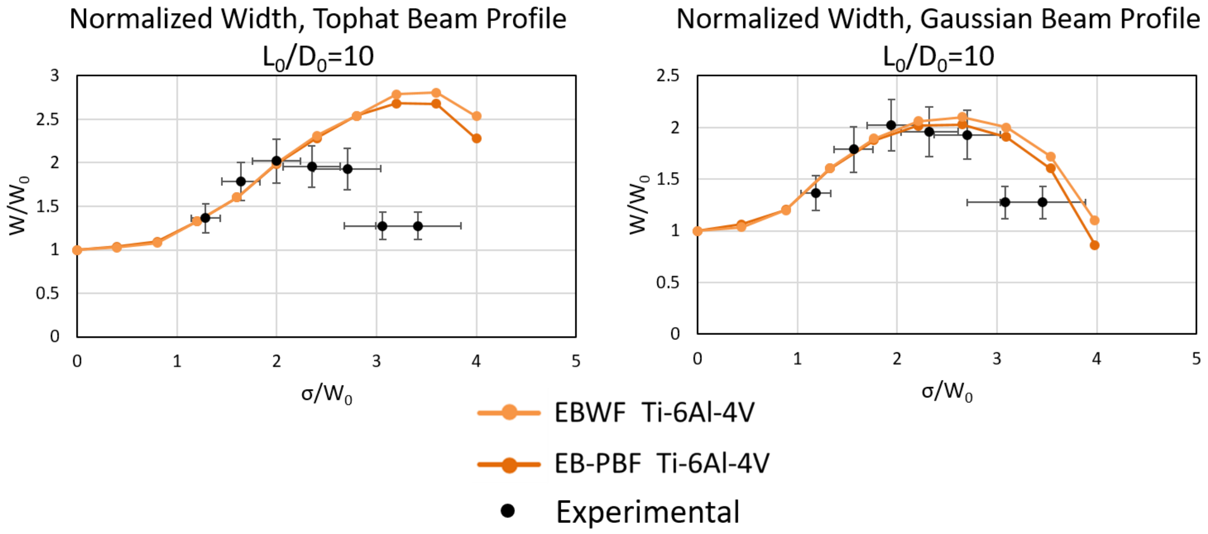

Figure 3-14: 3D Systems ProX 200 L-PBF, 17-4 PH stainless steel, 300 W, 1400 mm/s experimental normalized width measurements compared with finite element results for an L_0/D_0 ratio of 10

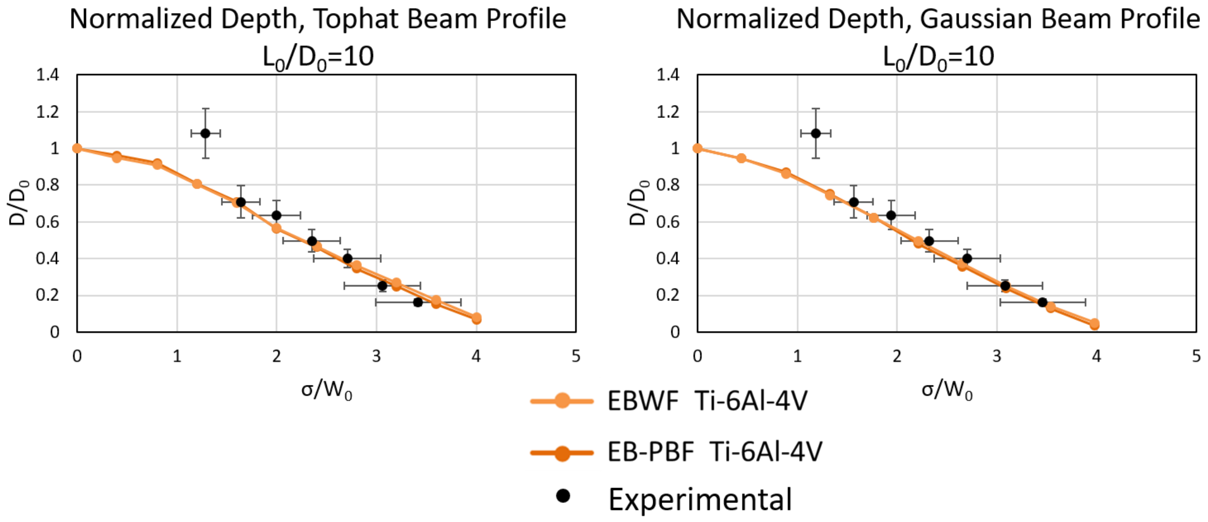

Figure 3-15: 3D Systems ProX 200 L-PBF, 17-4 PH stainless steel, 300 W, 1400 mm/s experimental normalized depth measurements compared with finite element results for an L_0/D_0 ratio of 10

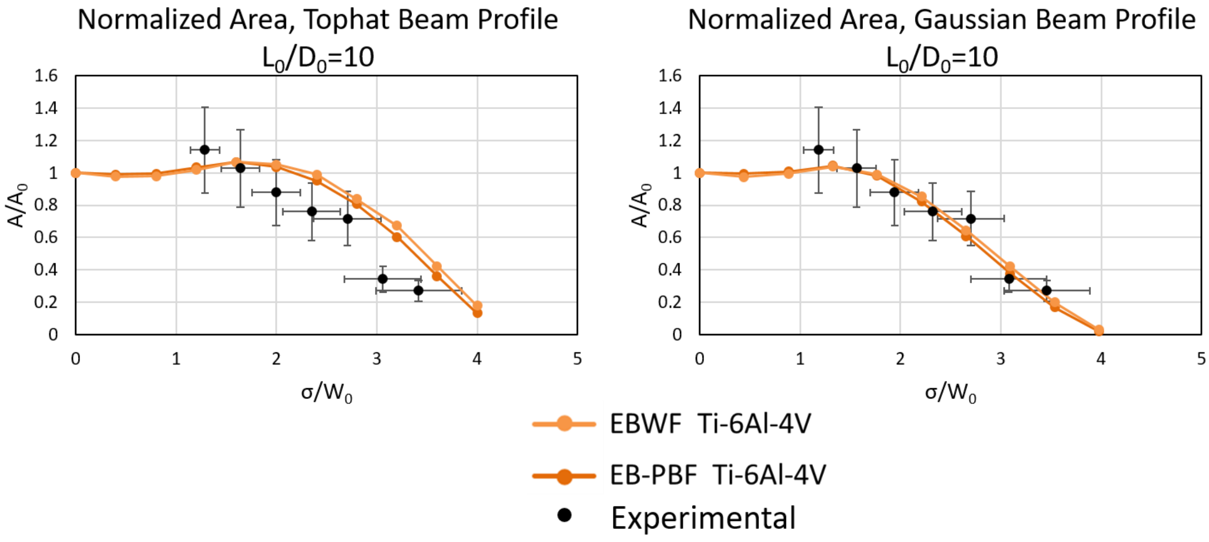

Figure 3-16: 3D Systems ProX 200 L-PBF, 17-4 PH stainless steel, 300 W, 1400 mm/s experimental normalized area measurements compared with finite element results for an L_0/D_0 ratio of 10

Experiments from the Arcam S12 EB-PBF process in IN 718 at 670 W, 1300 mm/s, and expected L_0/D_0 of 20, were measured and normalized based on a W_0 value of 390 µm. Comparison between normalized experimental and finite element results for width, depth, and area are presented in Figure 3-17, Figure 3-18, and Figure 3-19. For normalized melt pool width experimental measurements agree with simulation results except at high normalized spot sizes. Experimental results fell below the simulation curve for an assumed tophat distribution, and above the curve for a Gaussian distribution. For normalized melt pool depth, experimental measurements fell slightly below the curves for tophat and Gaussian distributions. Slightly better agreement was found for the tophat distribution. Experimental measurements of normalized melt pool area matched simulation data from an assumed Gaussian distribution. Uneven agreement of experiments with tophat and Gaussian distributions suggests the beam profile in the Arcam process is neither tophat nor Gaussian, but a combination of the two.

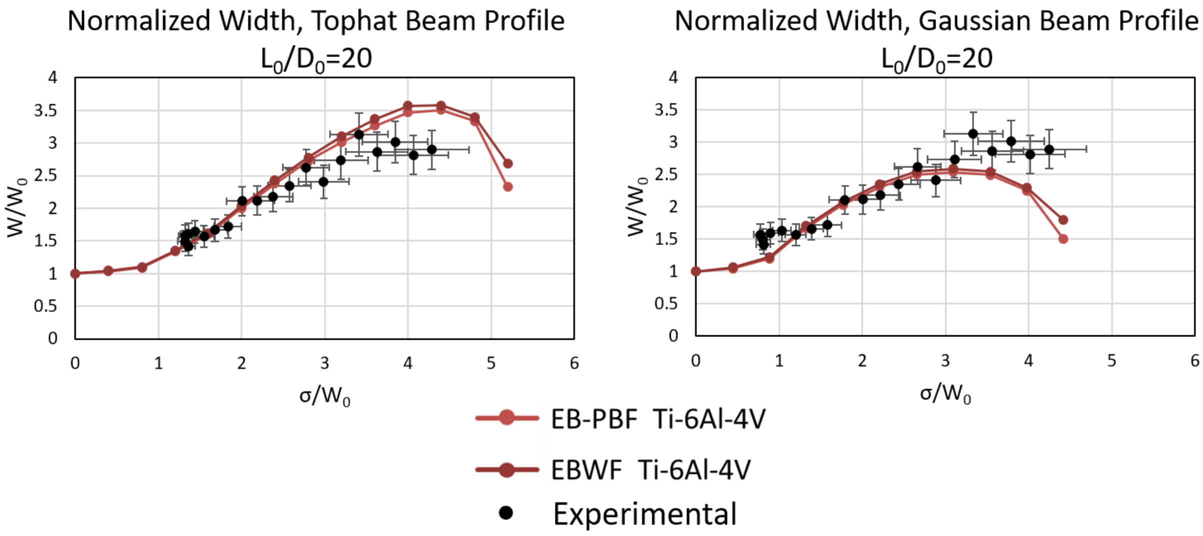

Figure 3-17: Arcam S12 EB-PBF, IN 718, 670 W, 1300 mm/s experimental normalized width measurements compared with finite element results for an L_0/D_0 ratio of 20

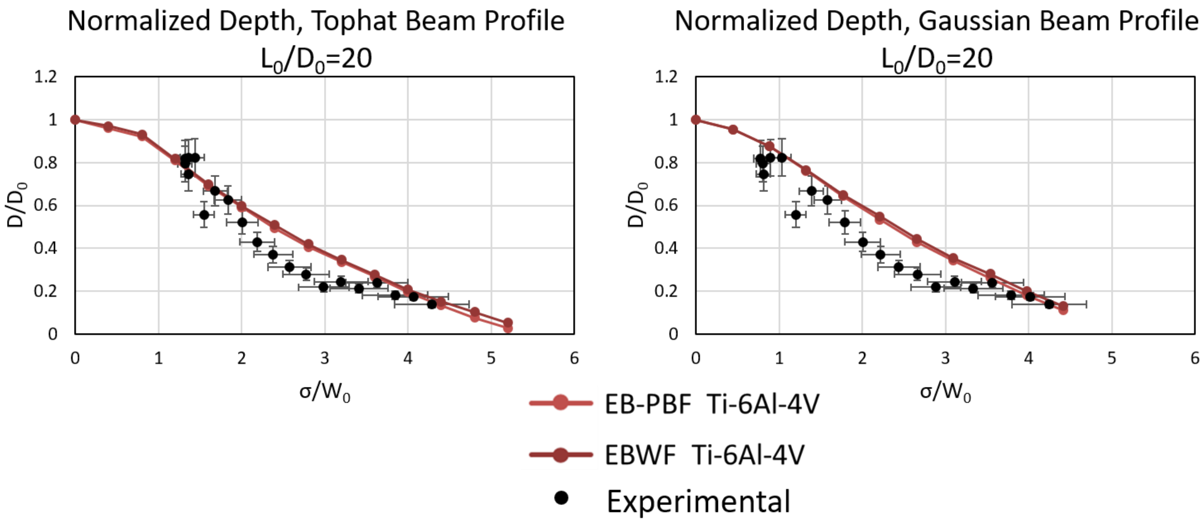

Figure 3-18: Arcam S12 EB-PBF, IN 718, 670 W, 1300 mm/s experimental normalized depth measurements compared with finite element results for an L_0/D_0 ratio of 20

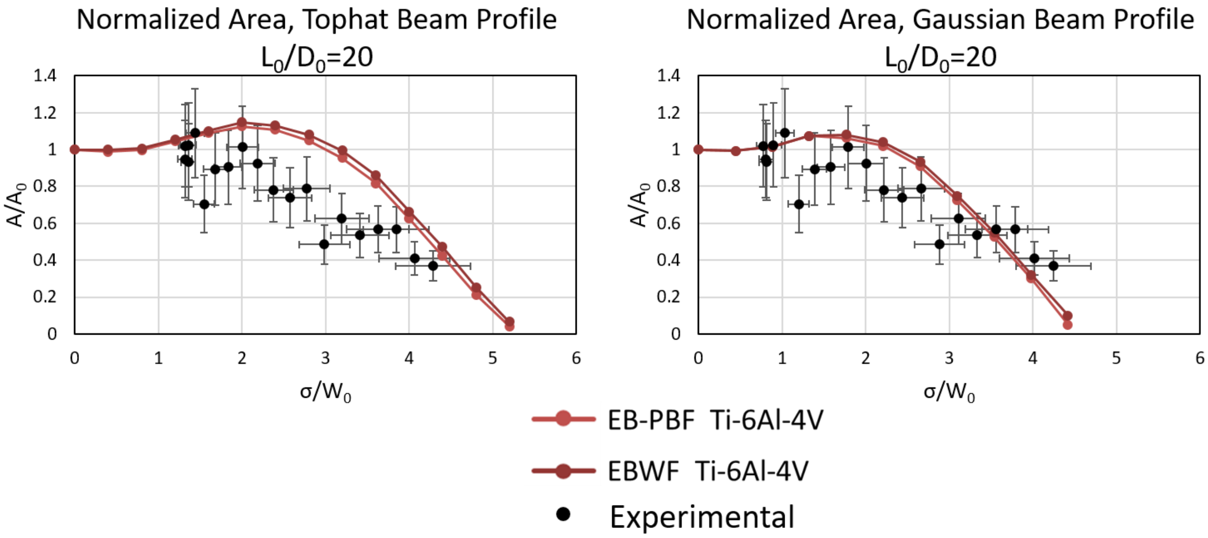

Figure 3-19: Arcam S12 EB-PBF, IN 718, 670 W, 1300 mm/s experimental normalized area measurements compared with finite element results for an L_0/D_0 ratio of 20

3.3.3 Spot Size Estimates

Measurements of spot size are key to knowing how certain melt pools will change when defocus parameters are adjusted. Backing out estimates of spot size from experiments can be very useful for machines where the spot size values are unknown. This section will present estimates from experiments for different machines and compare estimates with actual measurements of spot size in the EOS M 290 machine, and the ProX 200 machine. Estimated spot size values from multiple power-velocity combinations and alloys can be fit to curves describing lasers and electron beams that are off-focus.

The first step to estimate spot size based on experimental measurements is to identify a normalized spot size associated with the depth to width ratio of a melt pool as described in section 3.2.3. Normalized spot size values (σ/W_0) can be translated to estimated spot sizes by simply multiplying by the point source width (W_0). Point source width values were ascertained from simulations created by the author of this thesis and others [23] [116]. Characteristic curves can be fit to the spot size data to describe how the beam size changes with the defocus parameter. For lasers, Eq. 3-3 is used.

Eq. 3-3

$$\sigma(z) = \sigma_0 \sqrt{1 + \left(\frac{z - z_0}{z_r}\right)^2}$$

Where σ is the spot size at a defined offset, z. The minimum beam spot size, or waist, is represented by σ_0, the Rayleigh length by z_r, and z_0 represents the z location where the minimum spot size is present. Figure 3-20 shows the physical meaning of the variables discussed.

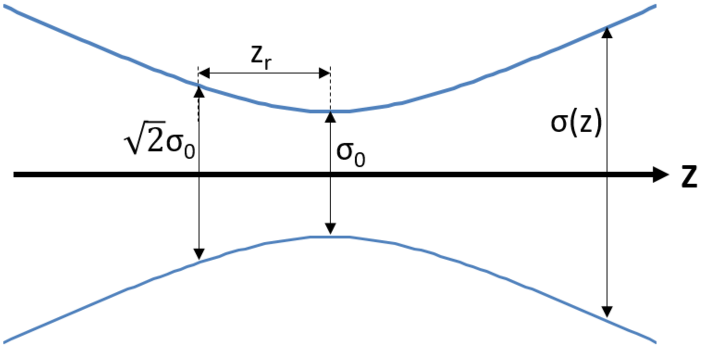

Figure 3-20: Beam profile with key beam measurements labeled

Estimated beam spot sizes for the ProX 300 L-PBF process are shown in Figure 3-21 along with best fit curves. Estimated spot sizes for an assumed tophat beam profile closely match estimated values for an assumed Gaussian beam profile. The best fit curve created for a tophat beam profile matched experimental results with an r^2 value of 0.936 with σ_0, z_r, and z_0 values of

121 µm, 4.03 mm, and -1.4 mm respectively. For an assumed Gaussian beam profile, the best fit curve matched experimental data with an r^2 value of 0.945, and fitted σ_0, z_r, and z_0 values of 101 µm, 3.25 mm, and -1.6 mm. Both best fit curves match the data very well and can likely be used to guide defocus adjustments for future experiments and builds. In general, an assumed Gaussian profile estimated smaller spot sizes at small offsets and larger spot sizes at large offsets when compared to the assumed tophat beam profile.

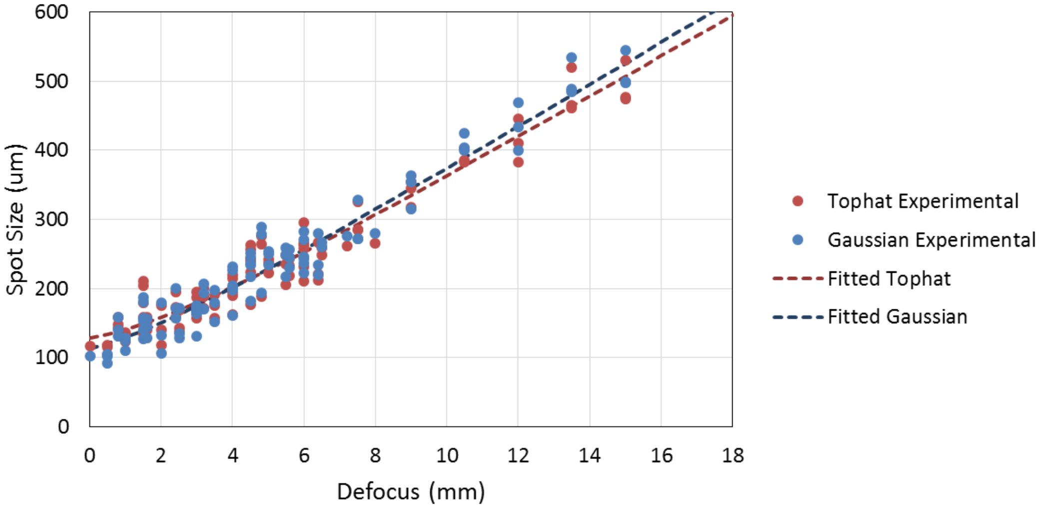

Figure 3-21: Spot Size Estimates for the ProX 300 L-PBF process with best fit curves for typical laser behavior

Estimated beam spot sizes for the ProX 200 L-PBF process are shown in Figure 3-22 along with best fit curves. The best fit curve created for a tophat beam profile matched experimental results with an r^2 value of 0.974 with σ_0, z_r, and z_0 values of 3 µm, 0.12 mm, and -1.62 mm respectively. For an assumed Gaussian beam profile, the best fit curve matched experimental data with an r^2 value of 0.977, and fitted σ_0, z_r, and z_0 values of 3 µm, 0.11 mm, and -1.12 mm. The values guiding the best fit curves suggest unrealistically low values for the waist (σ_0) of the beam;

however, these curves are likely still useful for guiding defocus changes in future experiments and builds.

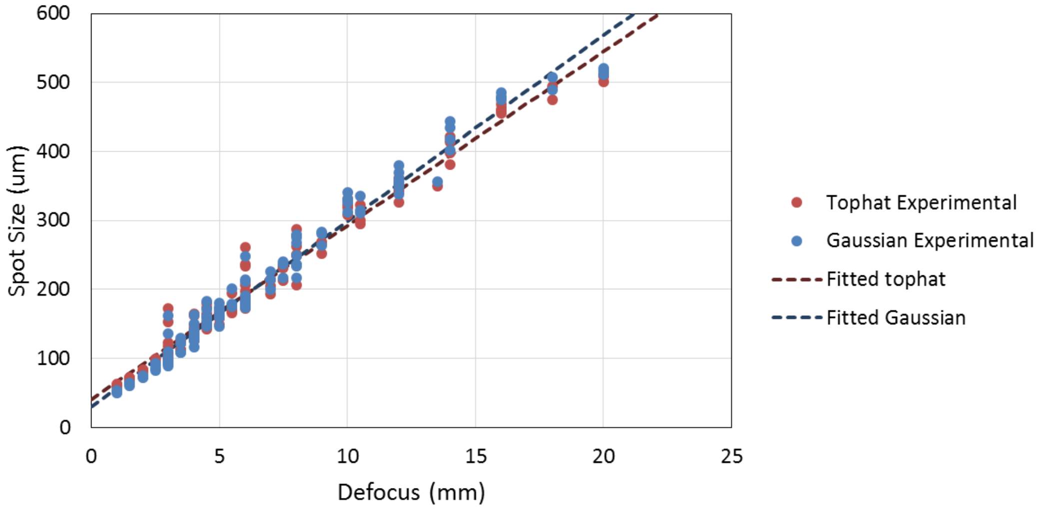

Figure 3-22: Spot Size Estimates for the ProX 200 L-PBF process with best fit curves for typical laser behavior

In the EOS M 290 process, spot size estimates and best fit curves are also compared against curves developed from actual measurements. A series of measurements were taken in the machine at Carnegie Mellon using Primes FocusMonitor equipment at 40 W and 200 W to find the Rayleigh length, beam radius, and z offset [114] [115]. Figure 3-23 shows experimental estimates and their best fit lines alongside a curve created from average values from the 200 and 40 W beam measurements. Very good agreement was observed between estimated experimental spot size values, and those based on measurements. Table 4 shows values from measurements, and curve fittings for the process. Additional information on the beam measurements is provided in Appendix 4.

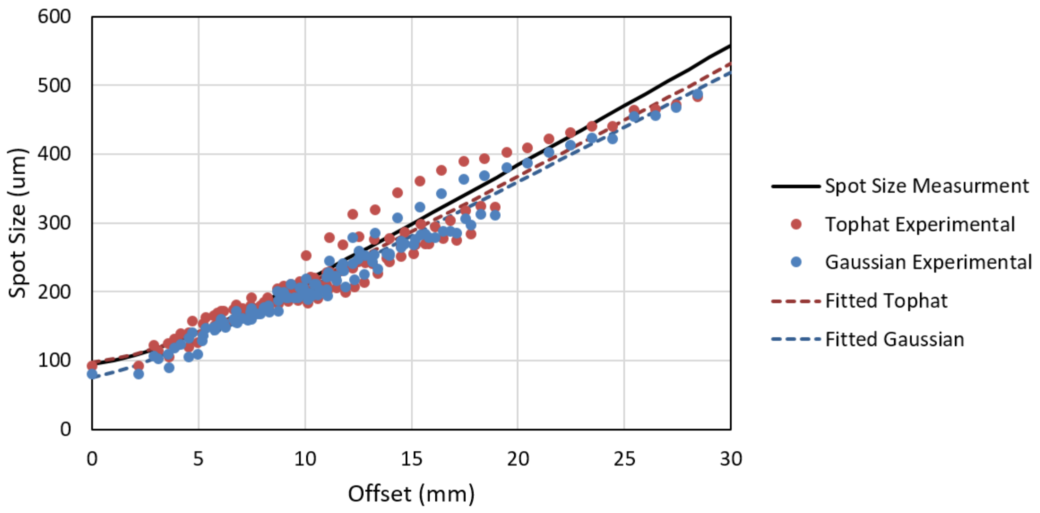

Figure 3-23: Spot Size Estimates for the EOS M 290 L-PBF process with best fit curves for typical laser behavior, and a curve based on spot size measurements

Table 4: Beam curve information from measurements and fitted curves for the EOS M 290 L-PBF process

	σ_0 (µm)	z_r (mm)	z_0 (mm)	Tophat profile r^2	Gaussian profile r^2
200 W Measurements	104.726	5.778	-1.48	0.842	0.822
40 W Measurements	83.216	4.794	-0.37	0.905	0.965
Fitted Tophat	96	5.71	-1.16	0.923	▨
Fitted Gaussian	69	4.25	-1.86	▨	0.969

Spot sizes in the Arcam S12 EB-PBF process were similarly estimated for different focus offset values. Figure 3-24 displays estimated values from experimental data along with best fit curves. The profile for electron beams also follows the same general profile in the z-direction as lasers. Current in the focusing coils is expected to change the spot size parabolically with changes to focus offset current [117] [118], however observations made to settings in the Arcam software appears to follow the trends produced by lasers. It is unknown whether the focus offset current that is set in the software is modified before changes are made in the process. The best fit curve created for a tophat beam profile matched experimental results with an r^2 value of 0.9674 with σ_0, z_r, and z_0 values of 513 µm, 11.3 mm, and 3.0 mm respectively. For an assumed Gaussian beam profile, the best fit curve matched experimental data with an r^2 value of 0.9535, and fitted σ_0, z_r, and z_0 values of 302.2 µm, 6.66 mm, and 2.1 mm. The minimum spot size in the process is expected to be around 300 µm [119], which is in good agreement with the assumed Gaussian profile. While the minimum spot size of the assumed Gaussian profile is in better agreement with the cited value, the tophat distribution appears to fit the data better. The beam profile likely falls between that of a tophat and Gaussian beam in this process.

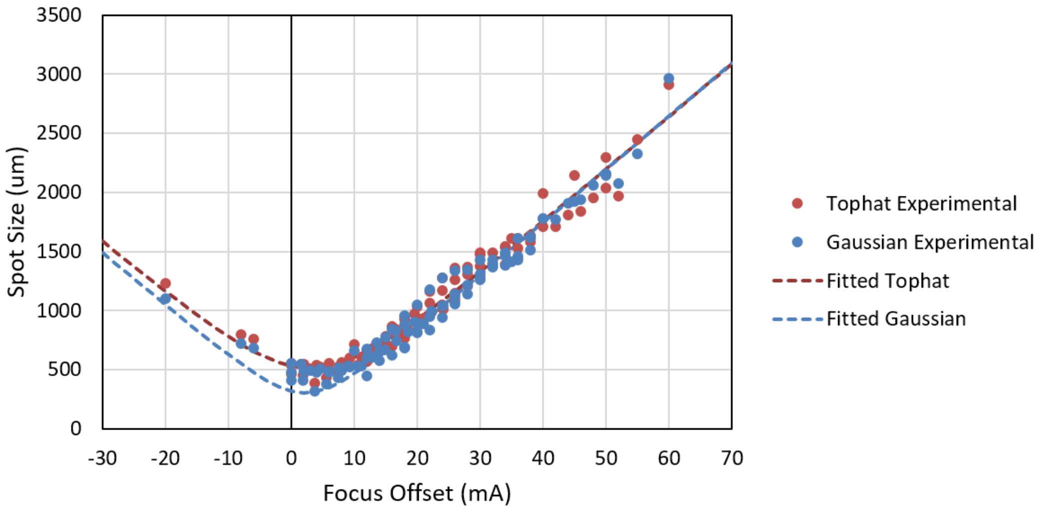

Figure 3-24: Spot Size Estimates for the Arcam S12 EB-PBF process with best fit curves

3.4 Discussion

The effects of laser and electron beam spot size across different melt pool sizes, alloys, and processes has been simulated and verified by experiments. Changing melt pool width, depth, and area were normalized by their point source values (W_0, D_0, and A_0) from simulations to remove variations in melt pool size. Spot size was also normalized by point source width. After normalization, changes in melt pool dimensions with spot size grouped together by the L_0/D_0 ratio, or aspect ratio.

Normalized melt pool width increased for all cases before dropping. Larger L_0/D_0 ratios had larger increases in width and withstood larger spot sizes before melting ceased. Normalized depth exhibited continuous decreases for any increases in spot size. For both normalized widths and depths, melt pool appear to follow similar changes before smaller L_0/D_0 melt pools dropped off from the trend. Normalized melt pool areas displayed distinctly different behavior between large and small L_0/D_0 ratios. Trends for small aspect ratios had small decreases in normalized area across low normalized spot sizes before larger decreases at higher spot sizes. Larger L_0/D_0 ratios had increases in normalized area at low and moderate spot sizes before dropping at higher normalized spot sizes. The behavior of normalized melt pool dimensions was also dependent on the assumed beam profile. Tophat and Gaussian beam profiles both followed similar trends with increasing spot sizes, but a Gaussian profile had smaller increases in width and area. Experimental results showed agreement with simulations across various L_0/D_0 ratios, alloys, and processes, but typically had better agreement with curves generated from a Gaussian beam profile.

Spot size values were also estimated based on experimental results and fit to characteristic curves. Depth to width ratios were measured for all spot size experiments and used to identify normalized spot sizes for each individual case. Normalized spot sizes are multiplied by simulation point source width to give an estimated spot size. Completed over a range of experimental points, estimated spot sizes give an idea of how spot size increases with offset parameters. In the EOS M 290 process, experimental estimates were compared with curves generated from beam measurements and saw very good agreement with an r^2 value of 0.965 for an assumed Gaussian beam profile. Estimated spot sizes can be used to guide offset changes for future experiments and builds.

Chapter 4: The Effects of Spot Size on Porosity and Flaws

4.1 Overview

In this chapter, the influence of spot size on melt pool morphological characteristics such as keyholing, variability, and porosity is analyzed. Variability in melt pool width and depth measurements is studied to find how keyhole mode melting influences single bead deposits. Keyholing is found to have little effect on the standard deviation of melt pool width, but a significant effect on standard deviation of melt pool depth. A depth to width ratio of 0.5 is used to identify keyholing and develop a normalized spot size threshold to avoid keyholing for multiple alloys. Insights into the effects of spot size on geometry and the presence of keyhole mode melting is used to design multi-layer pad experiments based on a large range of single bead melt pool areas. Porosity is measured in the multi-layer samples and compared to the nominal case.

4.2 Methods

4.2.1 Identifying Keyholing Melt Pools

Melting in additive manufacturing or welding processes occurs in one of two ways, conduction mode melting and keyhole mode melting. In conduction mode melting, the melt pool is created by heat conducting down from the surface to develop the melt pool. In keyhole mode melting, the beam raises the temperature high enough to vaporize significant amount of material. This can result in deep and narrow melt pools that are desirable in some welding applications, but is more variable and can leave behind porosity [45] [66]. In additive manufacturing, conduction mode melting is desired to avoid the porosity associated with keyhole mode melting and achieve more consistent results.

To identify melt pools that were deposited with keyhole mode melting, the depth to width ratio (D/W) is used. Melt pools with a depth to width ratio greater than 0.5 were deemed “keyholing” melt pools, as a semi-circular melt pool is the deepest that can be formed via only conduction mode melting [120]. While work by other authors has suggested identifying keyholing by using normalized enthalpy thresholds [47] [120], this research looks to identify thresholds based on relationships between the spot size and melt pool dimensions developed in Chapter 3:. Depth to width ratio trends can be compared for finite element simulations and experimental measurements to identify locations where experiments deviate from the predicted trends, and where the ratio exceeds 0.5. From this information, a normalized spot size can be suggested to avoid keyhole mode melting for different alloys.

4.2.2 Variability and Porosity Measurement

To identify the presence of any additional variability in keyhole or conduction mode melt pools, variability in melt pool width and depth is analyzed. Melt pool width can be easily traced after imaging melt pools from above. A script in MATLAB was developed by Fox to measure the distances between two regions manually painted red on an image [23]. Melt pool widths traced in red can be measured for both melt pool dimensions and standard deviation.

To acquire enough measurements for variability in melt pool depth, single bead melt pools need to be serial sectioned, or sectioned down the center of the bead. In this work, a series of melt pools were sectioned down the center of the bead with a wire EDM to measure depth variability using a similar MATLAB script as described above for width measurement. An additional component to the script included a best fit linear trend along the bottom of the melt pool to compensate for changing depths resulting from a misaligned cut. The traced melt pool was also cut off at the top surface of the melt pool to eliminate variability from the surface of the melt pool in a potential uneven cut. Melt pool depths were traced over a distance of 20 mm. Figure 4-1 shows a portion of a sectioned melt pool before and after being traced.

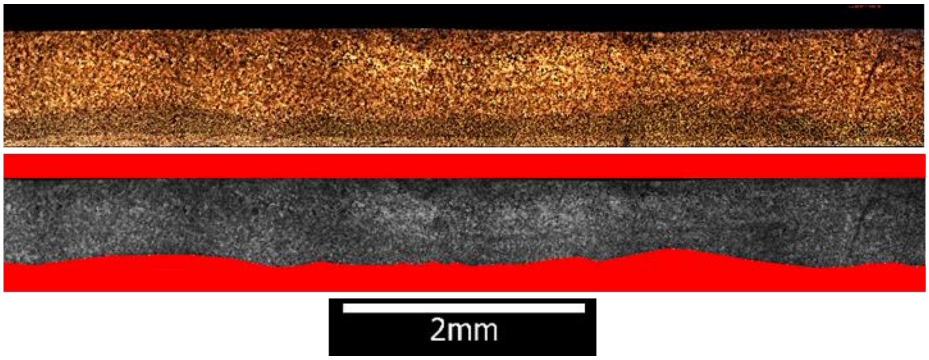

Figure 4-1: Melt pool depth before (top) and after (bottom) tracing for variability analysis

Analysis of bead-up melt pools could be completed by simply observing the surface of the single bead deposits. Bead up melt pools occur when instabilities in the melt pool begin breaking the liquid metal into individual droplets and is characterized by melt pools with inconsistent amounts of material in cross sections. Figure 4-2 shows two melt pools viewed from above and from cross sections. The top melt pool shows the inconsistent characteristics associated with bead-up melt pools while the bottom image shows a smooth melt pool with no bead-up issues present. Bead-up phenomenon can occur in long and narrow melt pools and can be a major source of porosity.

Previous work by Yadroitsev et al. identified a width to full length ratio (W/FL) as a threshold for bead-up melt pools in additive manufacturing [75]. To quantify the effects of spot size on the occurrence of the bead-up phenomenon, width to full length ratio was plotted against normalized spot size for different L_0/D_0 ratios. Observations from experimental melt pools can be used to verify the suggested cutoff values.

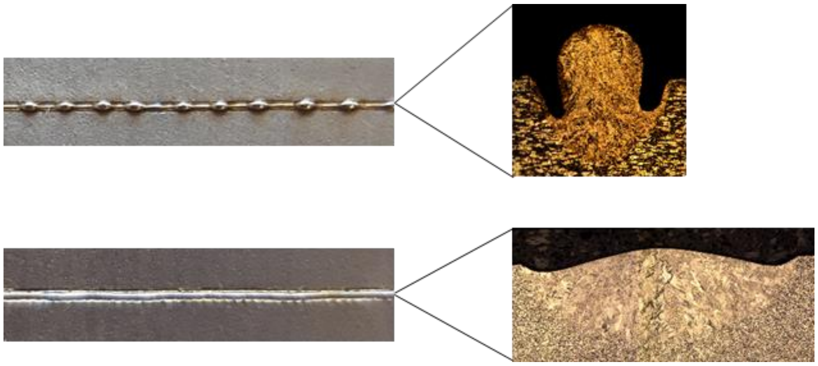

Figure 4-2: Bead-up (top) and smooth (bottom) melt pools as viewed from above, and from cross sections

Porosity measurements are completed on multi-layer pad experiments via optical images to analyze compare different parameter sets on how much porosity is present in the resulting deposit. Polished sections of a multi-layer deposit were imaged at three different magnifications, 2.5X, 10X, and 50X to be able to identify porosity of different size scales. Porosity measurements were gathered through the use of a MATLAB script developed by Luke Scime [121]. The code converts microscope images to a grayscale image, a brightness intensity histogram is displayed for the user to choose a cutoff intensity for identifying pores. The image is then converted to a binary black and white image based on the input cutoff value and porosity is calculated. Figure 4-3 shows the generated grayscale image with intensity histogram, and the resulting black and white image from a selected intensity cutoff value of 50.

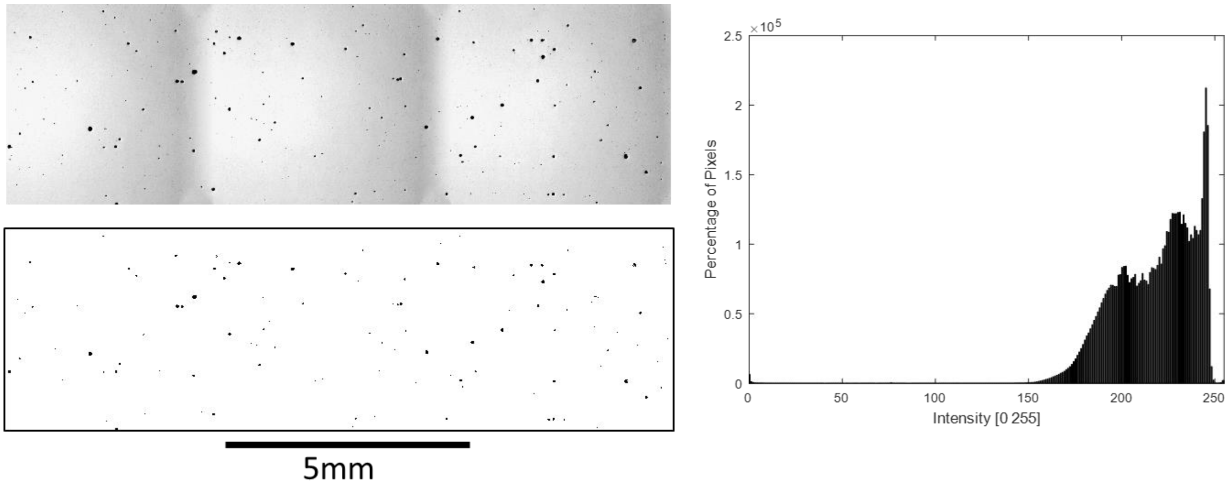

Figure 4-3: Porosity optical image before (top) and after (bottom) selection of an intensity cutoff value from the intensity histogram (right)

4.2.3 Experiment Setup

Experiments for this work consisted of both single bead experiments to analyze specific keyholing melt pools and variability, and multi-layer pads experiments to analyze porosity at different process parameter settings. This work made use of the same single bead experiments used in Chapter 3:, and some additional experiments designed to look more specifically at keyholing. Experiments involved particular power-velocity sets at chosen L_0/D_0 ratios where spot size was varied for different single bead deposits. These single bead deposits transitioned from keyhole mode melting at small spot sizes to conduction mode melting at larger spot sizes. Based on these experiments, relationships could be drawn between melt pool depth, width, spot size, and the occurrence of keyholing. Variability in melt pool depth was analyzed in a series of single beads at one power-velocity combination and multiple spot sizes. The chosen power-velocity combination was selected because of its relatively large size, making sectioning easier, and the occurrence of both significant keyhole and conduction mode melting across the spot size settings.

Multi-layer experiments were completed to analyze porosity in multi-layer pads build with a variety of process parameters. The experiments seek to identify porosity at different melt pool areas and compare nominal settings against settings with altered spot size and balanced hatch spacing and layer thickness. The multi-layer pads were deposited in the Arcam S12 EB-PBF process at a layer thickness of 70 µm in Ti-6Al-4V. Powder used for the build was gas atomized Ti-6Al-4V powder supplied by Arcam. The powder had been used in multiple previous builds and therefore may not have the same characteristics as virgin powder provided by Arcam. Table 5 outlines the settings used for each multi-layer pad deposited for these experiments. In general, the scan speed of the electron beam increases with increasing speed function [89], and increasing focus offset expands the beam. Settings to produce desired areas, and assistance with hatch spacing determination were provided by Sneha Narra [122].

Table 5: Multi-layer pad experiment plan to analyze porosity

Experiment #	Speed Function	Nominal Area Multiple	Focus Offset (mA)	Hatch Spacing (µm)
1	36	1X	19	200
2	72	0.5X	19	200
3	20	2X	19	1150
4	36	1X	10	362
5	72	0.5X	5	153
6	72	0.5X	0	220
7	152	0.25X	0	133
8	10	4X	28	1100
9	20	2X	25	290

Experiment one was deposited at the nominal settings for speed, focus offset, and hatch spacing in Ti-6Al-4V in the Arcam S12 machine at Carnegie Mellon. Experiments two and three used settings at larger and smaller cross-sectional areas with modified hatch spacing, but without modified focus offset. Experiment four used the nominal area setting with a decreased focus offset and increased hatch spacing intended to improve deposition rate while balancing melt pool width and hatch spacing to avoid introducing lack of fusion porosity. Experiments five and six were deposited at power and velocity settings designed to result in half the nominal area, and decreased focus offset and hatch spacing values to reduce porosity. Experiment seven used power and velocity settings to produce an area one quarter of the nominal size. Focus offset and hatch spacing were reduced to maintain low porosity. Experiment eight was designed for a melt pool four times larger than nominal with an increase in hatch spacing and focus offset to deposit successfully. Experiment nine used settings for an area twice that of nominal with increased focus offset and hatch spacing values to improve deposition quality.

4.3 Results

4.3.1 Depth and Width Variability in Keyhole Mode and Conduction Mode Melting

Many in the welding community have shown that keyhole mode welding can introduce increased variability in melt pool dimensions [45] [64] [65]. An investigation of additive manufacturing melt pools at different spot sizes was used to determine how variability in melt pool dimensions change at different magnitudes of keyholing. Figure 4-4 shows how melt pool depth and width change as a melt pool transitions into keyhole mode melting. Experiments were completed in the Arcam S12 EB-PBF process at a power of 670W, and velocity of 265 mm/s. Depth to width values over 0.5 are considered keyholing melt pools, and larger values indicate more severe keyholing. Melt pool widths showed less change as depth to width ratio increased into the keyhole mode melting range, but melt pool depths steadily increased. This suggests that increases in depth to width ratio in keyholing melt pools is primarily due to depth increases.

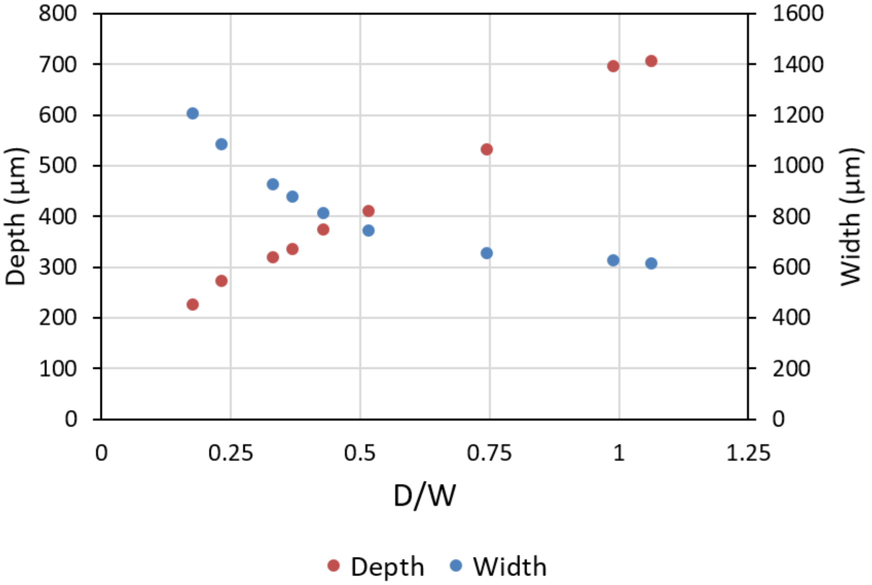

Figure 4-4: Width and depth vs D/W ratio for single beads deposited in Ti-6Al-4V in the Arcam S12 EB-PBF process

Similar to the plot above, standard deviations measured for the melt pools have been plotted against depth to width ratio for the 670 W, 265 mm/s EB-PBF experiments in Figure 4-5. Standard deviations for melt pool width taken from above view images suggest that the mechanisms that drive keyhole mode melting have little effect on the variability of the width of the melt pool. Standard deviations for width are consistently between 12 and 17 μm with no significant trend with respect to depth to width ratio. Standard deviations for melt pool depth were gathered from sections down the length of the melt pool. In conduction mode melting, standard deviations for depth typically fell below those found for melt pool width. In keyholing melt pools above depth to width ratios above 0.5, standard deviations increase significantly with increasing depth to width ratio. This signals that in more severe keyhole melt pools, the variability in the melt pool also become more severe, which reinforces the notion that keyhole mode melting is undesirable in additive manufacturing.

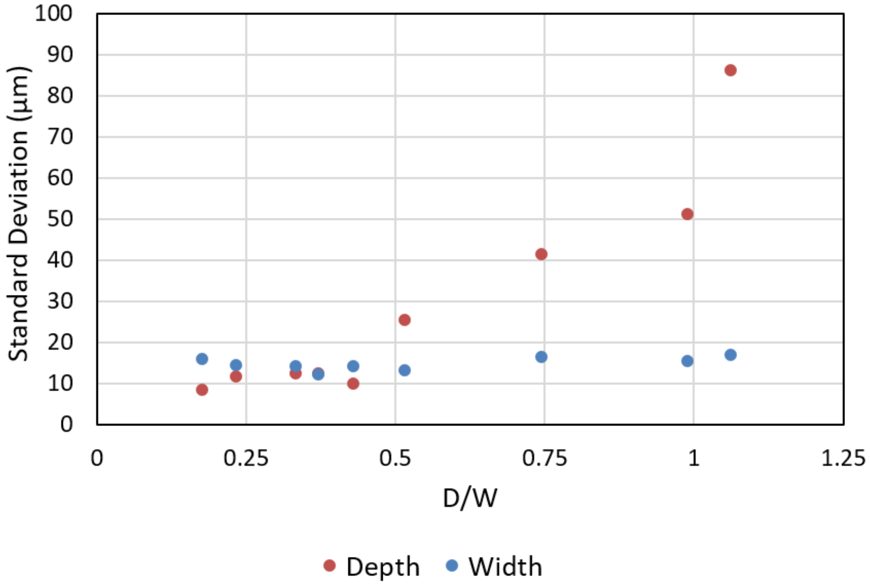

Figure 4-5: Standard deviations of width and depth vs D/W ratio for single beads deposited in Ti-6Al-4V in the Arcam S12 EB-PBF process

Although the data presented in this section is limited to data from one power-velocity combination, the observed trends give insight to how melt pool depth and width changes in conduction and keyhole mode melting scenarios. Keyholing has little effect on the width of melt pools, but can dramatically increase melt pool depth. While keyhole mode melting may be desirable in some welding applications, the variability in depth and large depth to width aspect ratios make keyhole mode melting unwanted when compared to more consistent melt pools deposited in conduction mode melting.

4.3.2 Spot Size Changes to Prevent Keyholing

Key to depositing successfully throughout processing space while avoiding keyhole mode melting is the ability to eliminate the occurrence of keyholing through process variable modification. Figure 4-6 displays Ti-6Al-4V melt pools produced in the Arcam S12 EB-PBF process at Carnegie Mellon at 670 W, 265 m/s, and different focus offset values. At narrow beam sizes, keyholing melt pools are produced. As spot sizes are increased, keyholing becomes less severe, and melt pools are created via conduction mode melting. Knowledge of the melt pool and spot size can be used to avoid keyhole mode melting and the adverse effects that come with it.

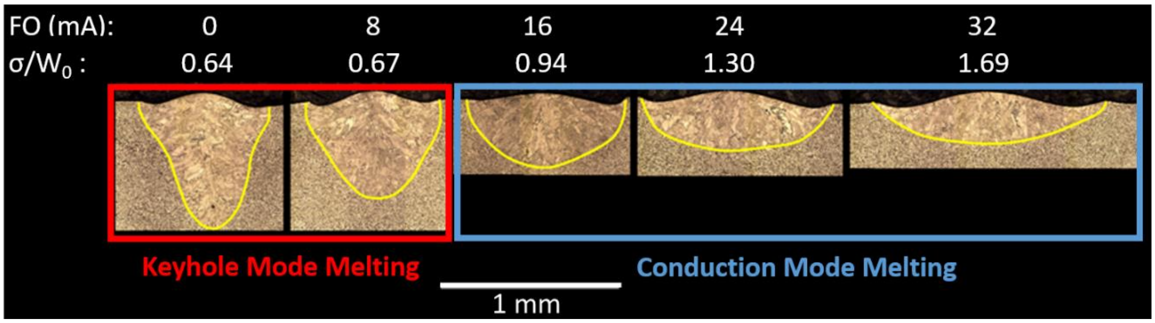

Figure 4-6: Melt pool cross sections from increasing spot sizes transitioning from keyholing to non-keyholing melt pools

To get an understanding of how spot size can be used to avoid the keyholing phenomenon, depth to width ratio is plotted against normalized spot size. Figure 4-7 shows depth to width values for all Ti-6Al-4V experiments from the Arcam S12 EB-PBF and EOS M 290 L-PBF processes along with the FEA line for an assumed Gaussian profile at a L_0/D_0 ratio of 5. To avoid keyholing by the D/W threshold of 0.5 used in this work, a corresponding normalized spot size (σ/W_0) value of 1 is necessary to ensure keyhole mode melting is avoided in Ti-6Al-4V. This means that spot sizes must be kept above the estimate point source width of a melt pool to avoid keyholing. There is also a second threshold of interest that may signal reduced variability in melt pools. At a depth to width ratio near 0.3, all experimental measurements begin good agreement not only with the finite element curve for depth to width, but also with other experiments. This depth to width threshold corresponds to a normalized spot size of 1.25. These two thresholds suggest that maintaining normalized spot sizes above 1 can help avoid keyhole mode melting, and normalized spot sizes above 1.25 produce more predictable melt pool sizes in Ti-6Al-4V.

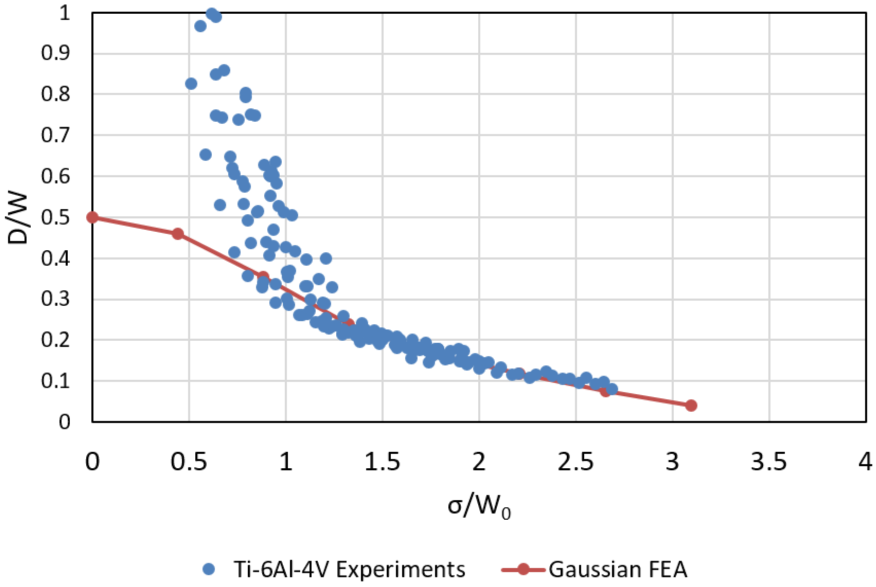

Figure 4-7: D/W ratio vs normalized spot size for all experimental Ti-6Al-4V data

A Similar analysis can be completed to find normalized spot size thresholds to avoid keyholing in other alloys. Figure 4-8 displays experimental data for both Inconel 718, and 316L stainless steel along with finite element data. IN718 experiments were completed only in the Arcam S12 EB-PBF process, while 316L stainless steel experiments were completed in the 3D Systems ProX 200 and ProX 300 L-PBF processes. The number of experiments completed in IN718 is much more limited than those for Ti-6Al-4V presented earlier, but a similar threshold value for keyholing can be found. A threshold for keyholing is found at a normalized spot size value of 0.9, just below the value found for Ti-6Al-4V. The keyholing threshold for normalized spot size in 316L stainless steel was similarly found to be 0.9. Both IN718, and 316L stainless steel thresholds were based off fewer experiments when compared to Ti-6Al-4V, and therefore a threshold for reduced variability in melt pool results could not be determined.

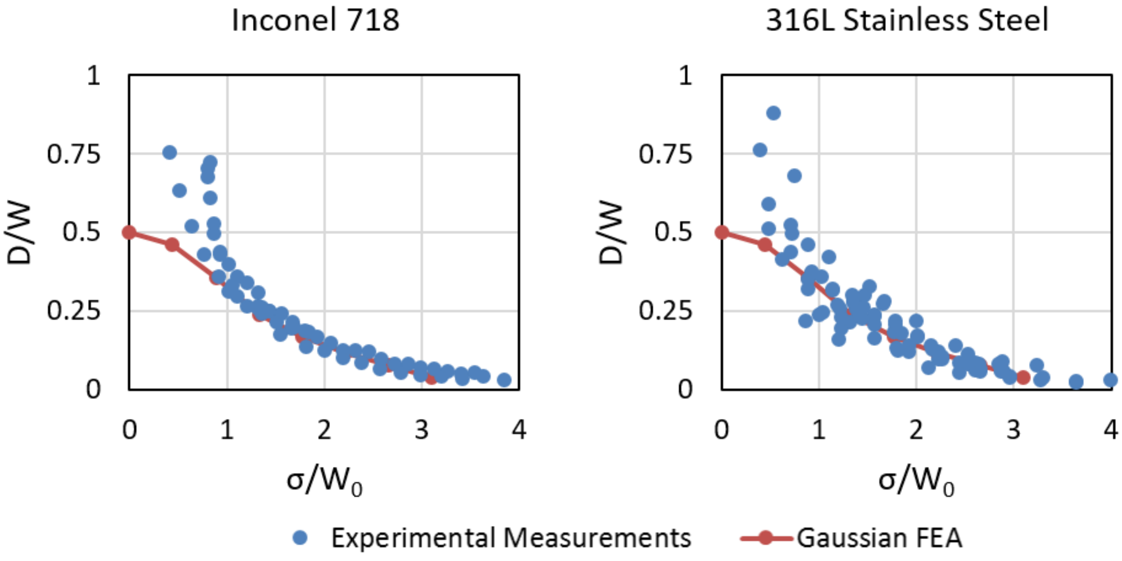

Figure 4-8: D/W ratio vs normalized spot size for all experimental IN718 (left) and 316L stainless steel (right) data

Keyholing thresholds can also be found for 17-4 PH stainless steel, and 304 stainless steel based on experiments from the ProX 200 and ProX 300 L-PBF experiments. Figure 4-9 shows experimental D/W data for 17-4 PH and 304 stainless steel compared against a finite element curve (L_0/D_0=5). For 17-4 PH stainless steel, a threshold for keyholing based on experimental measurements is determined to be 0.9, which falls in line with values attained for IN718 and 316L stainless steel. A normalized spot size threshold to avoid keyholing for 304 stainless steel based on experimental data is determined to be 0.9. As with IN718 and 316L stainless steel, there is not enough experimental data to determine a second threshold for reduced variability.

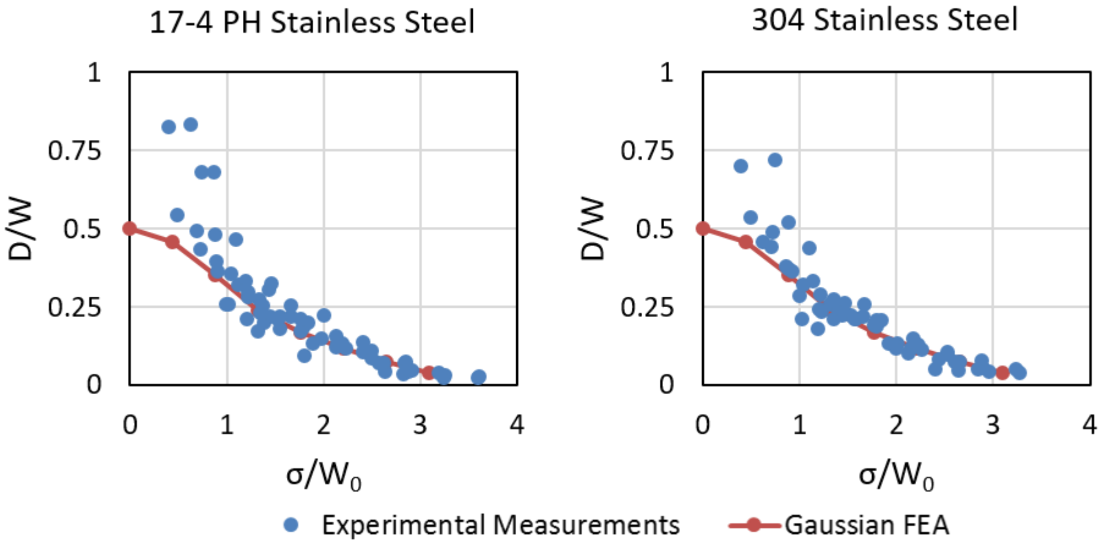

Figure 4-9: D/W ratio vs normalized spot size for all experimental 17-4 PH (left) and 304 (right) data

Plotting depth to width ratio for all experiments against normalized spot size has enabled thresholds to be developed based on spot size and melt pool size to be able to avoid keyhole mode melting. Across five different alloys, thresholds to avoid keyholing were found to be very similar. A conservative threshold to avoid keyholing across all five alloys studied in this section is a normalized spot size of 1. This means that to avoid keyholing, the spot size must be kept above the point source width from simulations, or estimated from experiments. A second threshold was observed in Ti-6Al-4V experiments for reduced variability, but such a threshold could not be determined in other alloys.

4.3.3 Spot Size Changes to Reduce Bead-up

In addition to keyhole mode melting, bead-up melt pools can introduce porosity into additive manufacturing deposits due to the inconsistent surface of the melt pools. Yadroitsev et al. suggested a minimum width to full length ratios to avoid instability depending on the angle the melt pool creates with the substrate. At an angle of 180 degrees, where the melt pool is contacting the substrate at one point, the W/FL threshold is found to be 0.26, and for a free cylinder with no contact to a substrate, the threshold is 0.32. These two numbers will be used as indicators for potential instability and the onset of bead-up.

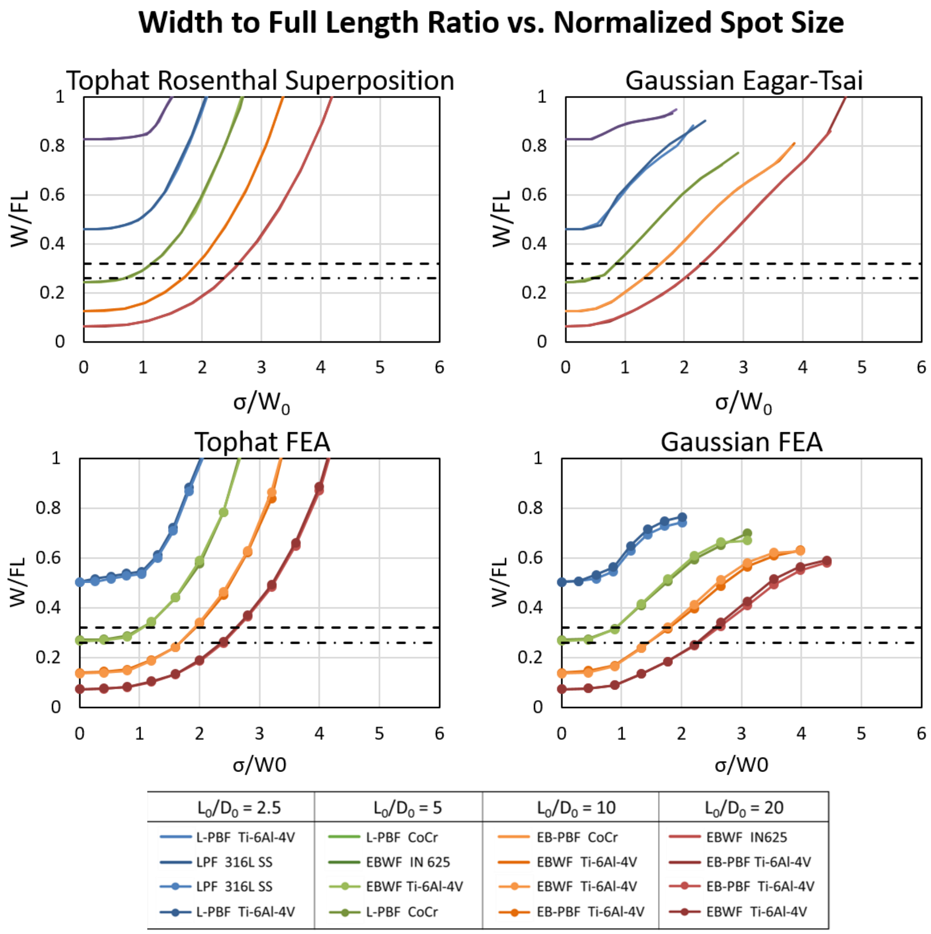

Figure 4-10: Width to full length (W/FL) versus normalized spot size (σ/W_0) for melt pools of different aspect ratios

Figure 4-10 shows trends in width to full length ratio with increasing spot size for different L_0/D_0 ratios. Shorter melt pools at smaller L0/D0 melt pools do not enter the bead-up region regardless of the spot size, however L0/D0 values above five require increased spot size to increase the width to full length ratio and avoid bead-up melt pools. For an assumed tophat beam distribution, W/FL continually increases at an increasing slope. With a Gaussian beam distribution, W/FL ratio continually increases with normalized spot size, but the changes become less significant at larger spot sizes. More important than the behavior of the width to full length ratio is the value of the normalized spot size where L_0/D_0 lines cross the bead-up thresholds. For this, similar values can be obtained for both tophat and Gaussian beam distributions.

Melt pools from a series of spot size experiments deposited in the 3D Systems ProX 200 L-PBF process in 17-4 stainless steel are presented in Figure 4-11. Width to full length values can be found based on normalized spot size, L_0/D_0 values, and the presented Gaussian simulation data. As spot size is increased, width to full length ratio increases, and severity of bead-up decreases. For the case presented below, a bead-up threshold exists between a W/FL ratio of 0.26 and 0.32. The average of the two values (0.29) is used as a threshold for this case with a W/FL uncertainty of 0.03.

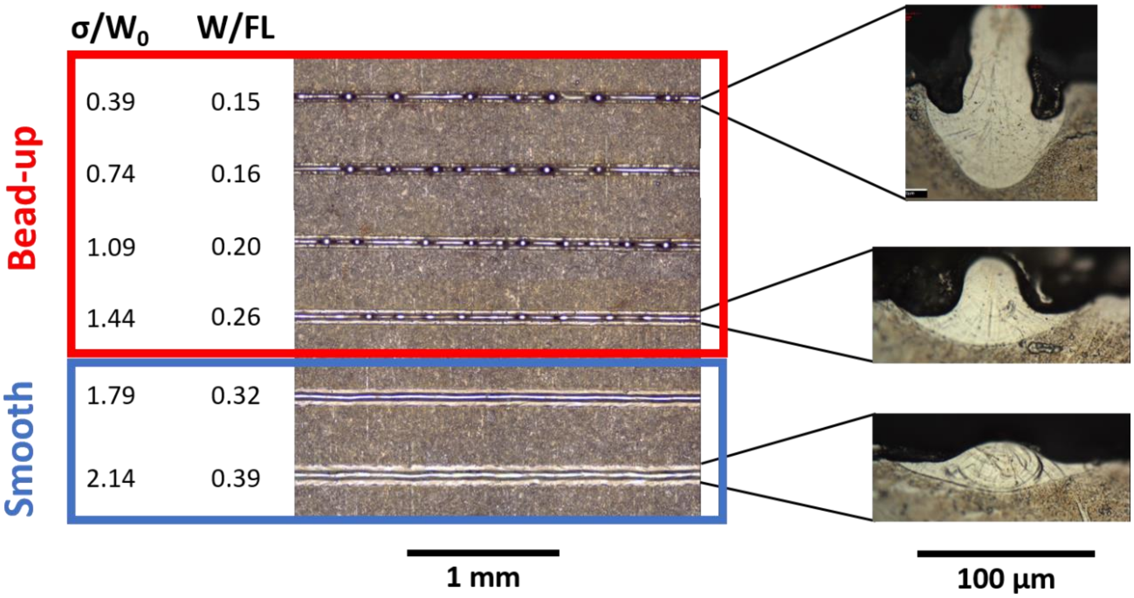

Figure 4-11: Observed bead-up and smooth melt pools deposited in 17-4 PH stainless steel in the ProX 200 L-PBF process

Observations similar to those presented above were completed in melt pool tracks across different alloys and processes to verify thresholds proposed by Yadroitsev when spot size is increased. Melt pools can be plotted in W/FL versus σ/W_0 space for the associated L_0/D_0 values to determine the bead-up threshold for different power-velocity combinations. Table 6 shows W/FL thresholds observed from various spot size experiments. The threshold presented is the average W/FL value between the last bead-up melt pool, and the first smooth melt pool. Uncertainty in the measurement is simply the difference between those average values and the W/FL value of the last bead-up melt pool.

Table 6: Experimental bead-up identification and measurement

Process	Alloy	Power (W)	Velocity (mm/s)	W/FL threshold	W/FL Uncertainty
Arcam S12	Ti-6Al-4V	670	1100	0.3	0.01
Arcam S12	Ti-6Al-4V	670	550	0.275	0.005
EOS M 290	Ti-6Al-4V	370	1900	0.265	0.005
EOS M 290	Ti-6Al-4V	330	2150	0.28	0.01
ProX 200	SS 316L	300	2400	0.29	0.03
ProX 200	SS 17-4 PH	300	2400	0.29	0.03
ProX 200	SS 304	300	2400	0.29	0.03

Strong agreement is observed between proposed bead-up thresholds and those observed for no-added material Ti-6Al-4V and stainless steel single bead deposits. Although good agreement is observed between Ti-6Al-4V and stainless steel deposits, bead-up was not observed in Inconel 718 deposits where it was expected due to a low width to full length ratio. With a layer of added powder, bead-up may occur in the Inconel deposits, but further work is required to explain the discrepancy between alloys. A conservative W/FL threshold to avoid bead-up melt pools is suggested as 0.32 based on the largest cutoff observed with uncertainty.

4.3.4 Spot Size Changes to Reduce Porosity

Based on previous information gathered about the effects of spot size on geometry and onset of keyholing, multi-layer pads were built in the Arcam S12 EB-PBF process. The power and velocity settings were based on different desired melt pool areas. Spot size was adjusted to give preferable melt pool shape, and hatch spacing was adjusted to ensure complete melting. Figure 4-12 displays percent porosity measured in each sample at different magnifications, and displays some key experiment settings.

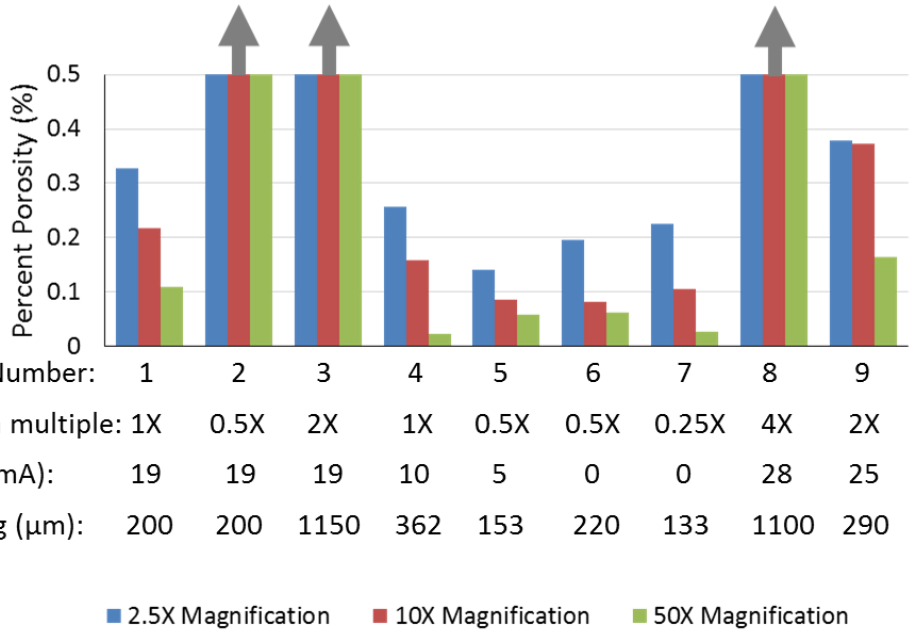

Experiment Number:	1	2	3	4	5	6	7	8	9
Nominal area multiple:	1X	0.5X	2X	1X	0.5X	0.5X	0.25X	4X	2X
Focus offset(mA):	19	19	19	10	5	0	0	28	25
Hatch spacing (μm):	200	200	1150	362	153	220	133	1100	290

Figure 4-12: Percent porosity measured at different magnifications for Ti-6Al-4V multi-layer pads deposited in the Arcam S12 machine at Carnegie Mellon

Experiments two, three, and eighth all had significant porosity of 15, 28, and 14 percent respectively. These would not be acceptable for use with the process parameters used, but may be suitable with adjustments to spot size or hatch spacing. Experiment nine, at a melt pool area of 2X resulted in similar porosity as the nominal settings in experiment one. Porosity in these experiments could likely be reduced by changing process parameters, as porosity at the nominal power-velocity settings was decreased in experiment four by decreasing spot size and increasing hatch spacing. A larger hatch spacing was able to be used because the smaller spot size gave better penetration into the substrate than the nominal focus settings. This simple decrease in spot size enabled a deposition rate 81 percent higher than standard settings at the same power and velocity.

The two lowest porosity samples in experiments five and six were produced at the 0.5X power-velocity settings. During the design of these experiments, the complete profile of spot size versus focus offset was unknown, and thus the two experiments were deposited at very similar spot sizes. A narrow spot size compared to nominal settings gave the 0.5X melt pools additional penetration into the substrate, and a smaller hatch spacing in experiment five resulted in reduced porosity. Experiment seven, with 0.25X power and velocity, also had significantly reduced porosity when compared to the nominal condition with decreased spot size and hatch spacing.

With correct adjustments to spot size, hatch spacing and layer thickness can be adjusted to create successful deposits. Adjustments made in experiments in this section allowed for successful deposition with melt pools that were one quarter to double the area of the nominal case. This wide range of available melt pool sizes can allow an operator to take advantage of qualities deposited at different melt pool sizes or in different regions of processing space.

4.4 Discussion

Keyhole mode melting can be avoided in additive manufacturing melt pools by increasing spot size. Variability in single bead melt pools was analyzed for both melt pool widths and depths. Depth to width ratio was used as an indicator of the presence and severity of keyhole mode melting, and both depth and width were plotted against this ratio. A depth to width ratio greater that 0.5

was considered a keyholing melt pool. As a depth to width ratio increased, changes in width became less sensitive to increasing severity of keyhole mode melting. Melt pool depth, however, steadily changed with increasing D/W ratio signaling that depth is primarily responsible for increases in melt pool area in keyhole mode melting. Standard deviations were calculated in melt pool widths as measured from above, and melt pool depths from sections down the length of the melt pool. Standard deviations in melt pool width were unaffected by keyhole mode melting and increasing severity of the phenomenon. Standard deviations in melt pool depth saw a jump in melt pool with D/W ratios greater than 0.5 and increasing variability with increasing keyhole severity.

Methods to identify keyholing based on depth to width ratio were explored and used to determine a normalized spot size (σ/W_0) threshold to avoid keyhole mode melting in Ti-6Al-4V, IN718, 316L stainless steel, 17-4 PH stainless steel, and 304 stainless steel. Normalized spot size thresholds for the different alloys were found to be 1.0 for Ti-6Al-4V, and 0.9 for all other alloys analyzed. Since all values were very close, a conservative estimate for all alloys analyzed is to follow the value of 1.0 to avoid keyhole mode melting in the alloys presented. While the alloys in this study all gave very similar results, analogous studies would need to be performed to confirm thresholds for different alloys.

In addition to keyholing, spot size can be used to avoid the formation of bead-up melt pools. Melt pool width to full length (W/FL) ratio has been established as an important indicator for the development of bead-up melt pools by previous authors [74]. Trends for W/FL against normalized spot size are developed based on simulations, and experiments are used to verify thresholds to avoid bead-up suggested by Yadroitsev [75]. Good agreement is observed between experimental and proposed thresholds suggesting spot size can be used to methodically avoid bead-up melt pools in additive manufacturing. A conservative threshold is considered to be a W/FL ratio of 0.32, but the value may need to be modified when a powder layer is present.

Knowledge of keyholing thresholds and geometrical changes due to spot size changes was used to design multi-layer pad experiments for a range of melt pool sizes. By modifying focus offset and hatch spacing, porosity at nominal power-velocity settings was able to be decreased while increasing deposition rate by 81 percent. Lower porosities were also achieved for process parameters at areas 0.5, and 0.25 times the nominal case. Similar porosity values were found for parameters yielding an area twice that of the nominal case. By including spot size in process parameter adjustments, high quality depositions can be created by avoiding keyhole and lack of fusion porosity.

Chapter 5: The Effects of Spot Size on Ti-6Al-4V Deposition Microstructure

5.1 Overview

The microstructure in an additively manufactured part is a key factor determining the part's mechanical properties. Models used in previous chapters are used to gain insights into how spot size affects cooling rates, which play an important role in the development of microstructure. Differences between tophat and Gaussian beam profiles are explored, and differences in results between the two cases are explained. Prior beta grain measurements from various Ti-6Al-4V experiments show no correlation with changing spot sizes. The absence of a trend with spot size requires an amendment to the findings by Gockel [81] that suggest a direct relationship between spot size and effective melt pool width.

5.2 Methods

5.2.1 Modeling

Work in this chapter makes use of the finite element, Rosenthal, and Eagar-Tsai models used in Chapter 3:. Much of this section reiterates the details of those models; information on the methods used that are specific to this chapter begins in section 5.2.1.3.

Work in this chapter is a product of both finite element based and analytical based models. Finite element simulations used in spot size analysis are based on those used in Chapter 2:, and simulate top hat or Gaussian flux distributions. Analytically based models are evolutions of the Rosenthal model of a moving point heat source [91]. The Eagar-Tsai model simulates a moving heat source with a Gaussian heat source and is a modification of the Rosenthal model [93]. Another model was created to simulate a top hat heat source by using the principle of superposition with the original Rosenthal model. These models were used to identify how melt pool geometry changes with increasing spot size.

5.2.1.1 Finite Element Models

The finite element model used in this section was a slight modification on the model used for the laser powder feed process. The model simulates a distributed moving heat source on a large substrate that is long enough to reach steady state melt pool size and wide and deep enough to avoid edge effects and a symmetry boundary condition down the center of the melt pool. The heat flux is distributed across elements on the surface to make a semi-circular shape. The number of elements with applied heat flux is determined by stepping through elements in the X-direction and rounding to the nearest element in the Y-direction to create the correct shape. Two different flux distributions within the spot size were simulated. One model uses a tophat distribution where all flux values are set equal, and a second approximates a Gaussian distribution. The spot size value used from Gaussian distribution simulations follows the D86 width measurement technique commonly used to find laser beam diameter [113]. The distribution of the heat flux for a typical model is shown in Figure 3-1.

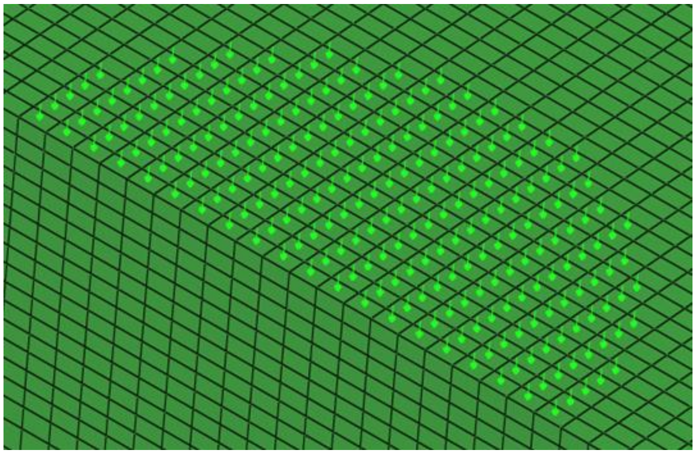

Figure 5-1: Flux distribution on the surface of a finite element model

The Gaussian heat source model extended the Gaussian profile out to two standard deviations, and amplitude is adjusted to provide the full power input. Since the Gaussian profile is fit onto a set of square elements, the smallest spot sizes used (4 element radius) had the largest percent error between the discrete and true distribution (25%). Other spot sizes simulated were multiples of 4 elements through the radius and have significantly decreased error in respect to modelling a Gaussian beam profile. Simulations of spot size span multiple processes and alloys. In all cases, the finite element models use temperature dependent thermal properties.

5.2.1.2 Rosenthal and Eagar-Tsai Models

In addition to finite element models, simpler models for tophat and Gaussian beam distributions were used to identify effects of increasing spot size. The models do not include temperature dependent properties or latent heat, but a solution can be found in a matter of seconds compared to hours or days. The first model, simulating a tophat distribution, is based off the moving heat source model developed by Rosenthal [91] shown in Eq. 3-1.

Eq. 5-1

$$T - T_0 = \frac{q}{2\pi kR} e^{-\frac{v(w+R)}{2\alpha}}$$

Where T is the temperature of the location of interest, T_0 is the preheat temperature, q is the input power, v is the travel velocity, k and α are thermal properties, and w and R specify the location. The equation gives the temperature at a specified location relative to a point heat source. To create a tophat heat source, multiple Rosenthal models are organized into a circular shape with 100 instances across the diameter. The principle of superposition is used to sum the solutions for a specified point in space. Melt pool boundaries are found by using the Newton-Raphson method and maximum width, depth, and area is found using the golden-section search method.

The Eagar-Tsai model was developed based on the Rosenthal model and simulates a moving heat source with a Gaussian distribution. Where the original Rosenthal model can be solved analytically, the derived Eagar-Tsai model in Eq. 3-2 must be solved numerically [93].

Eq. 5-2

$$\theta = \frac{n}{\sqrt{2\pi}} \int_0^{\frac{v^2 t}{2\alpha}} \frac{\tau^{-\frac{1}{2}}}{\tau + u^2} e^{-\frac{\xi^2+\psi^2+2\xi\tau+\tau^2}{2\tau+2u^2}-\frac{\zeta^2}{2\tau}} d\tau$$

Dimensionless temperature is represented by θ, and ξ, ψ, and ζ represent dimensionless distance in x, y, and z. Dimensionless time is represented by τ. u is a dimensionless heat source distribution parameter and n is an operating parameter that includes power, velocity, and thermal properties. The integral was solved numerically with the trapezoid method, and melt pool boundaries and maximum geometry values were found via the Newton-Raphson and golden-section search methods as with the tophat distribution model.

5.2.1.3 Modeling Cooling Rate

Simulation results for cooling rates have been determined from the different types of models described above using two different methods. In finite element simulations, a MATLAB script developed by Brian Fisher [123] measures the distance between the liquidus and solidus temperatures to generate a thermal gradient at the tail of the melt pool. The gradient is then multiplied by the heat source travel velocity to give a cooling rate for the steady state melt pools. In the Rosenthal based models used in this section, the absence of latent heat makes calculation of cooling rate easier. The gradient at the tail of the melt pool is multiplied by velocity to give the cooling rate for the simulation. Important to this work are the trends in cooling rates, thus the specific values are inconsequential.

5.2.2 Experiments and Microstructure Analysis

Experimental data used in this section was gathered from those used for geometry analysis in Chapter 3:. The Ti-6Al-4V single bead experiments are deposited at select power-velocity combinations in the Arcam S12 EB-PBF, EOS M 290 L-PBF, and Sciaky electron beam wire feed processes.

Once experiments were completed, samples are prepared for analysis. Samples are cross-sectioned, polished, and etched using Kroll’s etchant. Procedures for polishing and etching can be found in Appendix 1. Samples are then imaged using an Alicona Infinite Focus optical microscope. Melt pool cross-sectional dimensions and average prior beta grain width can be measured. Prior beta grain size is measured using the intercept method [112]. Prior beta grains in these processes are columnar in nature so prior beta grain width is the dimension of focus in this study. A horizontal line is drawn perpendicular to the growth direction of columnar grains, and grains are counted then the total is divided by the length of the line.

Work in this chapter will use normalized spot size values identified in Chapter 3:, but will focus on the microstructure of the depositions as opposed to the melt pool geometry. Melt pool geometries were previously normalized by their point source simulation values. Similarly, grain width is to be normalized; however, a point source grain size cannot be gleaned from simulations. Grain widths are therefore normalized by values found at small, non-keyholing melt pools, and may be based on two to three melt pools to reduce the influence of a single melt pool.

5.3 Results

5.3.1 Model Results

Models of a moving heat source were used to identify trends in cooling rates and give insight as to how prior beta grain widths may change with increasing spot size. Figure 5-2 displays trends for normalized cooling rates (CR/CR_0) in melt pools of different L_0/D_0 values. Similar to melt pool dimensions in earlier chapters, cooling rate is normalized by the point source value of cooling rate (CR_0). Trends are presented for both tophat and Gaussian beam profiles, as well as Rosenthal-based and finite element models. With a tophat beam distribution, cooling rates remain fairly constant with increasing spot size before sharply increasing at high normalized spot sizes. Melt pools with higher L0/D0 ratios have smoother increases in normalized cooling rate. This is in contrast to the behavior of normalized cooling rates for a Gaussian beam profile.

With a Gaussian beam profile normalized cooling rates increase similar to with a tophat distribution before leveling out and decreasing at large spot sizes. Larger potential increases in cooling rate are observed in melt pools with larger L_0/D_0 values. There is also a discrepancy between the trends observed in the Eagar-Tsai model, and the Gaussian distribution finite element model. Normalized cooling rates from the Gaussian finite element model only display slight leveling in some chosen curves, and has higher peaks than those observed by the Eagar-Tsai model. The differences between the two model results can be attributed to approximations made in generating the Gaussian heat flux distribution in the finite element models. The interface between elements with surface flux, and elements without surface flux, at the edge of the simulated beam lead to artificially higher gradients at the tail of the melt pool at large spot sizes. With a beam profile simulated to further extents, the differences between the two models would be reduced.

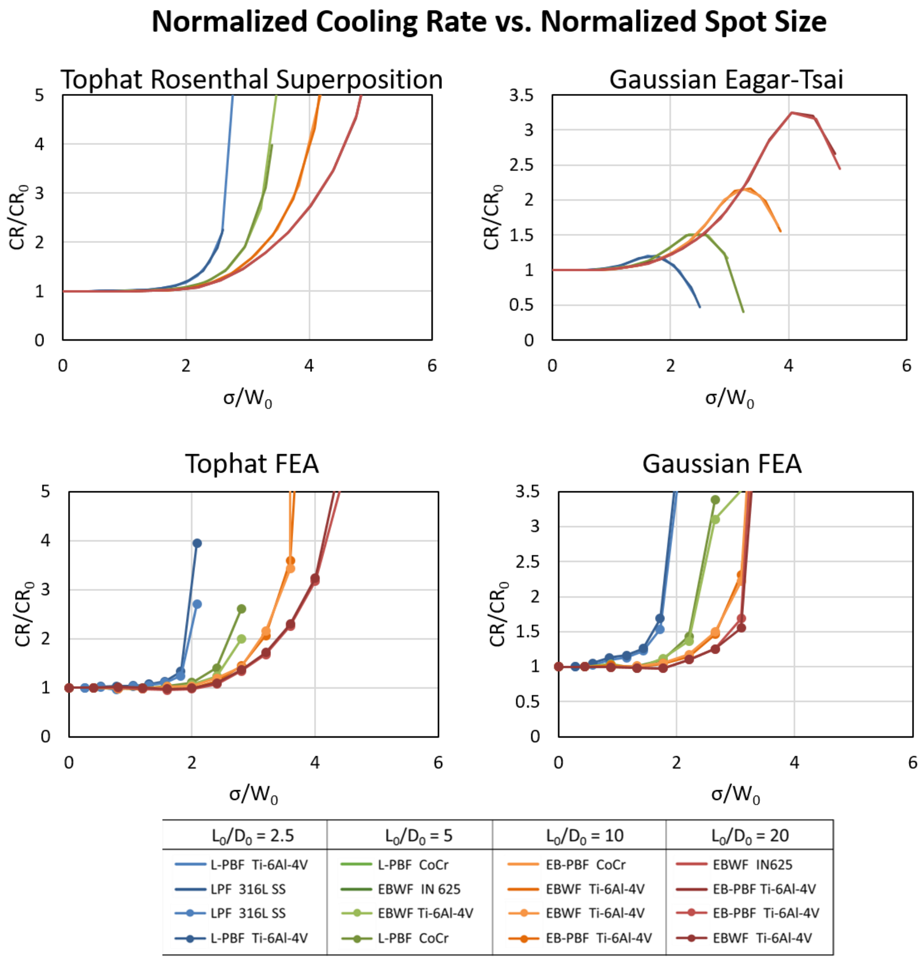

Figure 5-2: Normalized cooling rate vs. normalized spot size for tophat and Gaussian beam distributions

Differences between the two trends in cooling rate between tophat and Gaussian beam profiles is attributed to the temperature profiles created in the melt pools. Figure 5-3 compares the beam and temperature distributions down the centerline of the melt pool generated from the Rosenthal superposition tophat profile and Eagar-Tsai Gaussian profile models over various normalized spot sizes. The curves were created for a simulation of IN625 in the electron beam wire feed process at 3 kW and 21 mm/s with a L_0/D_0 ratio of 5. With a tophat beam profile, the maximum temperature occurs at the back edge of the beam before dropping sharply as the material cools. As the beam is expanded, the peak temperature develops closer to the melting temperature. This in turn brings the steep drop in temperature at the back of the beam spot closer to the melting temperature, raising the gradients at the melting point and similarly the cooling rates.

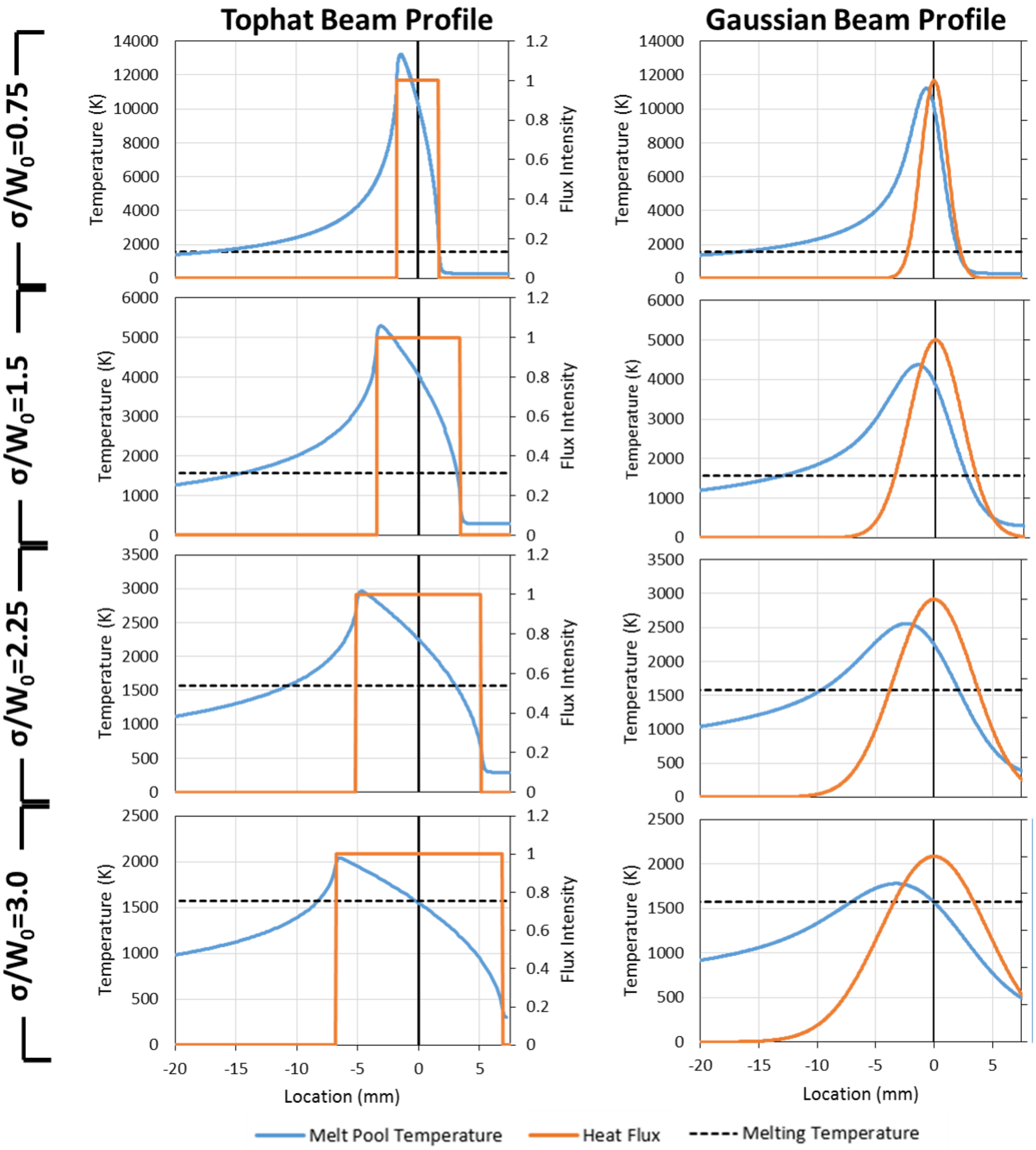

Figure 5-3: Temperature and beam profile distributions for different normalized spot sizes

With a Gaussian beam profile, the peak temperature also occurs toward the back of the beam spot; however, energy is still being input into the melt pool behind the peak temperature. This offsets some of the heat being conducted away and gives a smoother temperature profile compared to the tophat distribution. As spot size is increased, the melting point occurs at a location with steeper gradients on the melt pool cooling curve. As the spot size continues to increase, the melt point approaches the rounded peak of the temperature curve and begins decreasing.

5.3.2 Single Bead Experiments

Data from single bead experiments was gathered from experiments in the Arcam S12 EB-PBF, EOS M 290 L-PBF, and Sciaky electron beam wire feed processes. Prior beta grains from each experiment set were measured to get average grain sizes in the melt pools at different spot sizes. Measurements were normalized based on prior beta grain widths in relatively small, non-keyholing melt pools and plotted against normalized spot size. Figure 5-4 shows normalized grain width (GW/GW_0) versus normalized spot size data from all experimental measurements. The data does not form a discernable trend suggesting spot size has little to no effect on prior beta grain width in Ti-6Al-4V.

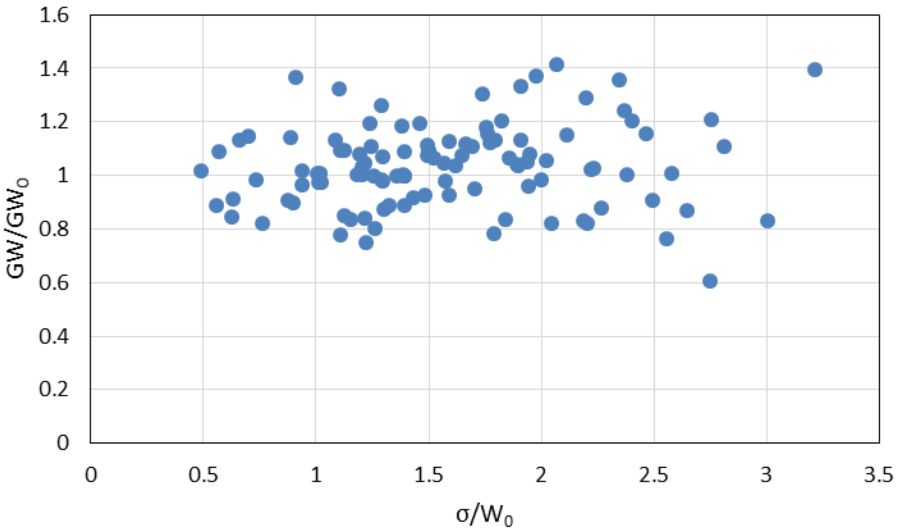

Figure 5-4: Experimental normalized prior beta grain width vs. normalized spot size for Ti-6Al-4V

The lack of correlation between prior beta grain width and spot size also means that there cannot be a relationship solely between grain size and melt pool dimensions, as the spot size does not change the melt pool dimensions. This suggests a corollary needs to be added to the findings by Gockel [81] that prior beta grain width scales with the square root of melt pool area. At large spot sizes, wide and shallow melt pools can have significantly reduced melt pool areas. An adjusted relationship between melt pool area and prior beta grain width should read as follows: Prior beta grain width in Ti-6Al-4V scales with the square root of area for consistent cross sectional shape. By considering the relationship for a consistent cross sectional shape, differences in area due to spot size no longer has influence over the trend. An additional benefit of using the relationship with consistent melt pool shape is the ability to directly use the measured melt pool width, rather than calculate effective melt pool width based on cross-sectional area measurements.

In light of the information presented in this chapter, relationships between melt pool dimensions and prior beta grain width in the Sciaky electron beam wire feed process from section 2.3.3 can be modified. Figure 5-5 shows the relationship between average prior beta grain width and effective melt pool width for both the original effective width values based on area measurements and adjusted effective width values that account for the effects of spot size on melt pool area. Adjusted values were ascertained through the fitted finite element process map for cross-sectional area associated with the process. The two groups of data still give very similar results, but a steeper slope is observed in the adjusted values. Larger differences would be expected between the two trends if more extreme melt pool shapes were present in the experiments.

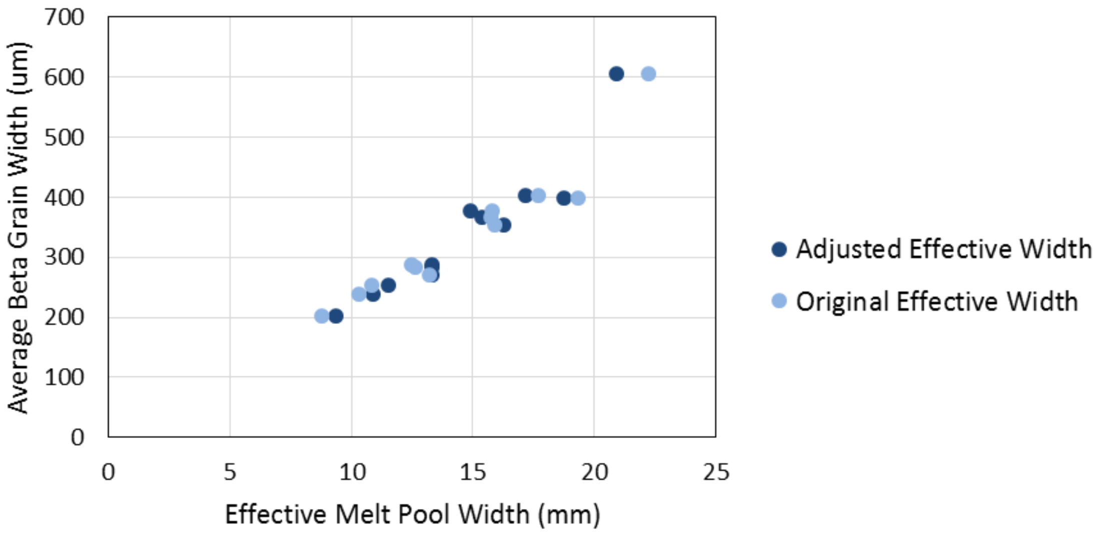

Figure 5-5: Relationships between prior beta grain width and effective melt pool width based on the original effective widths based on measurements, and spot size adjusted values based on finite element simulations.

5.4 Discussion

In addition to melt pool dimensions in previous chapters, the effects of spot size on cooling rate has been simulated. Trends between normalized cooling rates and normalized spot size show that cooling rate is generally not correlated with spot size for small and moderate spot sizes, while there is a strong, positive, correlation at large spot sizes. Simulations also identified significant differences in cooling rate at large spot sizes between beam distribution assumptions. Sharp decreases in applied heat at the edge of a tophat beam result in increasingly steep gradients and increasing cooling rates while the smoother shape of a Gaussian beam results in smaller increases in cooling rates, and even decreases in cooling rate for small L_0/D_0 ratios.

Based on the results of cooling rate trends from simulations, grain size is expected to decrease with increasing tail cooling rate at large spot sizes. Contrary to expectations, Ti-6Al-4V single bead experiments from multiple processes at various normalized spot sizes had no dependence upon spot size. This observation requires that the notion that grain width scales with melt pool area only holds true if the shape of the melt pool remains constant. It is important to note that these experimental measurements are for single bead results only, and the observed trends may not hold for multi-layer deposits. More work is required in the future to confirm or qualify the experimental findings in this chapter.

Chapter 6: Adjusting Spot Size to Expand Processing Space

6.1 Overview

Previous chapters have shown various ways that spot size influences different aspects of additive manufacturing deposits. Work presented here presents how those findings can be implemented to expand the usable processing space in additive manufacturing processes. Three stainless steels are process mapped in the ProX 200 L-PBF process at the nominal spot size. Issues are noted with the melt pools created throughout processing space, and expanded spot size experiments are completed for 316L stainless steel. Expanded spot size experiments make use of findings in Chapter 4: to eliminate keyholing at target power-velocity combinations. New melt pool measurements are used to create a modified process map with an increased usable processing space. A method is proposed to systematically increase the "good" processing space by avoiding keyholing, and preventing the occurrence of bead-up melt pools in some regions.

6.2 Methods

6.2.1 Modeling

Finite element process maps in this section are based on a series of two dimensional simulations completed using the Abaqus software package. The model is made up of a single plane and a point heat source that travels node by node along the y-axis. The model is radially symmetric about the y-axis, thus the model is simulating a heat source moving axially down the center of a cylinder. Simulating a simple heat source traversing a flat substrate of material is the goal of the model, so energy input on each step is doubled to compensate for energy lost to half of the modeled cylinder. As with finite element models used in previous sections, the two-dimensional model has a section of fine mesh where the melt pool will develop and be measured before a biased mesh creates a large enough substrate to simulate a semi-infinite domain. The model is long enough to allow melt pools to reach a steady state. Temperature dependent thermophysical properties are used for 316L, 17-4, and 304 stainless steel used in this chapter [124] [125] [126].

Melt pool dimensions measured from the simulations includes melt pool width, depth, cross-sectional area, and length values. The two dimensional models require less computing time when compared to the three dimensional models due to simplifications in the model geometry. A drawback of the model is the inability to model heat source distributions that are not a point heat source. The two dimensional model is therefore used as a basic model to create process maps, or to quickly ascertain point source and L_0/D_0 values that can be used for spot size adjustments.

6.2.2 Experiment Design and Process Mapping

Experiments took place in the 3D Systems ProX 200 L-PBF process for process mapping and spot size analysis purposes. For process mapping experiments, points for single bead experiments were chosen throughout the capable power and velocity in a grid pattern. Selected powers and velocities consisted of 45, 130, 215, and 300 watts for power, and 400, 900, 1400, 1900, 2400, 2900, and 3400 mm/s for velocity. All points were deposited at the nominal focus offset setting of zero, which results in a maximally focused beam with an estimated spot size of 30 μm from section 3.3.3. To generate a process map with lines of constant melt pool area, values measured from melt pools are piecewise linearly interpolated to find locations of a prescribed area in power-velocity space.

The experimental process map can then be related to finite element results through an effective absorptivity. Effective absorptivity is found by dividing the power required to produce a certain melt pool area in finite element simulations by the power required in experiments to produce the same area. Melt pool dimensions are measured after sectioning, polishing, and etching experimental deposits. Measurements of melt pool area were taken in such a way that a surplus or dearth of material was ignored, in the same fashion as outlined in section 3.2.2. Polishing and etching procedures for the stainless steel alloys are provided in Appendix 1.

Included in this chapter are experiments designed to eliminate keyholing at power-velocity combinations previously used for process mapping experiments. Seven points in processing space that had been classified as keyholing melt pools from 316L stainless steel process mapping experiments were selected to develop a new process map that is not influenced by the increased melt pool areas produced by keyholing. At each power-velocity combination, findings in Chapter 4: were used to guide selection of new focus offset values. A new process map could then be created using the newly deposited single beads at larger spot sizes.

6.3 Results

6.3.1 Process Mapping

Process maps of cross-sectional area were developed for 316L, 17-4, and 304 stainless steels in the 3D Systems ProX 200 process. In addition, specific experimental points were identified as keyholing, undermelting, bead-up, or good melt pools. Keyholing melt pools were identified as melt pools with a depth to width ratio greater than 0.5, and undermelting melt pools were identified as melt pools width a depth less than the nominal layer thickness that would lead to lack-of-fusion porosity. Bead-up melt pools were labeled as such based on above view observations of the single bead deposits. “Good” melt pools were the remaining melt pools that had not been labeled as having geometrical problems. Figure 6-1 shows the labeled points, and area process map for 316L stainless steel. Keyholing melt pools dominated the high power, low velocity region of processing space at the nominal focus settings, and undermelting dominated the low power, high velocity region. Bead-up melt pools occurred in the high power, high velocity region of processing space and coincided with many keyholing and undermelting melt pools. A very small region is left to be categorized as “good” points, which severely limits the range of settings that can be used to produce successful parts.

The influence of keyholing and undermelting can also be seen in the process map. While experimental measurements match up very well with finite element results, it only does so when different effective absorptivities are used for each line of constant area. Melt pools at smaller areas were effected by comparatively larger normalized spot sizes that worked to reduce the melt pool area in experiments, and resulted in lower effective absorptivities. Conversely, larger melt pools with small normalized spot sizes had increased melt pool areas due to the keyholing phenomenon, and therefore larger effective absorptivities. The significant differences in effective absorptivity, and small “good” processing space are remedied in section 6.3.3.

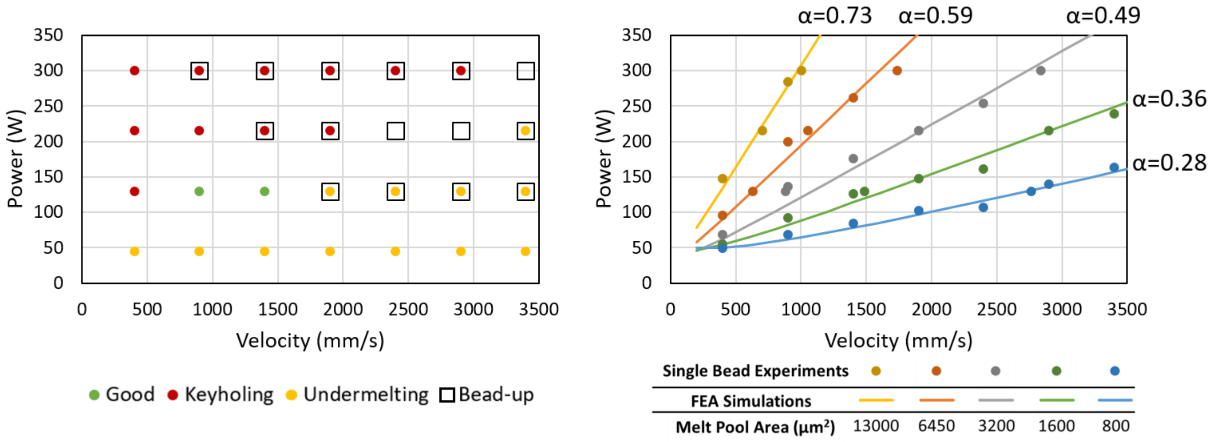

Figure 6-1: 316L experiments labeled good, keyholing, undermelting, and bead-up melt pools identified in melt pools throughout processing space (left), and finite element and experimental process map of melt pool areas with effective absorptivity values (right).

Process mapping and regions of keyholing and undermelting melt pools are also explored for the 17-4 PH stainless steel alloy. Figure 6-2 displays categorized melt pools in power-velocity processing space along with a melt pool area process map for the alloy. Unlike 316L stainless steel, experiments throughout power-velocity processing space are dominated by keyholing and undermelting melt pools. It is important to note, however, that there were no melt pools that required both a keyholing and undermelting label. This suggests that there would be a small region of "good" melt pools along the interface of the two regions. The process map displays similar behavior as the 316L process map, where small melt pools in the undermelting region had significantly smaller effective absorptivities than those in the keyholing region. Even with differences in effective absorptivities, the process map can be used to find different geometries throughout the capable process space.

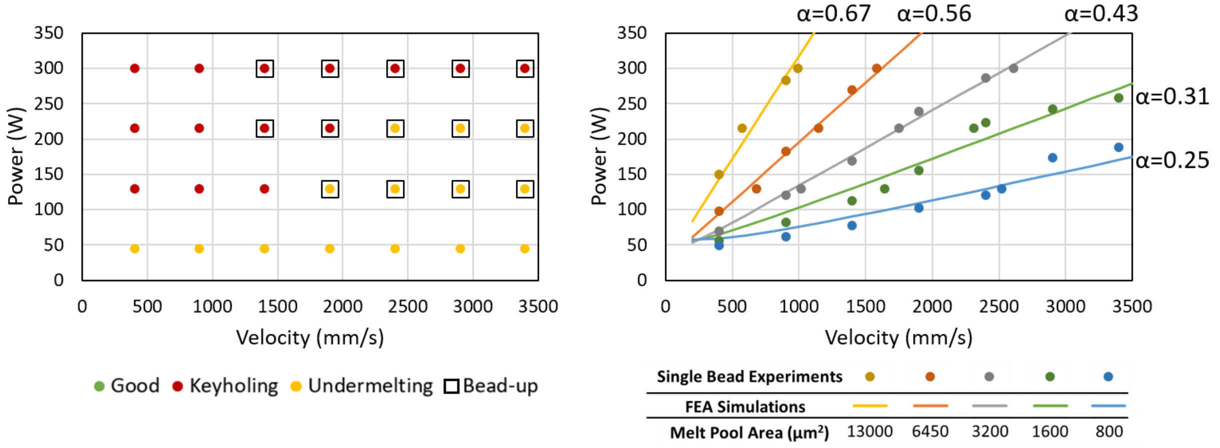

Figure 6-2: 17-4 experiments labeled good, keyholing, undermelting, and bead-up melt pools identified in melt pools throughout processing space (left), and finite element and experimental process map of melt pool areas with effective absorptivity values (right).

Process mapping and melt pool labeling was also completed for the 304 stainless steel alloy in Figure 6-3. As with the previous two alloys, keyholing melt pools dominate the high power, low velocity region of power-velocity space, and undermelting dominates the low power, high velocity region. One “good” point signals a small region of ideal processing space between the three larger regions of keyholing, undermelting, and bead-up. The melt pool area process map also resembles those from the other two stainless steel alloys. Small melt pools with shallow depth to width ratios have decreased absorptivities while large melt pools exhibit keyholing, which further increases the melt pool area.

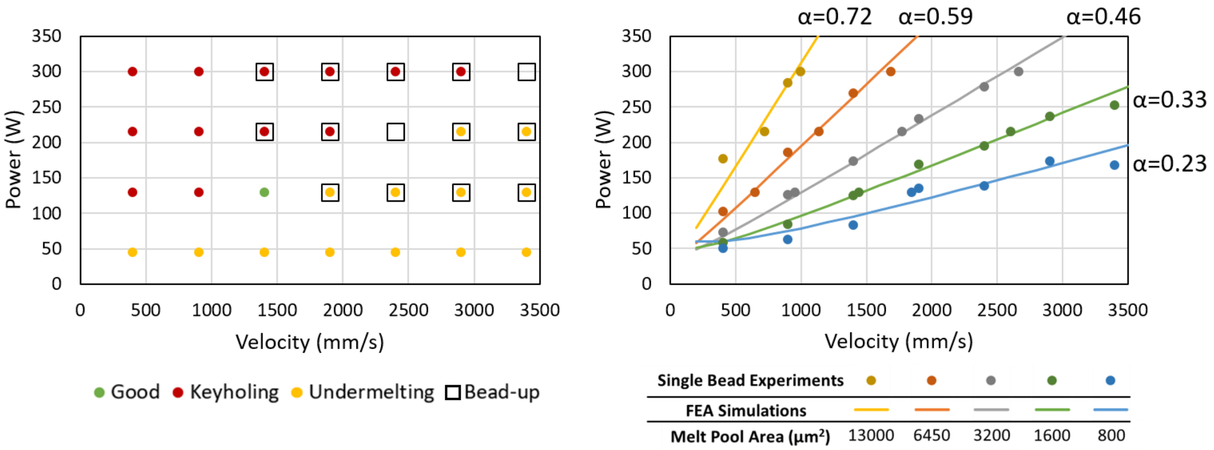

Figure 6-3: 304 experiments labeled good, keyholing, undermelting, and bead-up melt pools identified in melt pools throughout processing space (left), and finite element and experimental process map of melt pool areas with effective absorptivity values (right).

Similar results across the stainless steel alloys highlight a common problem. There is a very small region of processing space that is ideal for use in the ProX 200 L-PBF process at standard spot sizes. Additionally, the changing effective absorptivities and melt pool shapes makes identification of desired process parameters more difficult. Solutions to these identified problems are explored in section 6.3.3.

6.3.2 Spot Size Experiments

Spot size experiments were completed in the process not only to verify models and trends developed in Chapter 3:, but also to make adjustments to the process maps presented in section

6.3.1. This section will discuss results from experiments directed at eliminating specific keyholing melt pools labeled throughout 316L stainless steel power-velocity space. Figure 6-4 shows the labeled points from the process mapping experiments with nominal focus along with the points chosen for spot size adjustments. The chosen points are primarily in the keyholing region and have been chosen in such a way that a coarse process map can be formed from the resulting data.

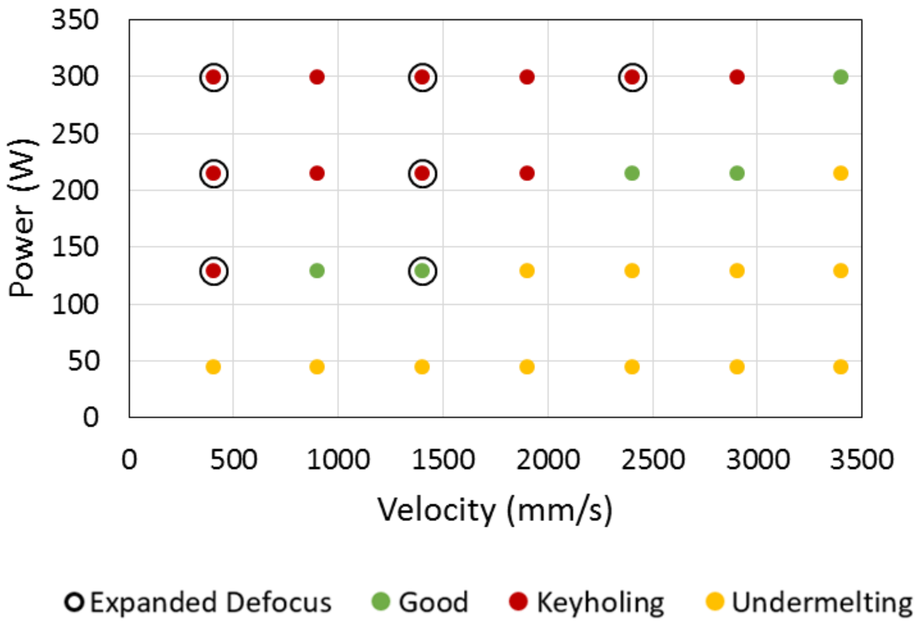

Figure 6-4: Labeled keyholing, "good", and undermelting melt pools from 316L experiments, and the points chosen for spot size adjustments

At each point chosen for adjusted spot size experiments, a specific spot size was chosen based on simulation point source widths and the keyholing threshold established in Chapter 4:. Point source width values in these experiments were based on simulation values and the effective absorptivity of 0.36 from the 1600 μm^2 constant area line used in the process map. This constant area line was chosen as it was the largest non-keyholing area line used in the process map. Figure 6-5 shows melt pools deposited at 300 W, 400 mm/s, and various spot sizes including the nominal case at a focus offset of 0 mm and estimated spot size of 30 μm from section 3.3.3. For this power-velocity combination, the melt pool produced with an estimated spot size of 165 μm would be the case chosen as a more ideal melt pool for an updated process map.

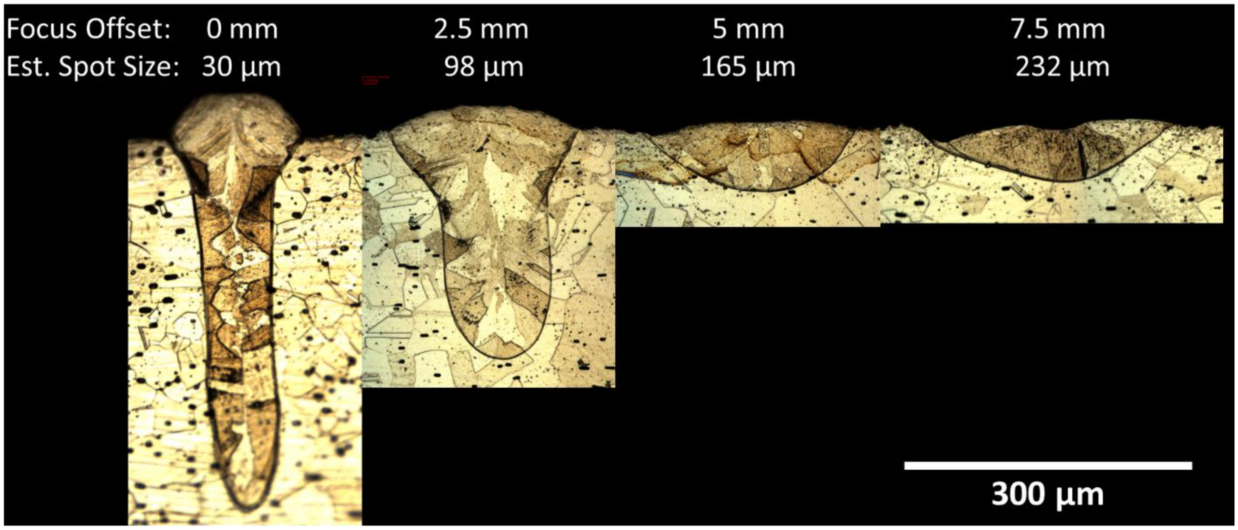

Figure 6-5: Cross section images of melt pools deposited at 300W, 400 mm/s, and various spot size values.

Spot size adjustments for the other selected power velocity combinations were also successful at preventing keyhole mode melting. Figure 6-6 shows results from two other selected power-velocity combinations; one case at 215 W and 1400 mm/s, and the other at 130 W and 400 mm/s. In both cases, the spot size adjustments intended to eliminate keyholing and give a smooth, arcing melt pool were successful in doing so. The findings of Chapter 4: were also successful in eliminating keyholing in melt pools at the other power-velocity combinations chosen for spot size adjustments in this chapter. Images of the other selected melt pools at the original and adjusted spot size settings are available in Appendix 5.

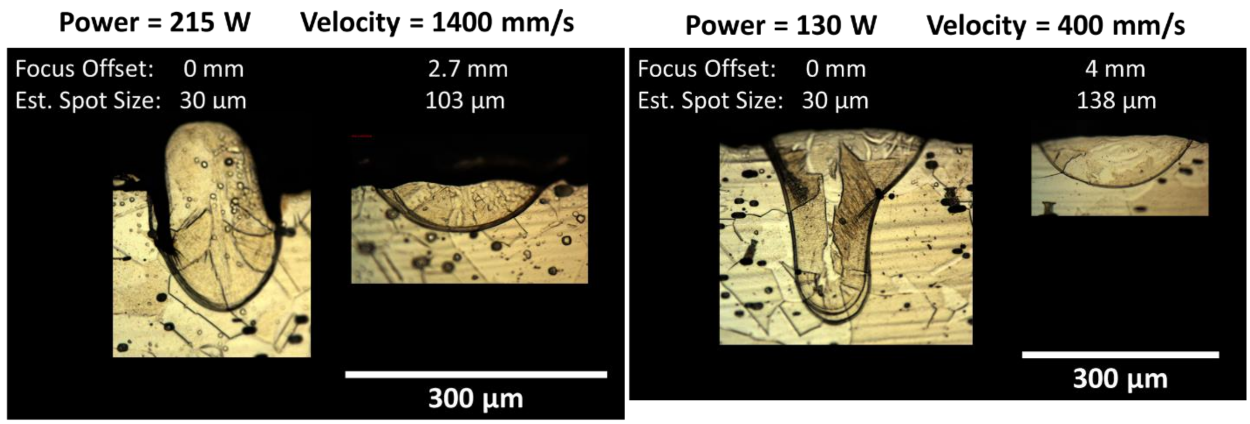

Figure 6-6: Cross section images of melt pools deposited at nominal and adjusted spot size values.

6.3.3 Expanding Processing Space

Using information presented in this thesis, the usable processing space can be increased through the intelligent control of spot size. Figure 6-7 outlines a method that can be implemented to increase the usable processing space. Step one begins with a process map generated from experimental measurements at a constant, nominal, spot size. Point source simulation data is fit to the measurements with different absorptivities for each constant area line. The limits of the usable processing space are bound by keyholing at high power and low velocity, undermelting at low power and high velocity, and bead-up at high power and high velocity. In step two, an effective absorptivity is selected from the largest non-keyholing melt pools, or from melt pools near the normalized spot size threshold for keyholing. Chapter 4: identifies a normalized spot size (σ/W_0) value of one as a threshold to avoid keyholing in multiple alloys.

Step three involves the creation of a new process map created using point source simulation data spread throughout processing space using the effective absorptivity identified in step two for all melt pool areas. Additionally, a specific spot size is assigned to each constant area line based on the normalized spot size requirements to avoid keyholing based on the identified normalized spot size threshold. Melt pool dimensions in this process map can be used to guide spot size changes for purposes beyond keyhole avoidance if it is desired.

Step four shows the identification of the usable processing space with the newly developed process map and spot sizes aimed at eliminating keyhole mode melting. The undermelting region remains constant in this case since no changes in layer thickness have been implemented. The limit for bead-up melt pools is based on a width to full length ratio calculated from point source simulations. Details on the threshold for bead-up melt pools are discussed in Chapter 4:. Step five, the final step, makes use of the relationships between normalized spot size, and width to full length ratio to further expand processing space. The new bead-up line is determined by increasing spot size of a certain melt pool area until the depth is equal to the layer thickness. The normalized spot size of the associated changes can be used to determine the maximum L_0/D_0 ratio that can be used while still remaining below the bead-up threshold for W/FL. It is important to note that the usable processing space gained between steps four and five will require additional spot size increases to avoid bead-up melt pools.

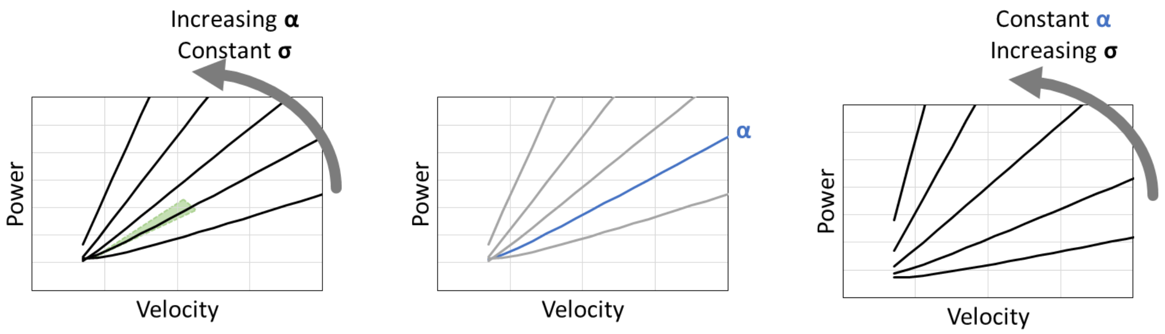

1: Process map created from experiments at nominal spot size. Small processing space identified due to keyholing, undermelting, and bead-up

2: Effective absorptivity identified for largest non-keyholing area

3: New process map developed based on simulation data and effective absorptivity and spot size adjustments

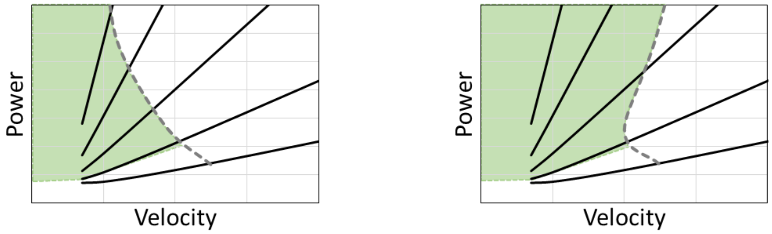

4: Expanded processing space identified for new process map with bead-up limit

5: Processing space further expanded to account for mitigation of bead-up via spot size increases

Figure 6-7: Steps taken to determine an expanded processing space that avoid keyholing, undermelting, and bead-up melt pools

The steps outlined above have been implemented for 316L stainless steel in the ProX 200 L-PBF process. Figure 6-8 shows plots that refer to steps one and four. On the left, the original process map created with nominal absorptivity and varying absorptivities to fit experimental and simulation data. A very narrow region of usable processing space is observed around the green, 1600 μm^2 area measurements.

On the right, a new area process map was developed based on expanded spot size experiments discussed in section 6.3.2. The area lines at high powers and low velocities have been modified as a result of the spot size changes. Details on the spot size changes suggested for 316L, and the other stainless steel alloys are available in Appendix 6. In the adjusted plot, the 13000 μm^2 line could no longer be created with the experiment set, and 6450 μm^2 and 3200 μm^2 have shifted to higher power regions with lower effective absorptivities. The new process map also has much more consistent effective absorptivities throughout processing space. The outlier is the 800 μm^2 case where the minimum spot size results in a higher normalized spot size and decreased melt pool areas. The "good" processing space is now only bound by the W/FL threshold for bead-up, and the minimum depth required to melt through the layer thickness. In this plot, W/FL is based on point source values from simulations. The only spot size requirements for this initial change in "good" processing space is to set the normalized spot size to a value of one.

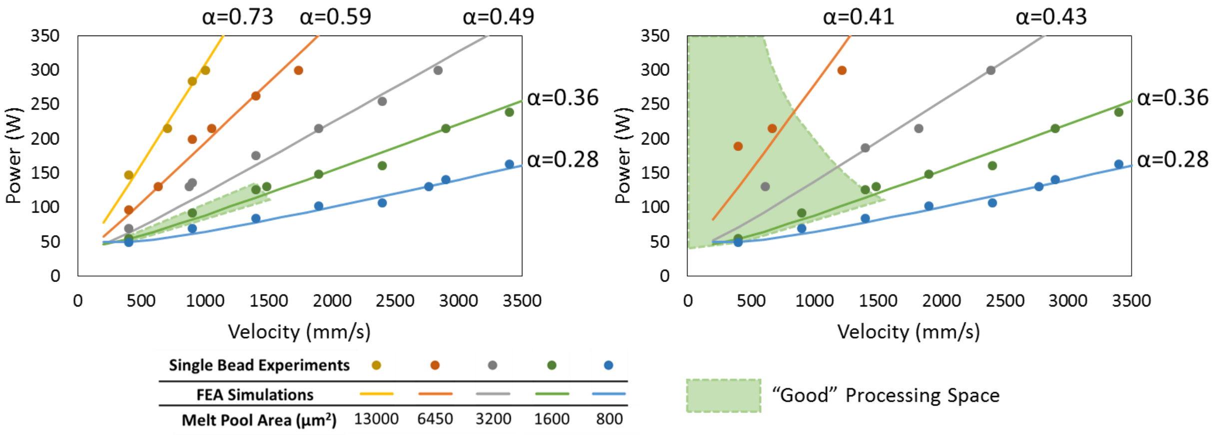

Figure 6-8: Processing space for 316L in the ProX 200 L-PBF process for nominal spot size (left), and variable spot size with original bead-up limit (right)

Where Figure 6-8 showed how spot size increases processing space when it is used to eliminate keyholing, it does not show how spot size can be used to further expand processing space by preventing the occurrence of bead-up melt pools. Figure 6-9 shows power-velocity space with a "good" processing space that has been expanded even further by increasing spot size to eliminate bead-up in some melt pools. It is important to note that the necessary spot size may be different for each power-velocity point in the specified processing space, and will still need to be balanced with hatch spacing and the fixed layer thickness to deposit successfully.

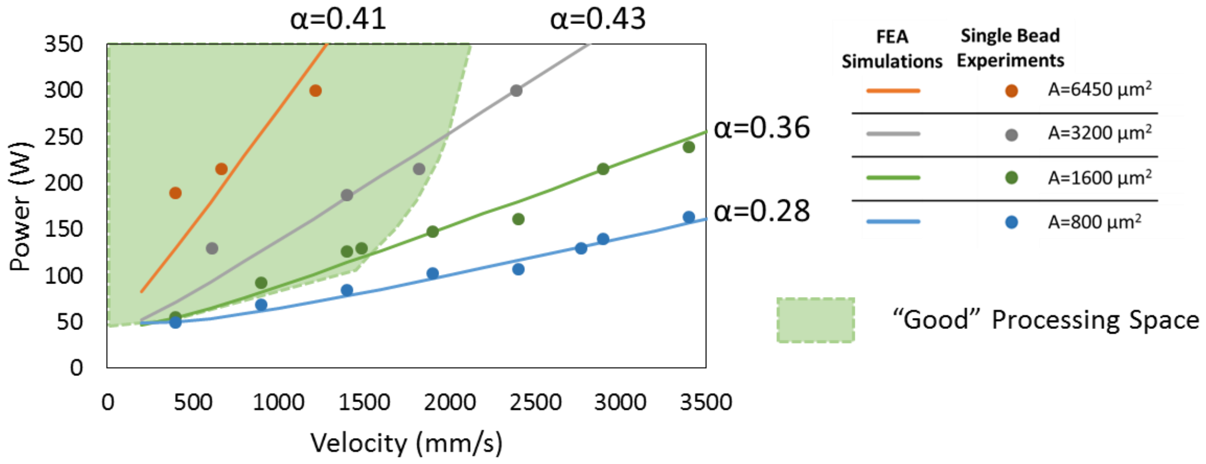

Figure 6-9: Expanded Processing space for 316L in the ProX 200 L-PBF process where increased spot size can eliminate keyholing and a portion of the bead-up region

6.4 Discussion

This chapter discusses the application of the findings earlier in the thesis that enable a user to expand the "good" processing space through specific spot size adjustments. Process maps were developed for three stainless steel alloys in the 3D Systems ProX 200 L-PBF process. The results showed a very small range where keyholing melt pools were not present and the melt pools were deep enough to melt through the layer thickness. Additionally, fitted simulation results required different effective absorptivity values for each line of constant area. Differences in effective absorptivity were due to increases in melt pool area in keyholing melt pools, and decreased area in small melt pools with larger normalized spot sizes. For 316L stainless steel, a selection of keyholing points were chosen for expanded focus experiments where specific spot sizes were chosen to eliminate keyholing based on the normalized spot size threshold suggested in Chapter 4:. In different L-PBF processes, the “good” processing window would differ based on the nominal spot size. For example, the EOS M 290 process would have a larger window at nominal parameters due to a larger spot size, but would be shifted to higher powers and lower velocities.

The suggested changes in spot size were successful in eliminating keyhole mode melting, and the new melt pool areas could be used to form an updated process map. Methods to expand processing space with increased spot size are presented, and the 316L experiments are used as a case study. An original process map was adjusted to account for spot size increases that eliminated keyholing melt pools, and more consistent effective absorptivities were observed. New limits on the usable processing space were also formed to account for the ability mitigate the presence bead-up melt pools by further increasing spot size. In general, the proposed method sets up guidelines for maximizing the “good” processing space through spot size modification.

Chapter 7: Conclusions

7.1 Conclusions

Additive manufacturing processes have the capability to transform the manufacturing industry by providing increased flexibility in part geometry and complexity. To take full advantage of the capabilities of AM, operators need to be able to produce parts throughout processing space while avoiding porosity and flaw formation. Work in this thesis analyzes the effects of three different process parameters, power, velocity, and spot size, on melt pool geometry. Ti-6Al-4V is process mapped in power-velocity space for the electron beam wire feed and laser powder feed processes. Relationships are also drawn between melt pool geometry and resulting prior beta grain width in the two processes. The process maps and microstructure relationships give insights into where melt pool sizes and Ti-6Al-4V beta grain sizes can be found throughout processing space.

Beam spot size has also been identified as having a major influence on melt pool geometry. Melt pool dimensions were normalized by dimensions generated by point heat source simulations, and spot size was normalized by the point heat source melt pool width. It was found that when normalized melt pool dimensions are plotted against normalized spot size, changes in melt pool dimensions grouped together based on the point source length to depth aspect ratio. These normalizations were used to describe how different melt pool dimensions changed with increasing spot size and compare against experimental measurements. It was also shown that experimental melt pool dimensions can be used to estimate how spot size changes with a focusing parameter in additive manufacturing processes; this is useful as direct-diameter measurements can often be challenging to perform.

The influence of spot size on the formation of keyhole mode melting and bead-up melt pools was determined; both of these melt pool morphologies can be a major source of porosity and flaws in additively manufactured parts. Increases in spot size have been shown to eliminate the presence of keyholing, and a normalized spot size threshold is proposed to prevent keyholing in five alloys. Width to full length ratio has been identified by previous authors as an indicator of bead-up melt pools. Changes in the ratio with normalized spot size have been presented and a suggested threshold to avoid bead-up melt pools is verified.

Analysis of the effects of spot size on Ti-6Al-4V beta microstructure is also presented in this thesis. Normalized cooling rates are plotted against normalized spot sizes for different length to width ratios, and beam energy distributions. Contrary to expectations, experimental measurements for prior beta grain width did not have a relationship with spot size. This suggests that relationships developed between melt pool geometry and prior beta grain width in Ti-6Al-4V will only hold true for consistent melt pool shapes.

The information presented is combined to suggest a robust method for increasing the usable processing space by expanding the limits for the onset of keyholing and bead-up melt pools. The method is applied to 316L stainless steel in the 3D Systems ProX 200 L-PBF process, and is able to drastically increase the usable processing space by avoiding keyholing and bead-up. In addition to expanding processing space, the method results in more consistent effective absorptivities that relate simulation results to experimental measurements. The proposed method to expand processing space can be used to reliably produce parts using a larger range of a process's capabilities.

7.2 Implications

Where previous work has named the general effects of spot size on melt pool geometry, flaws, and microstructure, this research found detailed relationships between spot size and various process outcomes. Some of the important implications of this research is presented below.

- Expansion of the Ti-6Al-4V electron beam wire feed process map, and verification of geometry-microstructure relationships. This work enables machine operators greater knowledge of how melt pool dimensions change throughout processing space, which allows for faster development of parameters and shorter qualification times. Relationships developed by Gockel [81] were verified at higher powers and the developed body of knowledge allows for easier development of location specific microstructure in the electron beam wire feed process. Monitoring melt pool width opens up real time indirect control of microstructure for the electron beam wire feed process.
- Process mapping Ti-6Al-4V in the LENS laser powder feed process and development of relationships between geometry and microstructure. Similar to the work in the electron beam wire feed process, this work gives insights into the geometry produced by power-velocity combinations throughout processing space. Relationships between melt pool full length, velocity, and prior beta grain width aide in the development of location specific microstructure. Monitoring melt pool full length and velocity opens up real time indirect control of microstructure for the laser powder feed process.
- Development of relationships between beam spot size and the resulting melt pool dimensions across any alloy and process Relationships between spot size and melt pool dimensions helps in the designing of process parameters when normalized spot size is not

consistent. Modification of spot size can be used to create melt pools of preferable melt pool geometry that can increase build rate or decrease porosity.

- Identification of methods to prevent keyhole mode melting through spot size increases. Increases to beam spot size have been shown to be capable of eliminating keyhole mode melting. Normalized spot size thresholds have been proposed to reliably avoid keyholing melt pools in five different alloys. These findings give guidelines to avoid keyholing that can introduce variability and porosity into an additively manufactured part.
- Identification of methods to prevent bead-up melt pools through spot size increases. Similar to keyholing, findings showed that bead-up melt pools can be avoiding through increases in spot size. Width to full length thresholds (for bead-up) are verified, and changes in the ratio with normalized spot size are presented. The findings related to bead-up melt pools allow an operator to methodically avoid lack-of-fusion issues associated with bead up melt-pools.
- Identifying effects of spot size on Ti-6Al-4V prior beta grain width. Simulation cooling rates and experimental prior beta grain widths were compared against normalized spot size. While cooling rates had large increases at large spot sizes, no relation was observed between prior beta grain width and spot size. This suggests that when relationships between Ti-6Al-4V microstructure and melt pool geometry are being used, the trends only hold true for consistent cross-sectional aspect ratios.
- Expansion of usable processing space through spot size modification. Findings from this dissertation are combined to develop a method for significantly expanding the usable processing space. Spot size is modified according to thresholds for keyholing and bead-up melt pools to expand the usable processing space, and the method is demonstrated for 316L

stainless steel in the ProX200 L-PBF process. This method can be used to expand the usable processing space with minimal porosity in the part. This allows operators to take advantage of build rate, microstructural, or other qualities present in different regions of processing space.

7.3 Future Work

A primary theme of this dissertation is the relation of process parameters to melt pool geometry and other process outcomes. Detailed knowledge of the effects of process parameters help to prevent the formation of porosity, and can be used to tailor microstructure or other preferable outcomes. While this research makes significant progress in understanding the effects of power, velocity, and spot size, there is still room for more progress. Suggested areas for future work are listed below.

- Effects of other process parameters. While the effects of some primary process parameters have been explored in this work, the effects of other important variables (material feed rate, hatch spacing, etc.) on melt pool geometry, microstructure, etc. have not been thoroughly explored.
- Effects in different deposition geometries. Results presented for process maps and spot size effects in this dissertation were based on models and experiments in steady state melt pools in bulk material. Analysis determining if these trends hold for other deposition geometries should be completed before the findings are applied in regions of parts with different geometries.
- Verification in multi-layer depositions. Verification of many findings in this research was limited to single track depositions with no added material. Further analysis is required to

determine if the findings are affected by added material either in the form of a powder layer, or fed material.

- Thresholds in other alloys. Thresholds found for keyholing and bead-up melt pools likely vary based on the alloy system being used. While many of the alloys used in this research yielded similar results, material properties do have an influence on the thresholds found for different materials.

References

[1] I. Gibson, D. Rosen and B. Stucker, Additive Manufacturing Technologies, Second ed., Springer, 2015.

[2] Wohlers Associates, "Wohlers Report 2013," Fort Collins, 2013.

[3] Arcam AB, "Metal Powders," [Online]. Available: http://www.arcam.com/technology/products/metal-powders/. [Accessed 12 Frebruary 2016].

[4] EOS GmbH, "Materials for Metal Manufacturing," [Online]. Available: http://www.eos.info/material-m. [Accessed 12 February 2016].

[5] K. M. Taminger and R. A. Hafley, "Electron Beam Freeform Fabrication for Cost Effective Near-Net Shape Manufacturing," in *NATO/RTOAVT-139 Specialist' Meeting on Cost Effective Manufacture vie Net Shape Processing*, Amsterdam, Netherlands, 2006.

[6] C. Atwood, M. Griffith, L. Harwell, E. Schlienger, M. Ensz, J. Smugeresky, T. Romero, D. Greene and D. Reckaway, "Laser Engineered Net Shaping (LENS): A Tool for Direct Fabrication of Metal Parts," Sandia National Laboratories, Albuquerque, NM, 1998.

[7] R. Grylls, "Laser Engineered Net Shapes," *Advanced Materials & Processes*, vol. 161, no. 1, pp. 45-46, 2003.

[8] M. Kerschbaumer and G. Ernst, "Hybrid Manufacturing Process for Rapid High Performance Tooling Combining High Speed Milling and Laser Cladding," in *23rd Annual Congress on Applications of Lasers and Electro-Optics*, 2004.

[9] Sciaky Inc., "ELECTRON BEAM ADDITIVE MANUFACTURING (EBAM™)," [Online]. Available: http://www.sciaky.com/additive-manufacturing/wire-am-vs-powder-am. [Accessed 12 February 2016].

[10] Optomec, "LENS Materials," [Online]. Available: http://www.optomec.com/3d-printed-metals/lens-materials/. [Accessed 12 February 2016].

[11] F. G. Arcella and F. H. Froes, "Producing Titanium Aerospace Components from Powder Using Laser Forming," *JOM,* pp. 28-30, May 2000.

[12] L. Robinson and J. Scott, "Layers of Complexity: Making the Promises Possible for Additive Manufacturing of Metals," *JOM,* vol. 66, no. 11, pp. 2194-2207, 2014.

[13] M. Seifi, A. Salem, J. Beuth, O. Harrysson and J. Lewandowski, "Overview of Materials Qualification Needs for Metal Additive Manufacturing," *JOM,* vol. 68, no. 3, pp. 747-764, 2016.

[14] J. Beuth, J. Lewandowski, O. Harrysson, B. Stucker and N. Klingbeil, "Rapid Qualification Methods for Powder Bed Direct Metal AM Processes," in *Solid Freeform Fabrication Symposium*, Austin, TX, 2014.

[15] S. Tammas-Williams and I. Todd, "Design for Additive Manufacturing with Site-Specific Properties in Metals and Alloys," *Scripta Materialia,* 2016.

[16] K. P. Cooper and S. G. Lambrakos, "Thermal Modeling of Direct Digital Melt-Deposition Processes," *Journal of Materials Engineering and Performance,* vol. 20, no. 1, pp. 48-56, 2010.

[17] J. Beuth and N. Klingbeil, "The Role of Process Variables in Laser-Based Direct Metal Solid Freeform Fabrication," *JOM,* pp. 36-39, 2001.

[18] N. W. Klingbeil, J. W. Zinn and J. L. Beuth, "Measurement of Residual Stresses in Parts Created by Shape Deposition Manufacturing," in *Solid Freeform Fabrication Symposium,* Austin, TX, 1997.

[19] N. W. Klingbeil, J. L. Beuth, R. K. Chin and C. H. Amon, "Residual Stress-Induced Warping in Direct Metal Solid Freeform Fabrication," *International Journal of Mechanical Sciences,* vol. 44, pp. 57-77, 2002.

[20] N. W. Klingbeil, J. L. Beuth, R. K. Chin and C. H. Amon, "Measurement and Modeling of Residual Stress-Induced Warping in Direct Metal Deposition Processes," in *Solid Freeform Fabrication Symposium,* Austin, TX, 1998.

[21] A. Vasinonta, J. Beuth and M. Griffith, "Process Maps for Predicting Residual Stress and Melt Pool Size in the Laser-Based Fabrication of Thin-Walled Structures," *Journal of Manufacturing Science and Engineering,* vol. 129, no. 1, pp. 101-109, 2007.

[22] A. Vasinonta, J. Beuth and M. Griffith, "A Process Map for Consistent Build Conditions in the Solid Freeform Fabrication of Thin-Walled Structures," *ASME Journal of Manufacturing Science and Engineering*, vol. 123, pp. 615-622, 2001.

[23] J. Fox, "Transient Melt Pool Response in Additive Manufacturing of Ti-6Al-4V (Doctoral dissertation)," Carnegie Mellon University, Pittsburgh, PA, 2015.

[24] E. Soylemez, J. Beuth and K. Taminger, "Controlling Melt Pool Dimensions Over a Wide Range of Material Deposition Rates in Electron Beam Additive Manufacturing," in *Solid Freeform Fabrication Symposium*, Austin, TX, 2010.

[25] C. Montgomery, J. Beuth, L. Sheridan and N. Klingbeil, "Process Mapping of Inconel 625 in Laser Powder Bed Additive Manufacturing," *SFF Symposium Proceedings,* pp. 1195-1204, August 2015.

[26] A. Birnbaum, P. Aggarangsi and J. Beuth, "Process Scaling and Transient Melt Pool Size Control in Laser-Based Additive Manufacturing Processes," in *Solid Freeform Fabrication Conference*, Austin, TX, 2003.

[27] J. Beuth, J. Fox, J. Gockel, C. Montgomery, R. Yang, H. Qiao, E. Soylemez, P. Reeseewatt, A. Anvari, S. Narra and N. Klingbeil, "Process Mapping for Qualification Across Multiple Direct Metal Additive Manufacturing Processes," in *Solid Freeform Fabrication Symposium*, Austin, TX, 2013.

[28] P. Kobryn and S. Semiatin, "Microstructure and Texture Evolution During Solidification Processing of Ti-6Al-4V," *Journal of Materials Processing Technology,* vol. 13, pp. 330-339, 2003.

[29] P. Kobryn, E. Moore and S. Semiatin, "The Effect of Laser Power and Traverse Speed on Microstructure, Porosity and Build Height in Laser Deposited Ti-6Al-4V," *Scripta Materialia,* vol. 43, pp. 299-305, 2000.

[30] N. Aboulkhair, N. Everitt, I. Ashcroft and C. Tuck, "Reduscing Porosity in AlSi10Mg Parts Processed by Selectove Laser Melting," *Additive Manufacturing,* vol. 1, no. 4, pp. 77-86, 2014.

[31] H. Gong, K. Rafi, H. Gu, T. Starr and B. Stucker, "Analysis of Defect Generation in Ti-6Al-4V Parts Made Using Powder Bed Fusion Additive Manufacturing Processes," *Additive Manufacturing,* vol. 1, no. 4, pp. 87-98, 2014.

[32] Y.-F. Tzeng, "Effects of Operating Parameter on Surface Quality for the Pulsed Laser Welding of Zinc-Coated Steel," *Journal of Materials Processing Technology,* vol. 100, pp. 163-170, 2000.

[33] A. Safdar, H. Z. He, L.-Y. Wei, A. Snis and L. E. Chavez de Paz, "Effect of process parameters settings and thickness on surface roughness of EBM produced Ti-6Al-4V," *Rapid Prototyping Journal,* vol. 18, no. 5, pp. 401-408, 2012.

[34] D. B. Hann, J. Iammi and J. Folkes, "A simple methodology for predicting laserweld properties from material and laser parameters," Journal of Physics D: Applied Physics, 2011.

[35] M. Seifi, D. Christiansen, J. Beuth, O. Harrysson and J. Lewandowski, "Process Mapping, Fracture and Fatigue Behavior of Ti-6Al-4V Produced by EBM Additive Manufacturing," in *Ti-2015: The 13th World Conference on Titanium*, San Diego, CA, 2015.

[36] A. Okunkova, P. Peretyagin, Y. Vladimirov, M. Volosova, R. Torrecillas and S. V. Federov, "Laser-Beam Modulation to Improve Effiviency of Selective Laser Melting for Metal Powders," in *Proc. SPIE, Laser Sources and Applications II*, Brussels, Belgium, 2014.

[37] P. Y. Peretyagin, I. V. Zhirnov, Y. G. Vladimirov, T. V. Tarasova and A. A. Okun'kova, "Track Geometry in Selective Laser Melting," *Russian Engineering Research*, vol. 35, no. 6, pp. 473-476, 2015.

[38] T. T. Roehling, S. S. Q. Wu, S. A. Khairallah, J. D. Roehling, S. S. Soezeri, M. F. Crumb and M. J. Matthews, "Modulating Laser Intensity Profile Ellipticity for Microstructural Control During Metal Additive Manufacturing," *Acta Materialia*, pp. ISSN 1359-6454, 2017.

[39] R. P. Mudge and R. N. Wald, "Laser Engineered Net Shaping Advances Additive Manufacturing and Repair," *Welding Journal*, pp. 44-48, January 2007.

[40] D. Miller, C. Deckard and J. Williams, "Variable beam size SLS workstation and enhanced SLS model," *Rapid Prototyping Journal*, vol. 3, no. 1, pp. 4-11, 1997.

[41] G. Bi, C. N. Sun and A. Gasser, "Study on Influential Factors for Process Monitoring and Control in Laser Aided Additive Manufactring," *Journal of Materials Processing Technology,* vol. 213, pp. 463-468, 2013.

[42] H. E. Helmer, C. Körner and R. F. Singer, "Additive manufacturing of nickel-based superalloy Inconel 718 by selective electron beam melting: Processing window and microstructure," *Journal of Materials Research,* vol. 29, no. 17, pp. 1987-1996, September 2014.

[43] C. A. Walsh, "Laser Welding - Literature Review," Materials Science and Metallurgy Department, University of Cambridge, 2002.

[44] G. Verhaeghe, P. Hilton and TWI Ltd, "The effect of spot size and laser beam quality on welding," *International Congress on Applications of Lasers & Electro-Optics*, 2005.

[45] J. T. Norris, C. V. Robino, D. A. Hirschfeld and M. J. Perricone, "Effects of Laser Parameters on Porosity Formation: Investigating Millimeter Scale Continuous Wave Nd: YAG Laser Welds," *Welding Journal,* pp. 198-203, October 2011.

[46] J. Zhou and H.-L. Tsai, "Porosity Formation and Prevention in Pulsed Laser Welding," *Journal of Heat Transfer,* vol. 129, no. 8, pp. 1014-1024, August 2007.

[47] W. E. King, H. D. Barth, V. M. Castillo, G. F. Gallegos, J. W. Gibbs, D. E. Hahn, C. Kamath and A. M. Rubenchik, "Observation of keyhole-mode laser melting in laser powder-bed fusion additive manufacturing," *Journal of Materials Processing Technology,* vol. 214, no. 12, pp. 2915-2925, December 2014.

[48] R. Dinwiddie, R. Dehoff, P. Lloyd, L. Lowe and J. Ulrich, "Thermographic In-Situ Process Monitoring of the Electon Beam Melting Technology used in Additive Manufacturing," in *Proceedings of SPIE,* San Francisco, CA, 2013.

[49] M. L. Griffith, W. H. Hofmeister, G. A. Knorovsky, D. O. MacCallum, E. M. Schlienger and J. E. Smugersky, "Direct Laser Additive Fabrication System with Image Feedback Control". United States Patent 6,459,951 B1, 1 Oct. 2002.

[50] W. Hofmeister and M. Griffith, "Solidification in Direct Metal Deposition by LENS Processing," *JOM,* vol. 53, no. 9, pp. 30-34, 2001.

[51] D. Hu and R. Kovacevic, "Sensing, Modelling and Control for Laser-Based Additive Manufacturing," *International Journal of Machine Tools and Manufacture,* vol. 43, no. 1, pp. 51-60, 2003.

[52] L. Song and J. Mazumder, "Feedback Control of Melt Pool Termperature During Laser Cladding Process," *IEEE Transactions on Control Systems Technology,* vol. 19, no. 6, pp. 1349-1356, 2011.

[53] L. Song, V. Bagavath-Singh, B. Dutta and J. Mazumder, "Control of Melt Pool Temperature and Deposition Height During Direct Metal Deposition Process," *International Journal of Advanced Manufacturing Technology,* vol. 58, no. 1, pp. 247-256, 2012.

[54] T. Craeghs, F. Bechmann, S. Berumen and J.-P. Kruth, "Feedback Control of Layerwise Laser Melting using Optical Sensors," *Physics Procedia,* vol. 5, pp. 505-514, 2010.

[55] T. Craeghs, S. Clijsters, E. Yasa and J.-P. Kruth, "Online Quality Control of Selective Laser Melting," in *Solid Freeform Fabrication,* Austin, TX, 2011.

[56] J. Mireles, S. Ridwan, P. Morton, A. Hinojos and R. Wicker, "Analysis and Correction of Defects within Parts Fabricated using Powder Bed Fusion Technology," *Surface Topography: Metrology and Properties,* vol. 3, no. 3, 2015.

[57] B. Fisher, "Thermal Imaging and Feedback Control of Ti64 EBM (Internal Report)," Carnegie Mellon University, Pittsburgh, PA, 2016.

[58] J. Jacobsmuhlen, S. Kleszczynski, G. Witt and D. Merhof, "Detection of Elevated Regions in Surface Images from Laser Beam Melting Processes," in *IECON,* Yokohama, 2015.

[59] L. Scime, "Anomaly Detection and Classification in a Laser Powder Bed Additive Manufacturing Process using a Trained Computer Vision Algorithm (Internal Report)," Carnegie Mellon University, Pittsburgh, PA, 2017.

[60] G. Tapia and A. Elwany, "A Review on Process Monitoring and Control in Metal-Based Additive Mnaufacturing," *Journal of Manufacturing Science and Engineering,* vol. 136, pp. 060801-1 - 060801-10, 2014.

[61] E. Akman, A. Demir, T. Canel and T. Sinmazcelik, "Laser Welding of Ti6Al4V titanium alloys," *Journal of Materials Processing Technology,* vol. 209, no. 8, pp. 3705-3713, April 2009.

[62] J. D. Madison and L. K. Aagesen, "Quantitative characterization of porosity in laser welds of stainless steel," *Scripta Materialia,* vol. 67, no. 9, pp. 783-786, November 2012.

[63] R. Rai, J. W. Elmer, T. A. Palmer and T. DebRoy, "Heat transfer and fluid flow during keyhole mode laser welding of tantalum, Ti–6Al–4V, 304L stainless steel and vanadium," *Journal of Physics D: Applied Physics,* vol. 40, no. 18, pp. 5753-5766, August 2007.

[64] P. S. Wei and T. C. Chao, "The Effects of Entrainment on Pore Shape in Keyhole Mode Welding," *Journal of Heat Transfer,* vol. 137, August 2015.

[65] M. Pastor, H. Zhao, R. P. Martukanitz and T. Debroy, "Porosity, Underfill and Magnesium Loss during Contiunous Wave Nd:YAG Laser Welding of Thin Plates of Aluminum Alloys 5182 and 5754," *Welding Research Supplement,* pp. 207s-216s, 1999.

[66] W. Tan and Y. Shin, "Analysis of Multi-Phase Interaction and Its Effects on Keyhole Dynamics with a Multi-Physics Numerical Model," *Journal of Physics D: Applied Physics,* vol. 47, 2014.

[67] W. Tan, N. Bailey and Y. Shin, "Investigation of Keyhole Plume and Molten Pool Based on a Three-Dimensional Dynamic Model with Sharp Interface Formulation," *Journal of Physics D: Applied Physics,* vol. 46, 2013.

[68] F. Verhaeghe, T. Craeghs, J. Heulens and L. Pandelaers, "A pragmatic model for selective laser melting with evaporation," *Acta Materialia,* vol. 57, no. 20, pp. 6006-6012, December 2009.

[69] R. Cunningham, S. Narra, C. Montgomery, J. Beuth and A. Rollett, "Synchrotron-Based X-ray Microtomography Characterization of the Effect of Processing Variables on Porosity Formation in Laser Powder-Bed Fusion Additive Manufacturing of Ti-6Al-4V," *JOM,* Vols. DOI: 10.1007/s11837-016-2234-, 2017.

[70] R. Cunningham, S. Narra, T. Ozturk, J. Beuth and A. Rollet, "Evaluating the Effect of Processing Parameters on Porosity in Electron Beam Melted Ti-6Al-4V via Synchrotron X-ray Microtomography," *JOM,* vol. 68, no. 3, pp. 765-771, 2016.

[71] M. Tang, P. C. Pistorius and J. L. Beuth, "Prediction of Lack-of-Fusion Porosity for Powder Bed Fusion," *Additive Manufacturing,* vol. 14, pp. 39-48, 2017.

[72] K. C. Mills, B. J. Keene, R. F. Brooks and A. Shirali, "Marangoni Effects in Welding," *Philosophical Transactions of the Royal Society A,* vol. 356, no. 1739, pp. 911-925, 1998.

[73] V. A. Nemchinsky, "The Role of Thermocapillary Instability in Heat Transfer in a Liquid Metal Pool," *International Journal of Heat and Mass Transfer,* vol. 40, no. 4, pp. 881-891, 1997.

[74] U. Gratzke, P. D. Kapadia, J. Dowden, J. Kroos and G. Simon, "Theoretical Approach to the Humping Phenomenon in Welding Processes," *Journal of Physics D: Applied Physics,* vol. 25, no. 11, pp. 1640-1647, 1992.

[75] I. Yadroitsev, A. Gusarov, I. Yadroitsava and I. Smurov, "Single Track Formation in Selective Laser Melting of Metal Powders," *Journal of Materials Processing Technology,* vol. 210, pp. 1624-1631, 2010.

[76] S. Kou and Y. H. Wang, "Weld Pool Convection and Its Effect," *Welding Research Supplement,* pp. 63s-70s, March 1986.

[77] P. A. Kobryn and S. L. Semiatin, "The Laser Additive Manufacture of Ti-6Al-4V," *JOM,* pp. 40-42, 2001.

[78] S. Bontha and N. Klingbeil, "Thermal Process Maps for Controlling Mictostructure in Laser-Based Solid Freeform Fabrication," in *Solid Freeform Fabrication Symposium,* Austin, TX, 2003.

[79] S. Bontha, C. Brown, D. Gaddam, N. W. Klingbeil, P. A. Kobryn, H. L. Fraser and J. W. Sears, "Effects of Process Variables and Size Scale on Solidification Microstructure in

Laser-Based Solid Freeform Fabrication of Ti-6Al-4V," in *Solid Freeform Fabrication Symposium*, Austin, TX, 2004.

[80] S. Bontha, N. Klingbeil, P. Kobryn and H. L. Fraser, "Effects of Process Variables and Size Scale on Solidification Microstructure in Beam-Based Fabrication of Bulky 3D Structures," *Materials Science and Engineering*, vol. 513, pp. 311-318, 2009.

[81] J. Gockel, *Integrated Control of Solidification Microstructure and Melt Pool Dimensions in Additive Manufacturing of Ti-6Al-4V (Doctoral dissertation)*, PhD Thesis: Carnegie Mellon University, 2014.

[82] J. Gockel, J. Fox, J. Beuth and R. Hafley, "Integrated Melt Pool and Microstructure Control for Ti-6Al-4V Thin Wall Additive Manufacturing," *Materials Science and Technology*, vol. 31, no. 8, pp. 912-916, 2015.

[83] J. Gockel, J. Beuth and K. Taminger, "Integrated Control of Solidification Microstructure and Melt Pool Dimension in Electron Beam Wire Feed Additive Manufacturing of Ti-6Al-4V," *Additive Manufacturing*, vol. 1, pp. 119-126, 2014.

[84] W. Tan and Y. Shin, "Multi-Scale Modeling of Solidification and Microstructure Developement in Laser Keyhole Welding Process for Austenitic Stainless Steel," *Computational Materials Science*, vol. 98, pp. 446-458, 2015.

[85] R. C. Dykhuizen and D. Dobranich, "Cooling Rates in the LENS Process," Sandia National Laboratories, Albuquerque, NM, 1998.

[86] S. M. Kelly, "Thermal and Microstructure Modeling of Metal Deposition Processes with Application to Ti-6Al-4V," Virginia Polytechnic Institute and State University, PhD Thesis, 2004.

[87] J. Lin, Y. Lv, Y. Liu, Z. Sun, K. Wang, Z. Li, W. Yixiong and B. Xu, "Microstructural Evolutionand Mechanical Property of Ti-6Al-4V Wall Deposited by Continuous Plasma Arc Additive Manufacturing Without Post Heat Treatment," *Journal of the Mechanical Behavior of Biomedical Materials,* vol. 69, pp. 19-29, 2017.

[88] A. A. Antonysamy, "Microstructure, Texture, and Mechanical Property Evolution during Additive Manufacturing of Ti6Al4V Alloy for Aerospace Applications," University of Manchester, PhD Thesis, 2012.

[89] S. P. Narra, R. Cunningham, D. Christiansen, J. Beuth and A. D. Rollett, "Toward Enabling Spatial Control of Ti-6Al-4V Solidification Microstructure in the Electron Beam Melting Process," in *SFF Symposium,* Austin, TX, 2015.

[90] L. E. Murr, E. V. Esquivel, S. A. Quinones, S. M. Gaytan, M. I. Lopez, E. Y. Martinez, F. Medina, D. H. Hernandez, E. Martinez, J. L. Martinez, S. W. Stafford, D. K. Brown, T. Hoppe, W. Meyers, U. Lindhe and R. B. Wicker, "Microstructures and Mechanical Properties of Electron Beam-Rapid Manufactured Ti-6Al-4V Biomedical Prototypes Compared to Wrought Ti-6Al-4V," *Materials Characterization,* vol. 60, pp. 96-105, 2009.

[91] D. Rosenthal, "The Theory of Moving Sources of Heat and Its Application to Metal Treatments," *Transactions of the A.S.M.E.,* pp. 849-866, 1946.

[92] N. Christensen , V. Davies and K. Gjermundsen, "The Distribution of Temperature in Arc Welding," *British Welding Journal*, vol. 12, no. 2, pp. 54-75, 1965.

[93] T. W. Eagar and N. S. Tsai, "Temperature Fields Produced by Traveling Distributed Heat Sources," *Welding Research Supplement*, pp. 346-355, 1983.

[94] R. C. Dykhuizen and D. Dobranich, "Analytical Thermal Models for the LENS Process," Sandia National Laboratories, Albuquerque, NM, 1998.

[95] D. Dobranich and R. C. Dykhuizen, "Scoping Thermal Calculations of the LENS Process," Sandia National Laboratories, Albuquerque, NM, 1998.

[96] L. Wang, S. Felicelli, Y. Gooroochurn, P. T. Want and M. F. Horstemeyer, "Optimization of the LENS Process for Steady Molten Pool Size," *Materials Sciance and Engineering,* vol. 474, pp. 148-156, 2008.

[97] P. Michaleris, "Modeling Metal Deposition in Heat Transfer Analyses of Additive Manufacturing Processes," *Finitie Elements in Analysis and Design,* vol. 86, pp. 51-60, 2014.

[98] E. Denlinger, J. Heigel, P. Michaleris and T. Palmer, "Effect of Inter-Layer Dwell Time on Distortion and Residual Stress in Additive Manufacturing of Titanium and Nickel Alloys," *Journal of Materials Processing Technology,* vol. 215, pp. 123-131, 2015.

[99] W. E. King, A. T. Anderson, R. M. Ferencz, N. E. Hodge, C. Kamath, S. A. Khairallah and A. M. Rubenchik, "Laser Powder Bed Fusion Additive Manufacturing of Mateal; Physica, Computational, and Materials Challenges," *Applied Physics Reviews,* vol. 2, no. 4, 2015.

[100] S. Khairallah, A. Anderson, A. Rubenchik and W. King, "Laser Powder-Bed Fusion Additive Manufacturing: Physics of Complex Melt Flow and Formation Mechanisms of Pores, Splatter, and Denudation Zones," *Acta Materialia,* vol. 108, pp. 36-45, 2016.

[101] P. Nie, O. A. Ojo and Z. Li, "Numerical Modeling of Microstructure Evolution During Laser Additive Manufacturing of a Nickel-Based Superalloy," *Acta Materialia,* vol. 77, pp. 85-95, 2014.

[102] A. Zinoviev, O. Zinovieva, V. Ploshikhin, V. Romanova and R. Balokhonov, "Evolution of Grain Structure During Laser Additive Manufacturing. Simulation by a Cellular Automata Method," *Materials and Design,* vol. 106, pp. 321-329, 2016.

[103] D. Clymer, J. Beuth and J. Cagan, "Additive Manufacturing Process Design," in *Solid Freeform Fabrication Symposium,* Austin, TX, 2016.

[104] M. Donachie, Titanium: A Technical Guide, ASM International, 2007.

[105] P. W. Early and S. J. Burns, "Improved Toughness From Prior Beta Grains in Ti-6Al-4V," *Scripta Metallurgica,* vol. 11, pp. 867-869, 1977.

[106] R. Filip, K. Kubiak, W. Ziaja and J. Sieniawski, "The Effect of Microstructure on the Mechanical Properties of Two-Phase Titanium Alloys," *Journal of Materials Processing Technology,* vol. 133, no. 1-2, pp. 84-89, 2003.

[107] C. Leyens and M. Peters, Titanium and Titanium Alloys: Fundamentals and Applications, Beerfelden, Germany: Wiley-VCH Verlag GmbH & Co. KGaA, 2005.

[108] Y. Arata and I. Miyamoto, "Laser Welding," *Technocrat,* vol. 11, no. 5, pp. 33-42, 1978.

[109] M. Boivineau, C. Cagran, D. Doytier, V. Eyraud, M. Nadal, B. Wilthan and G. Pottlacher, "Thermophysical Properties of Solid and Liquid Ti-6Al-4V (TA6V) Alloy," *International Journal of Thermophysics,* vol. 27, no. 2, pp. 507-529, 2006.

[110] J. Li, L. Johnson and W. Rhim, "Thermal Expansion of Liquid Ti-6Al-4V Measure by Electrostatic Levitation," *Applied Physics Letters,* vol. 89, 2006.

[111] Dassault Systems, *Abaqus Theory Guide: 2.11.1 Uncoupled heat transfer analysis,* Simulia - Abaqus 6.14, 2014.

[112] ASTM Standard E112-13, "Standard Test Methods for Determining Average Grain Size," ASTM International, West Conshocken, PA, 2013.

[113] D. Wright, "Beamwidths of a Diffracted Laser using Four Proposed Methods," *Optical and Quantum Electronics,* vol. 24, pp. S1129-S1135, 1992.

[114] S. Goodrich, *SI1866_11AUG16_200w.foc,* Pittsburgh, PA: EOS GmbH, 2016.

[115] S. Goodrigh, *SI1866_11AUG16_40w.foc*, Pittsburgh, PA: EOS GmbH, 2016.

[116] S. Narra, "Melt pool area of select power- velocity combinations in IN718 and Ti-6Al-4V," Carnegie mellon University. Internal Report, Pittsburgh, PA, 2017.

[117] R. Egerton, "Chapter 2: Electron Optics," in *Physical Principles of Electron Microscopy: An Introduction to TEM, SEM, and AEM*, Springer, 2005, pp. 27-55.

[118] D. Weill, J. Rice, M. Shaffer and J. Donovan, "Chapter Four: The Electron Beam and Electron Optics," in *Electron Beam MicroAnalysis Theory and Application*, Eugene, OR, University of Oregon Center for Advanced Materials Characterization in Oregon (CAMCOR), 2013, pp. 4-1 to 4-30.

[119] Neue Materialien Furth GMBH, "Selective Electron Beam Melting (SEBM) of Metals," [Online]. Available: http://www.nmfgmbh.de. [Accessed 9 September 2015].

[120] J. W. Elmer, W. H. Giedt and T. W. Eagar, "The Transition from Shallow to Deep Penetration during Electron Beam Welding," *Welding Research*, pp. 167-s - 176-s, 1990.

[121] L. Scime, "Bulk Porosity," MATLAB Script, Carnegie Mellon, 2016.

[122] S. Narra, "Melt pool areas and settings in the Arcam S12 process," Internal Report - Carnegie Mellon University, Pittsburgh, PA, 2016.

[123] B. Fisher, "Determination of cooling rate from finite element simulations," Internal MATLAB Script. Carnegie Mellon University, Pittsburgh, PA, 2017.

[124] J. R. Chukkan, M. Vasudevan, S. Muthukumaran, R. R. Kumar and N. Chandrasekhar, "Simulation of Laser Butt Welding of AISI 316L Stainless Steel Sheet Using Various Heat Sources and Experimental Validation," *Journal of Materials Processing Technology,* vol. 219, pp. 48-59, 2015.

[125] Y. S. Touloukian and C. Y. Ho, "Thermophysical Properties of Selected Aerospace Materials, Part II. Thermophysical Properties of Seven Materials," CINDAS-Purdue University, West Lafayette, IN, 1977.

[126] R. H. Bogaard, P. D. Desai, H. H. Li and C. Y. Ho, "Thermophysical Properties of Stainless Steels," *Thermochimica Acta*, vol. 218, pp. 373-393, 1993.

[127] J. W. Elmer, W. H. Giedt and T. W. Eagar, "The Transition from Shallow to Deep Penetration during Electron Beam Welding," *Welding Research*, pp. 167-s to 176-s, 1990.

Appendix 1: Polishing and Etching Procedures

Ti-6Al-4V Polishing and Etching

	Surface	Abrasive/Size	Load (lbs)	Base Speed (rpm) and direction	Time (min:sec)
Polishing	Carbimet Disks	320 Grit SiC water cooled	6	240-300 >>	Until Plane
	UltraPol Cloth	9 µm MetaDi Diamond Suspension	6	120-150 ><	10:00
	Microcloth	0.05 µm Activated MasterMet Colloidal Silica	6	120-150 ><	10:00

\>> denotes complimentary motion between specimen holder and platen
\>< denotes contra motion

Kroll's Etchant

	Chemical	Amount
Etching	Distilled Water	92 ml
	HNO_3	6 ml
	HF	2 ml

Procedure: Swab or submerge samples for 15-30 seconds

Stainless Steel Polishing and Etching

	Surface	Abrasive/Size	Load (lbs)	Base Speed (rpm) and direction	Time (min:sec)
Polishing	Carbimet Disks	320 Grit SiC water cooled	6	300 >>	Until Plane
	UltraPol Cloth	9 µm MetaDi Diamond Suspension	6	150 ><	5:00
	TriDent	3 µm MetaDi Diamond Suspension	6	150 >>	3:00
	MicroCloth	0.05 µm Activated MasterMet Colloidal Silica	6	150 ><	2:00

\>> denotes complimentary motion between specimen holder and platen
\>< denotes contra motion

Oxalic Acid Etchant

	Chemical	Amount
Etching	Distilled Water	10% wt.
	Oxalic Acid	90% wt.

Procedure: Electroetch samples at 1A for 90-120 seconds

<table>
<tr><th colspan="6">IN 718 Polishing and Etching</th></tr>
<tr><th rowspan="6">Polishing</th><th>Surface</th><th>Abrasive/Size</th><th>Load (lbs)</th><th>Base Speed (rpm) and direction</th><th>Time (min:sec)</th></tr>
<tr><td>Carbimet Disks</td><td>240 Grit SiC water cooled</td><td>6</td><td>300 >></td><td>Until Plane</td></tr>
<tr><td>Apex Hercules S</td><td>9 µm MetaDi Diamond Suspension</td><td>6</td><td>150 ><</td><td>5:00</td></tr>
<tr><td>TriDent</td><td>3 µm MetaDi Diamond Suspension</td><td>6</td><td>150 >></td><td>5:00</td></tr>
<tr><td>ChemoMet</td><td>0.05 µm Activated MasterMet Colloidal Silica</td><td>6</td><td>150 ><</td><td>2:00</td></tr>
<tr><td colspan="5">>> denotes complimentary motion between specimen holder and platen
>< denotes contra motion</td></tr>
<tr><th rowspan="6">Etching</th><th colspan="2">Waterless Kallings Etchant</th><td colspan="3"></td></tr>
<tr><th>Chemical</th><th>Amount</th><td colspan="3"></td></tr>
<tr><td>Ethanol</td><td>50 ml</td><td colspan="3"></td></tr>
<tr><td>HCL</td><td>50 ml</td><td colspan="3"></td></tr>
<tr><td>Copper Chloride</td><td>2.5 g</td><td colspan="3"></td></tr>
<tr><td>Procedure:</td><td colspan="4">Swab or submerge samples for 15-30 seconds</td></tr>
</table>

Appendix 2: Melt Pool Width Measurements from LENS Ti-6Al-4V Experiments

<table>
<tr><th colspan="6">Laser Powder Feed Process Melt Pool Width (Constant 3 gpm Feed Rate)</th></tr>
<tr><th>Power (W)</th><th>Velocity (in/min)</th><th>"Best Guess" Width from Cross Section (mm)</th><th>Width Uncertainty from Cross Section (mm)</th><th>Average Width from Above (mm)</th><th>Standard Deviation from above (mm)</th></tr>
<tr><td>450</td><td>15</td><td>1.85</td><td>1.67-2.05</td><td>1.98</td><td>0.08</td></tr>
<tr><td>450</td><td>25</td><td>1.63</td><td>1.47-1.85</td><td>1.72</td><td>0.06</td></tr>
<tr><td>450</td><td>35</td><td>1.49</td><td>1.29-1.67</td><td>1.57</td><td>0.05</td></tr>
<tr><td>450</td><td>45</td><td>1.38</td><td>1.24-1.63</td><td>1.44</td><td>0.07</td></tr>
<tr><td>350</td><td>15</td><td>1.48</td><td>1.32-1.57</td><td>1.45</td><td>0.07</td></tr>
<tr><td>350</td><td>25</td><td>1.31</td><td>1.20-1.52</td><td>1.34</td><td>0.05</td></tr>
<tr><td>350</td><td>35</td><td>1.24</td><td>1.07-1.38</td><td>1.22</td><td>0.04</td></tr>
<tr><td>350</td><td>45</td><td>1.12</td><td>0.98-1.25</td><td>1.13</td><td>0.04</td></tr>
<tr><td>250</td><td>15</td><td>1.14</td><td>1.13-1.31</td><td>1.12</td><td>0.08</td></tr>
<tr><td>250</td><td>25</td><td>1.03</td><td>0.97-1.11</td><td>1.01</td><td>0.04</td></tr>
<tr><td>250</td><td>35</td><td>0.95</td><td>0.87-1.06</td><td>0.94</td><td>0.04</td></tr>
<tr><td>250</td><td>45</td><td>0.91</td><td>0.85-1.01</td><td>0.86</td><td>0.03</td></tr>
</table>

150	15	0.68	0.66-0.76	0.66	0.05
150	25	0.66	0.64-0.80	0.61	0.03
150	35	0.59	0.53-0.61	0.54	0.03
150	45	0.51	0.48-0.57	0.47	0.02

Laser Powder Feed Process Melt Pool Width (Scaled Feed Rate)

Power (W)	Velocity (in/min)	"Best Guess" Width from Cross Section (mm)	Width Uncertainty from Cross Section (mm)	Average Width from Above (mm)	Standard Deviation from above (mm)
450	15	1.87	1.79-2.03	1.82	0.05
450	25	1.61	1.49-1.79	1.60	0.03
450	35	1.43	1.32-1.54	1.46	0.03
450	45	1.30	1.20-1.47	1.36	0.04
350	15	1.53	1.42-1.72	1.50	0.05
350	25	1.33	1.24-1.52	1.36	0.03
350	35	1.19	1.06-1.31	1.23	0.05
350	45	1.15	1.11-1.30	1.13	0.03
250	15	1.14	1.05-1.29	1.10	0.03
250	25	1.02	0.94-1.10	1.00	0.03
250	35	0.92	0.82-1.01	0.90	0.02
250	45	0.86	0.79-0.96	0.86	0.02
150	15	0.67	0.66-0.73	0.63	0.02
150	25	0.62	0.62-0.75	0.58	0.02
150	35	0.54	0.49-0.61	0.53	0.02
150	45	0.51	0.46-0.60	0.50	0.02

Laser Powder Feed Process Melt Pool Width (No Added Material)

Power (W)	Velocity (in/min)	"Best Guess" Width from Cross Section (mm)	Uncertainty from Cross Section (mm)	Average Width from Above (mm)	Standard Deviation from above (mm)
450	15	1.77	1.65-1.98	1.88	0.06
450	25	1.56	1.49-1.76	1.62	0.05
450	35	1.44	1.31-1.59	1.45	0.08
450	45	1.33	1.21-1.45	1.34	0.12
350	15	1.49	1.35-1.67	1.50	0.05
350	25	1.33	1.23-1.49	1.35	0.03
350	35	1.22	1.13-1.33	1.26	0.06
350	45	1.15	1.03-1.29	1.16	0.07

250	15	1.13	1.00-1.24	1.16	0.02
250	25	1.01	0.96-1.13	0.99	0.03
250	35	0.92	0.84-1.04	0.93	0.06
250	45	0.87	0.80-0.97	0.89	0.07
150	15	0.71	0.59-0.84	0.69	0.02
150	25	0.67	0.44-0.72	0.66	0.03
150	35	0.62	0.42-0.79	0.55	0.04
150	45	0.57	0.41-0.71	0.52	0.04

Appendix 3: Spot size effects on melt pool geometry - Experimental measurements compared with simulation results

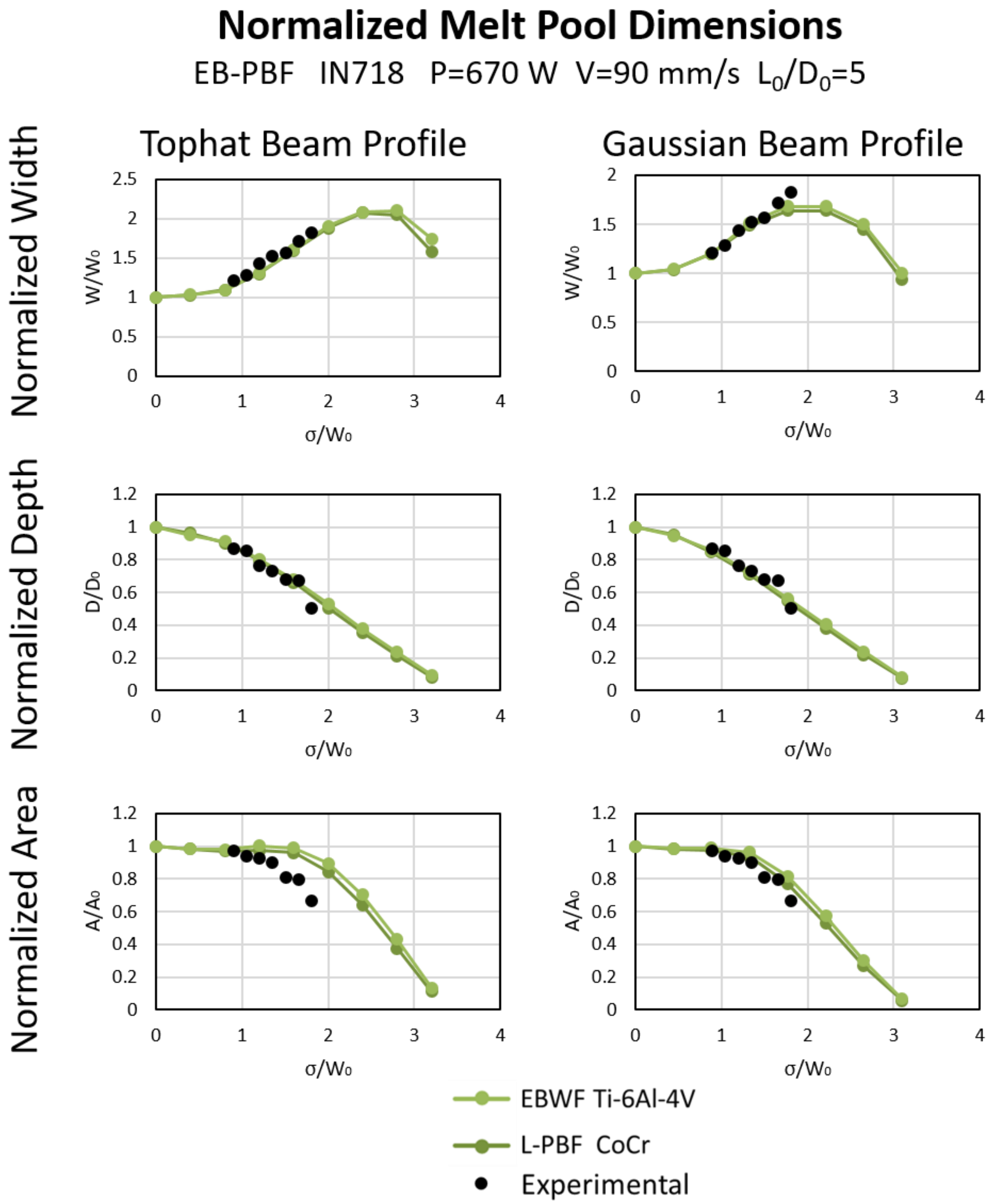

Appendix Figure 1: Experimental and simulation normalized melt pool dimensions vs normalized spot size

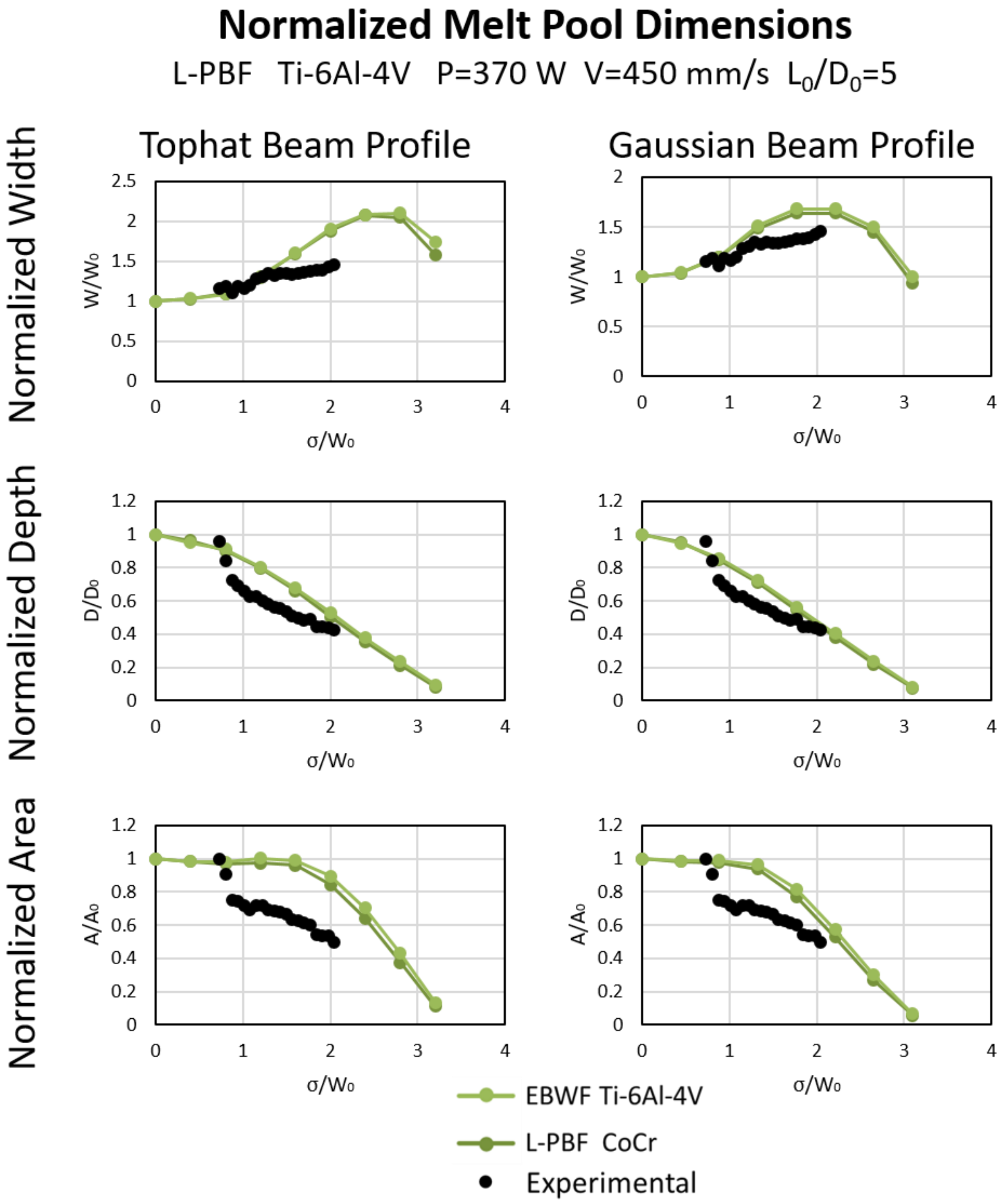

Appendix Figure 2: Experimental and simulation normalized melt pool dimensions vs normalized spot size

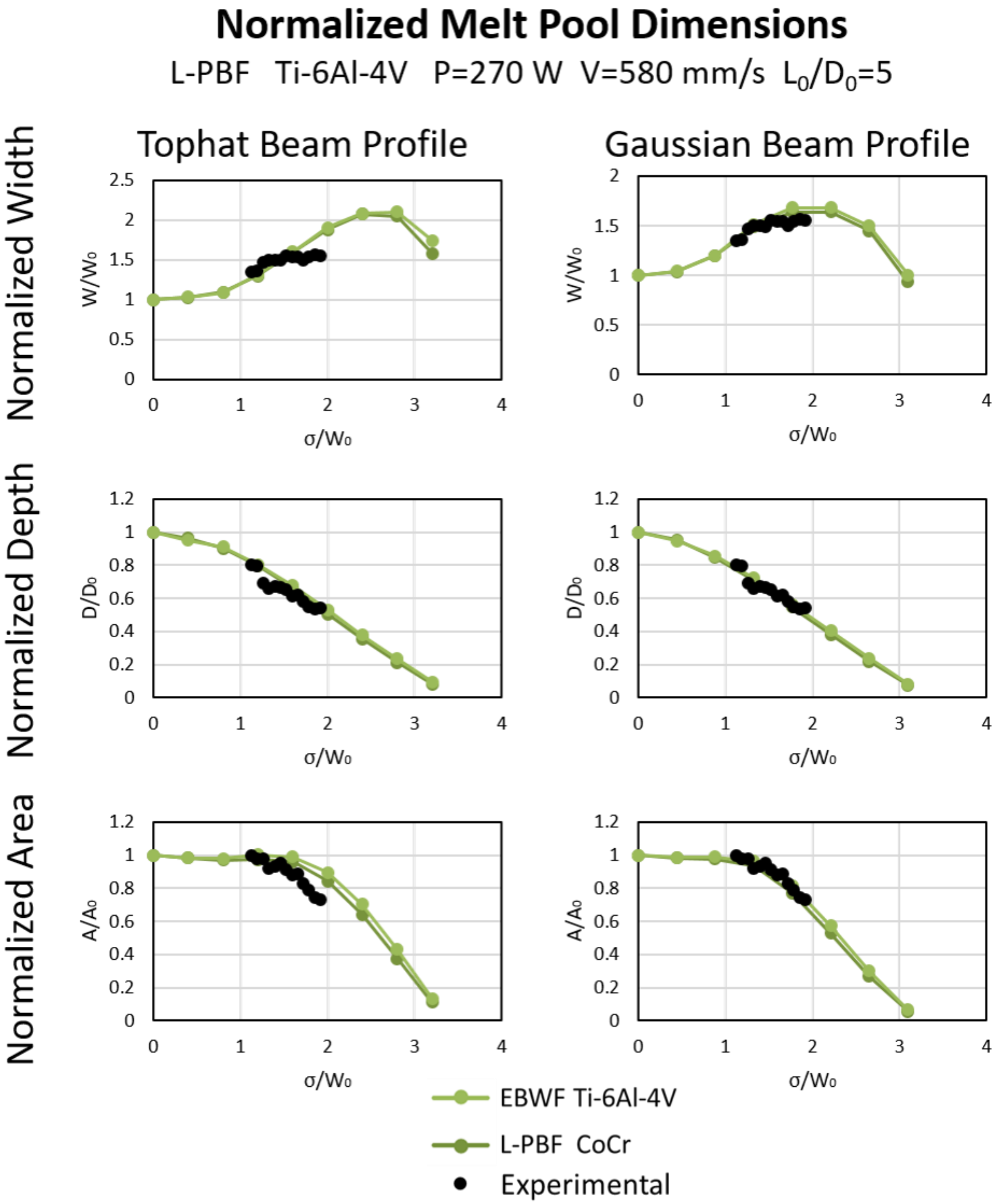

Appendix Figure 3: Experimental and simulation normalized melt pool dimensions vs normalized spot size

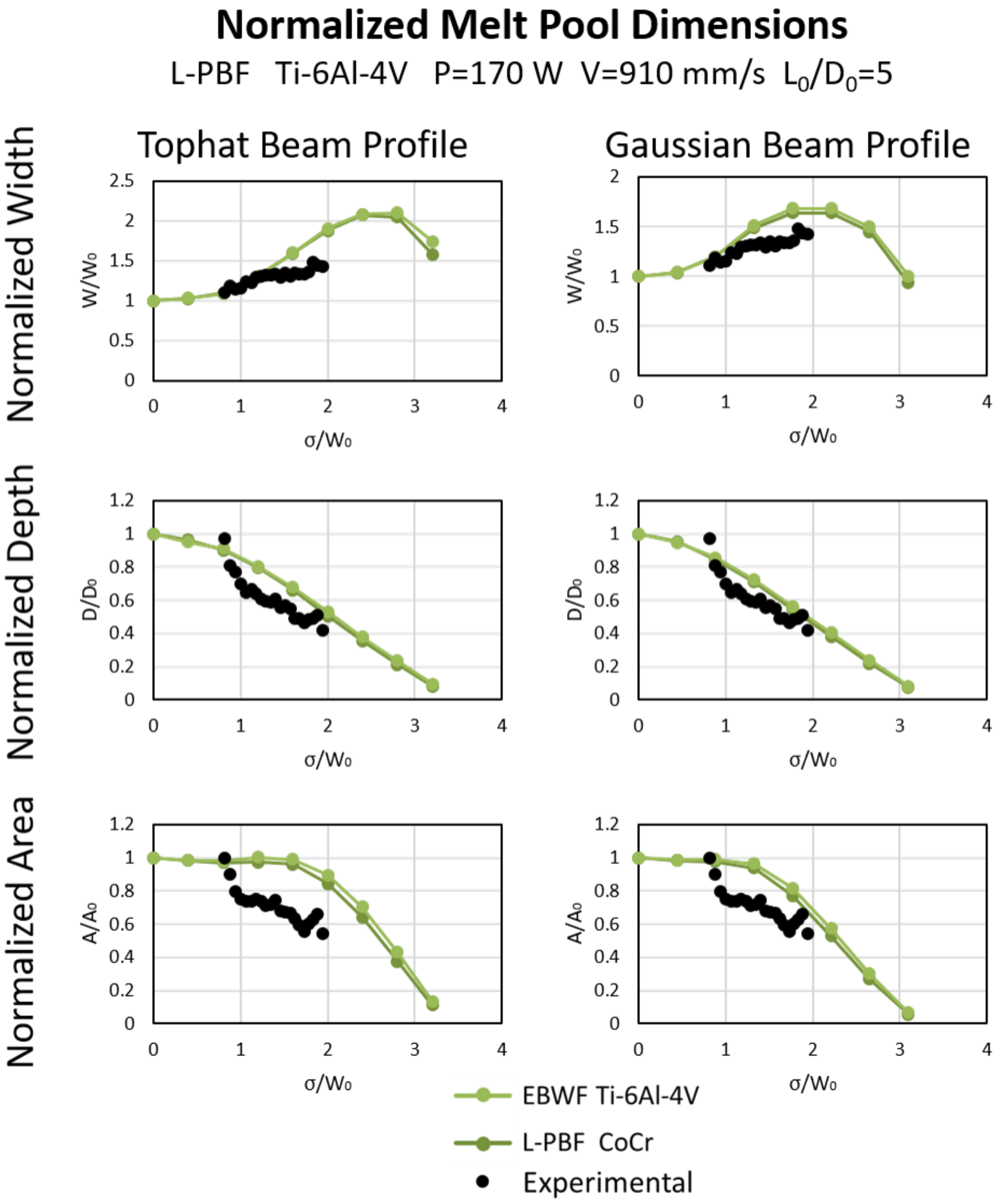

Appendix Figure 4: Experimental and simulation normalized melt pool dimensions vs normalized spot size

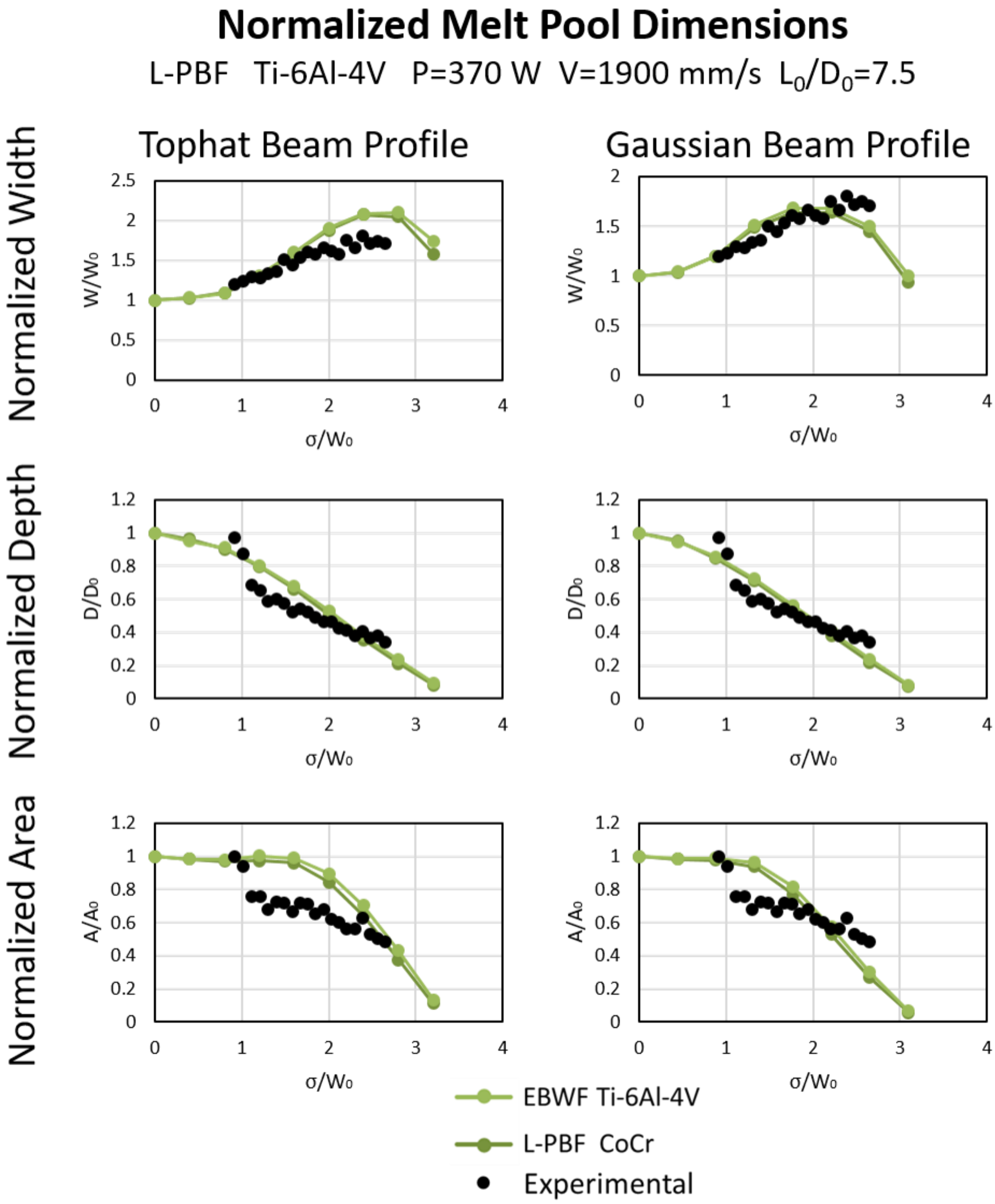

Appendix Figure 5: Experimental and simulation normalized melt pool dimensions vs normalized spot size

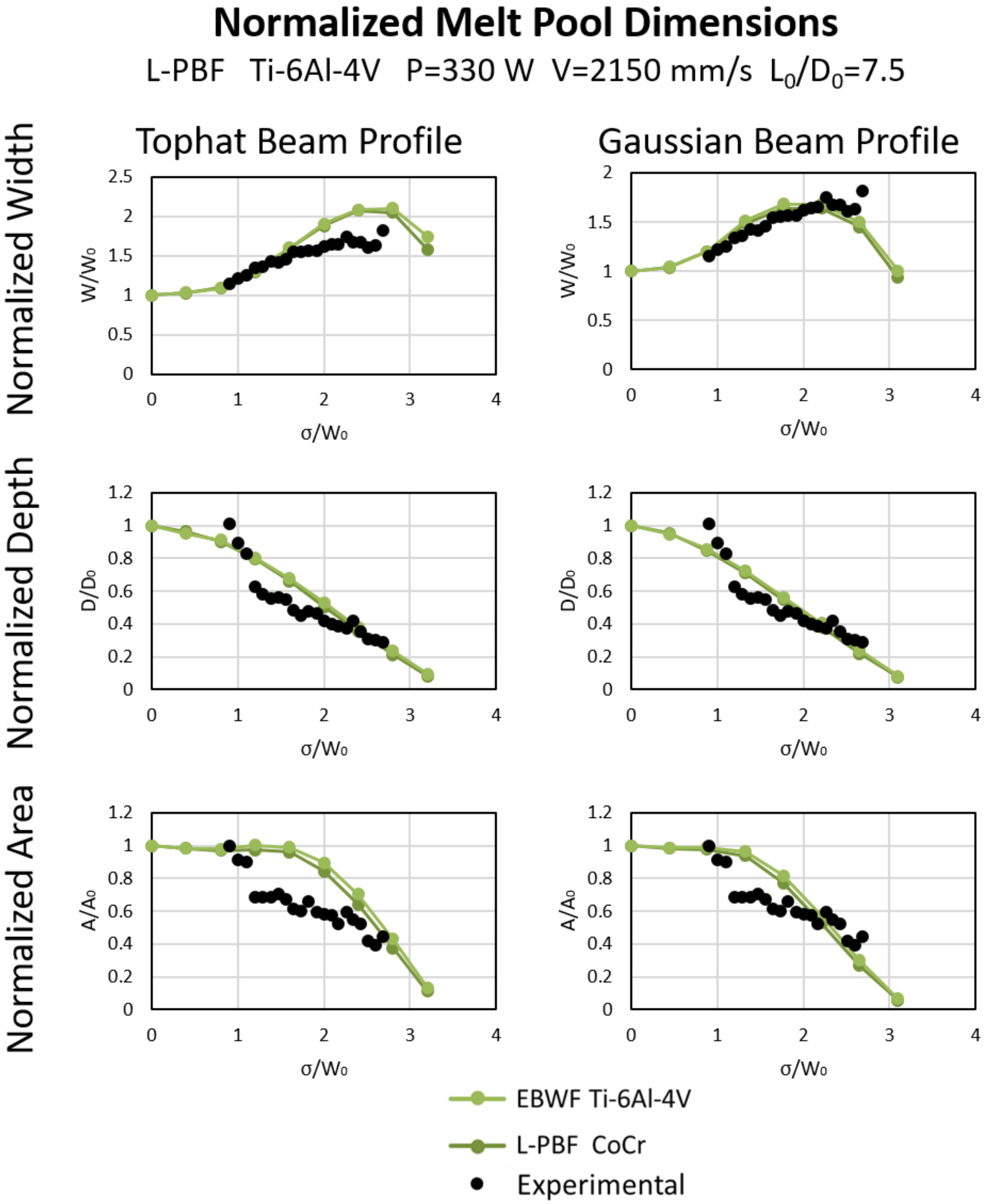

Appendix Figure 6: Experimental and simulation normalized melt pool dimensions vs normalized spot size

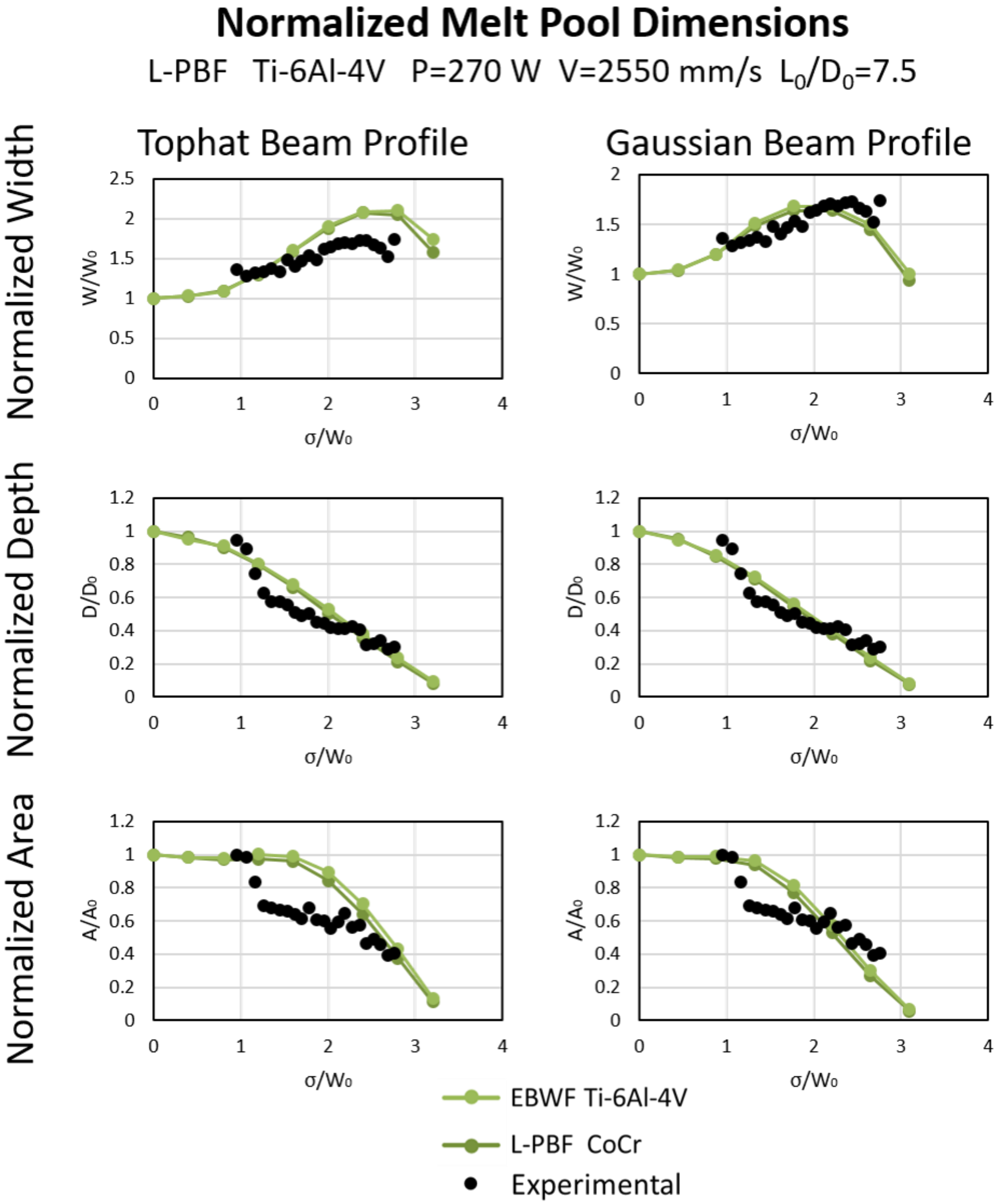

Appendix Figure 7: Experimental and simulation normalized melt pool dimensions vs normalized spot size

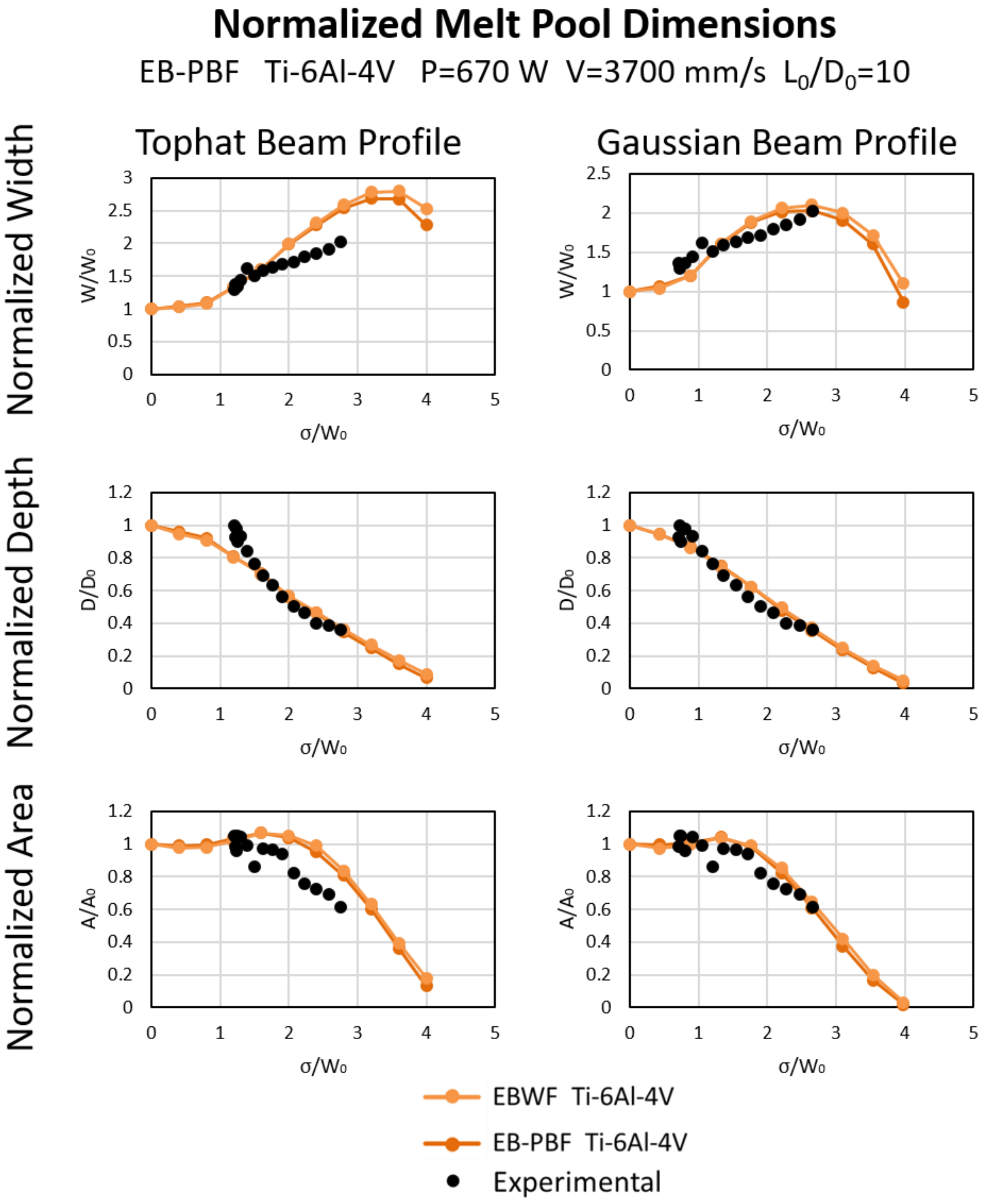

Appendix Figure 8: Experimental and simulation normalized melt pool dimensions vs normalized spot size

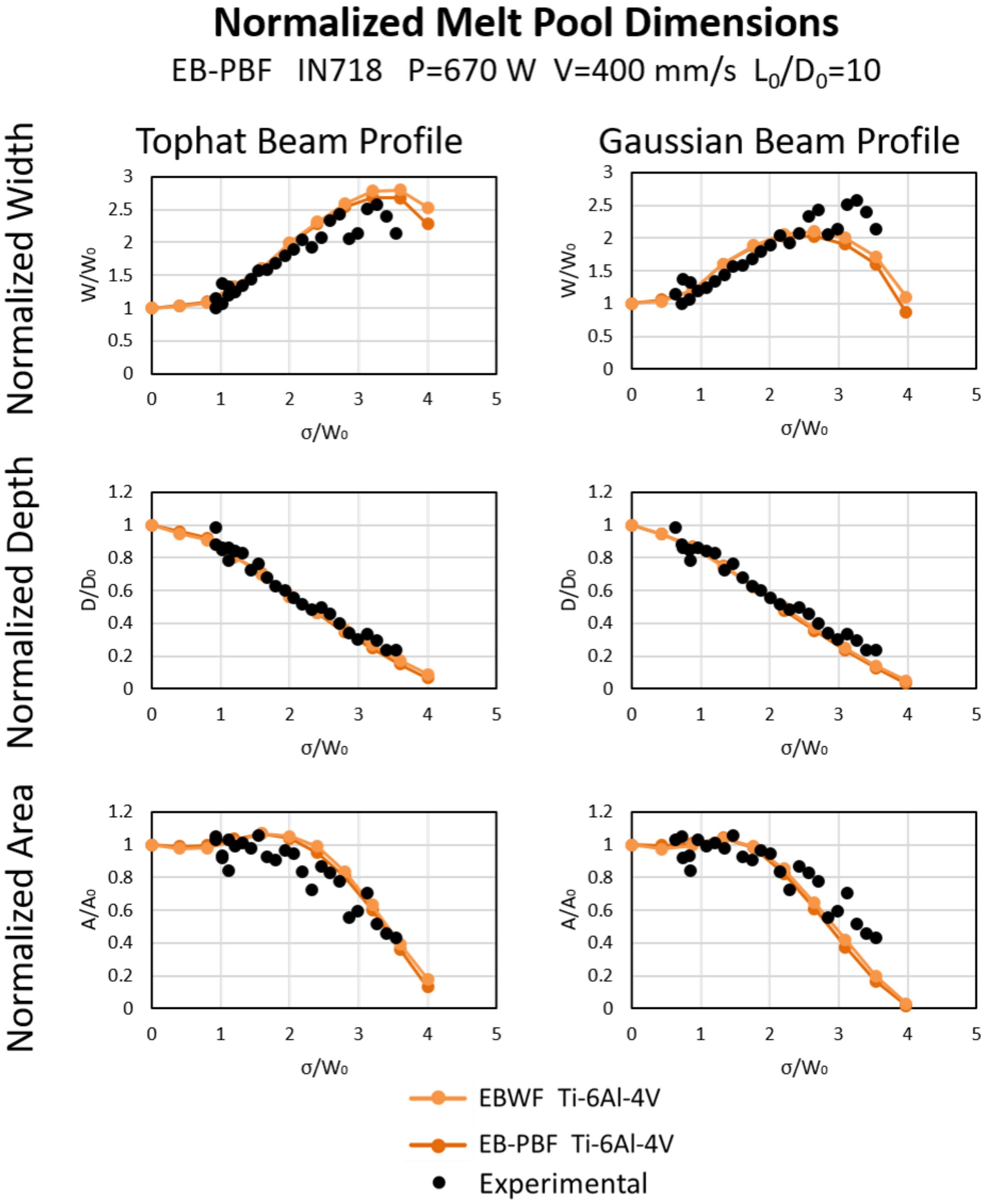

Appendix Figure 9: Experimental and simulation normalized melt pool dimensions vs normalized spot size

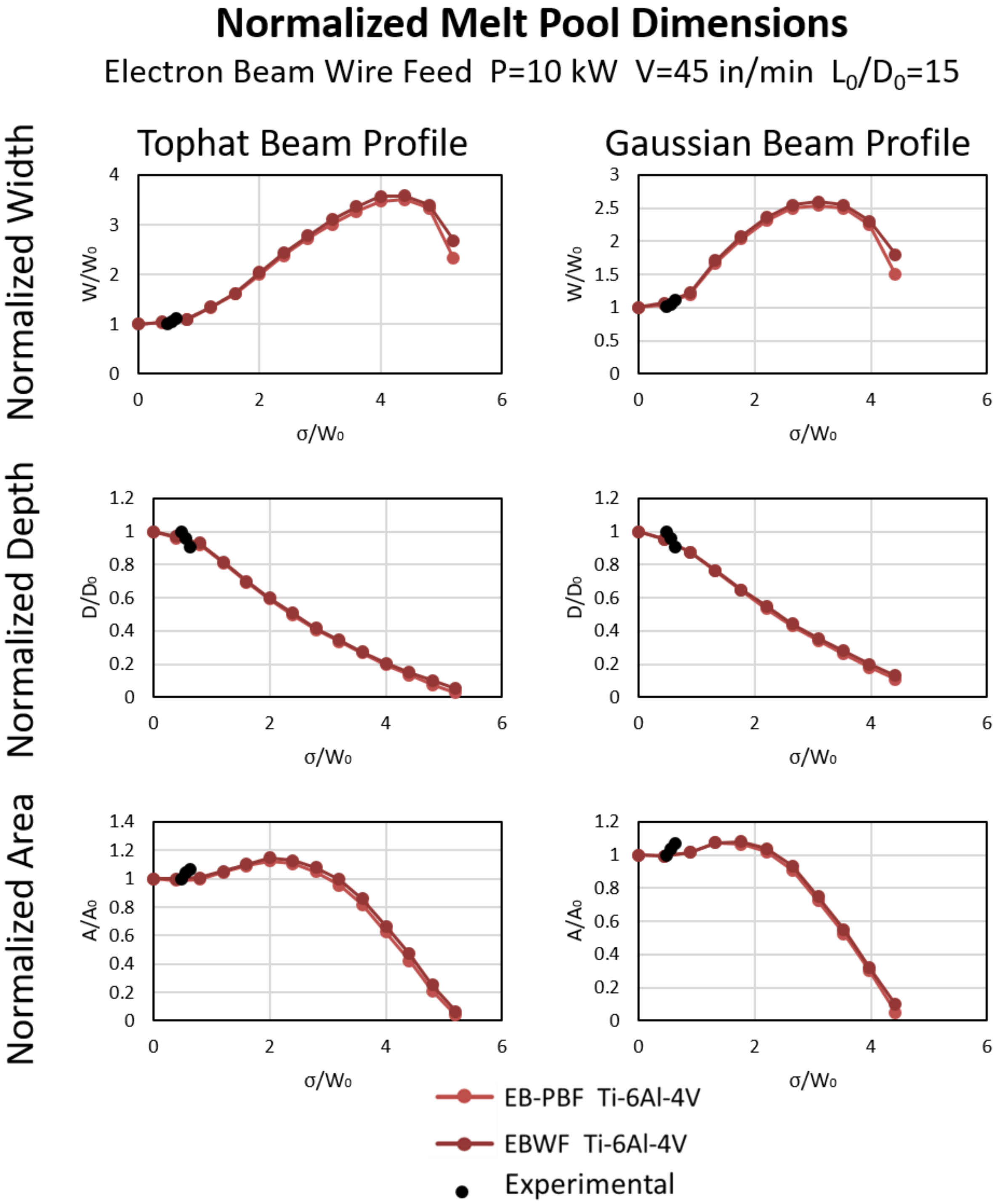

Appendix Figure 10: Experimental and simulation normalized melt pool dimensions vs normalized spot size

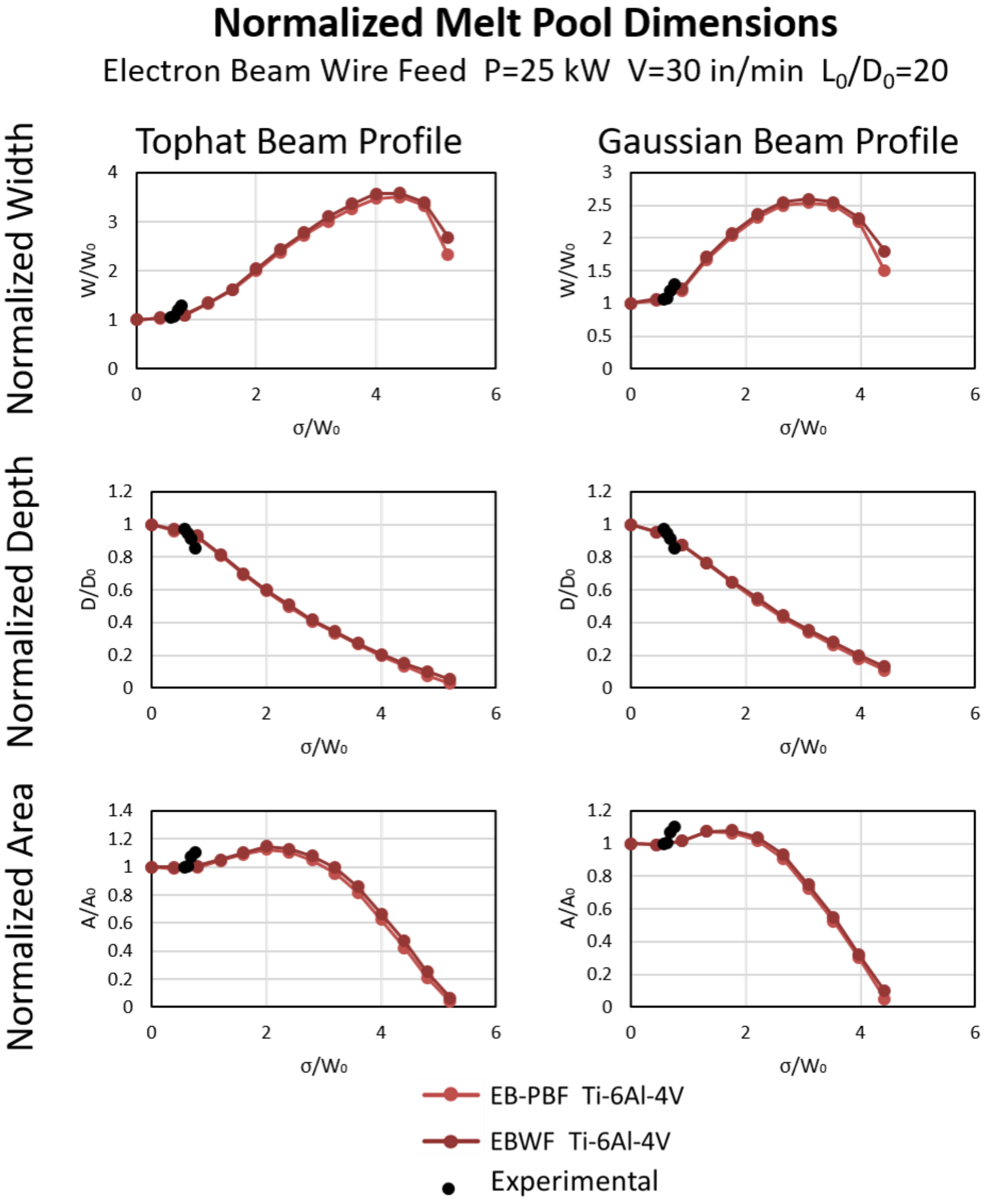

Appendix Figure 11: Experimental and simulation normalized melt pool dimensions vs normalized spot size

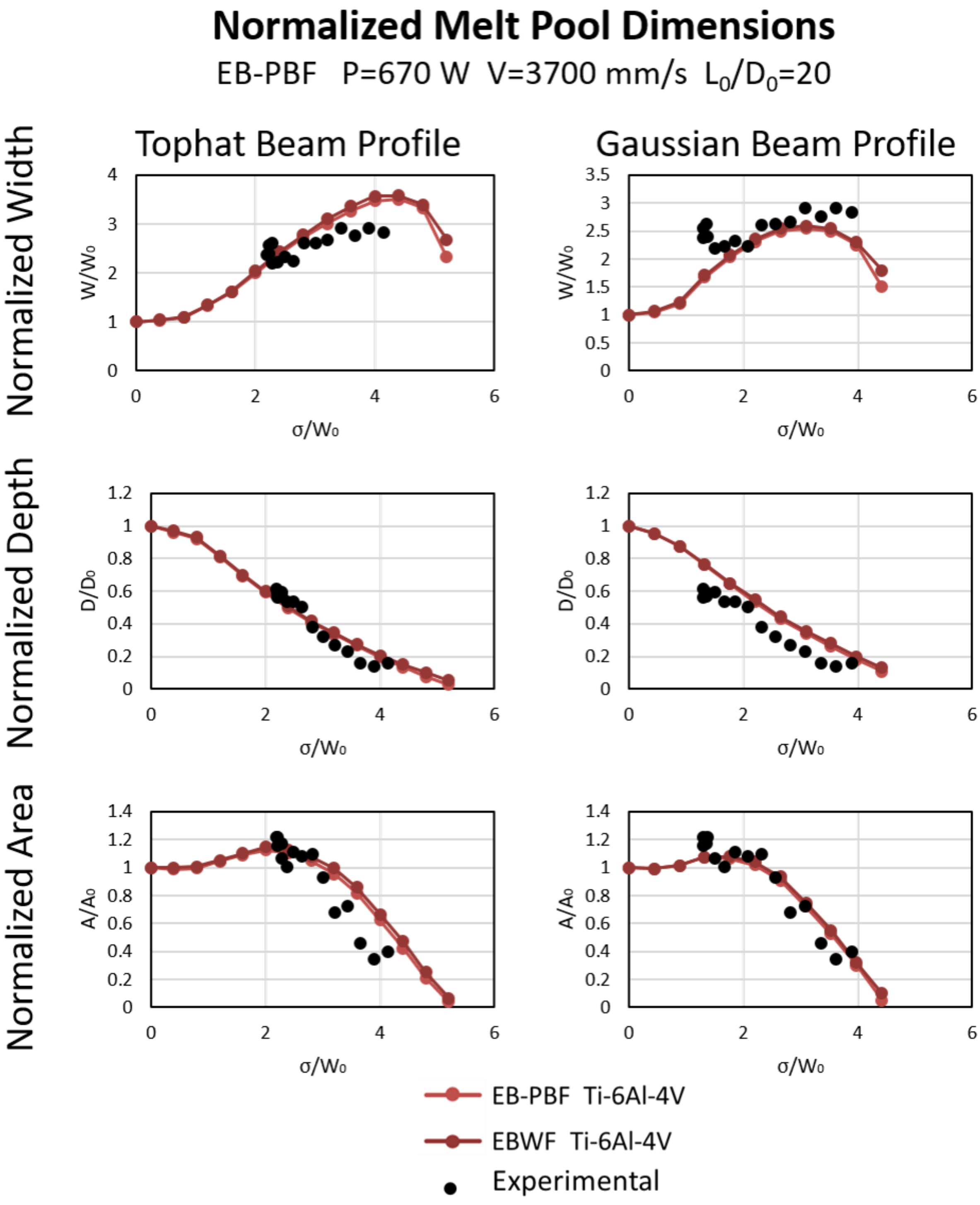

Appendix Figure 12: Experimental and simulation normalized melt pool dimensions vs normalized spot size

Appendix 4: Laser beam measurements in the EOS M 290 process

Laser measurements were taken by Sean Goodrich using Primes FocusMonitor equipment that uses a rotating pinhole to direct segments of the beam to a detector. The D86 laser measurement method is used to provide the beam diameter.

Measurements at 40 W:

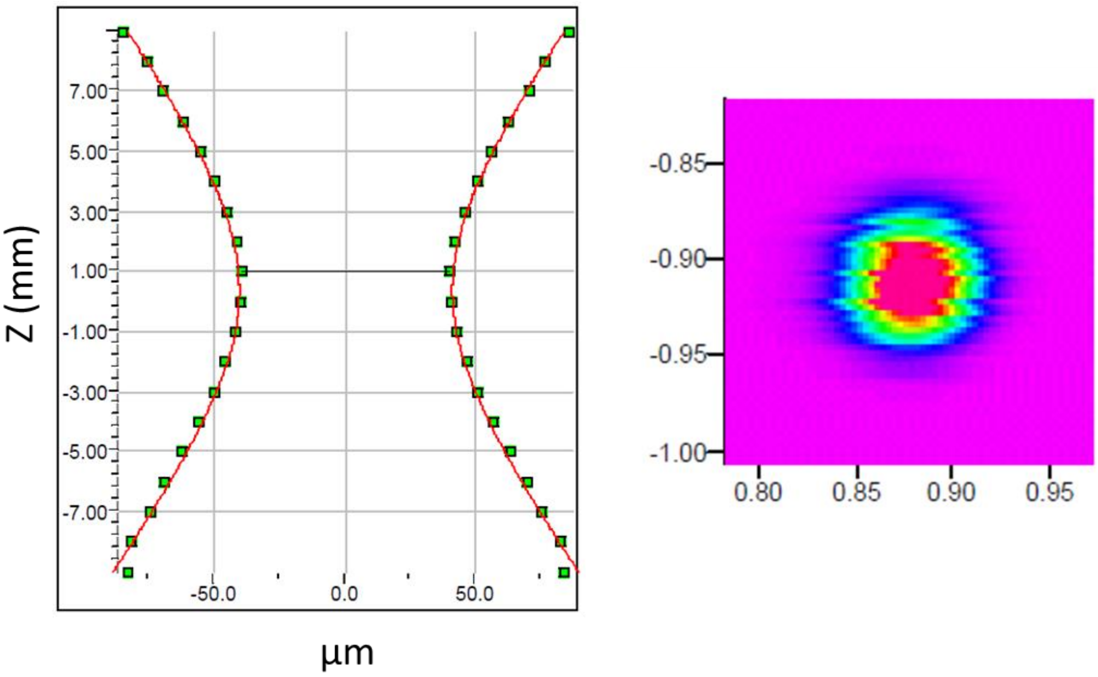

Appendix Figure 13: Beam Measurements taken in the EOS M 290 process at 40 W

Focus Radius: 41.608 µm
Focus radius X: 42.874 µm
Focus Radius Y: 40.299 µm
K: 0.952
Kx: 0.917
Ky: 0.990
M2: 1.05
M2x: 1.09
M2y: 1.01
Position Z: 0.34 mm
Position Z(X): 0.34 mm

Position Z(Y): 0.342 mm
Rayleigh Length: 4.794 mm
Rayleigh Length X: 4.905 mm
Rayleigh Length Y: 4.68 mm
Beam Parameter: 0.4 mm*mrad
Beam Parameter X: 0.4 mm*mrad
Beam Parameter Y: 0.3 mm*mrad
Focus Symmetry (rx/ry): 1.06
Astigmatic difference: -0.00

Measurements at 200 W:

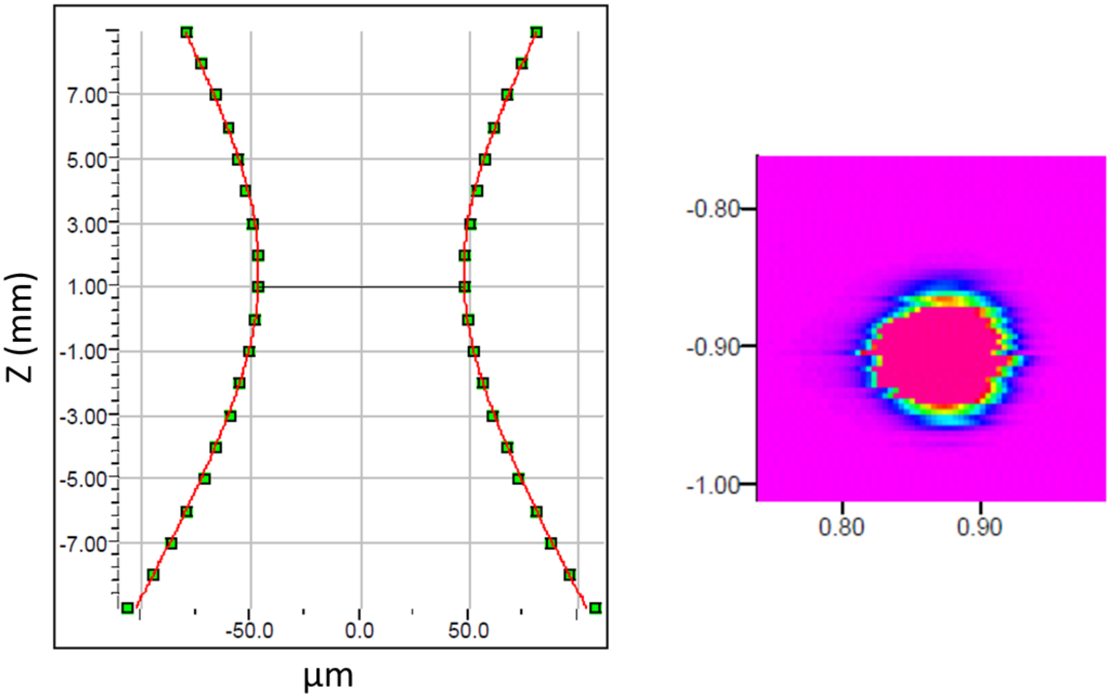

Appendix Figure 14: Beam Measurements taken in the EOS M 290 process at 200 W

Focus Radius: 52.363 µm
Focus radius X: 55.445 µm
Focus Radius Y: 49.067 µm
K: 0.724
Kx: 0.701
Ky: 0.756
M2: 1.38
M2x: 1.43

M2y: 1.32
Position Z: 1.59 mm
Position Z(X): 1.63 mm
Position Z(Y): 1.56 mm
Rayleigh Length: 5.778 mm
Rayleigh Length X: 6.266 mm
Rayleigh Length Y: 5.29 mm
Beam Parameter: 0.5 mm*mrad
Beam Parameter X: 0.5 mm*mrad
Beam Parameter Y: 0.5 mm*mrad
Focus Symmetry (rx/ry): 1.13
Astigmatic difference: 0.02

Appendix 5: Cross section changes at selected power-velocity combinations in the ProX 200 Process

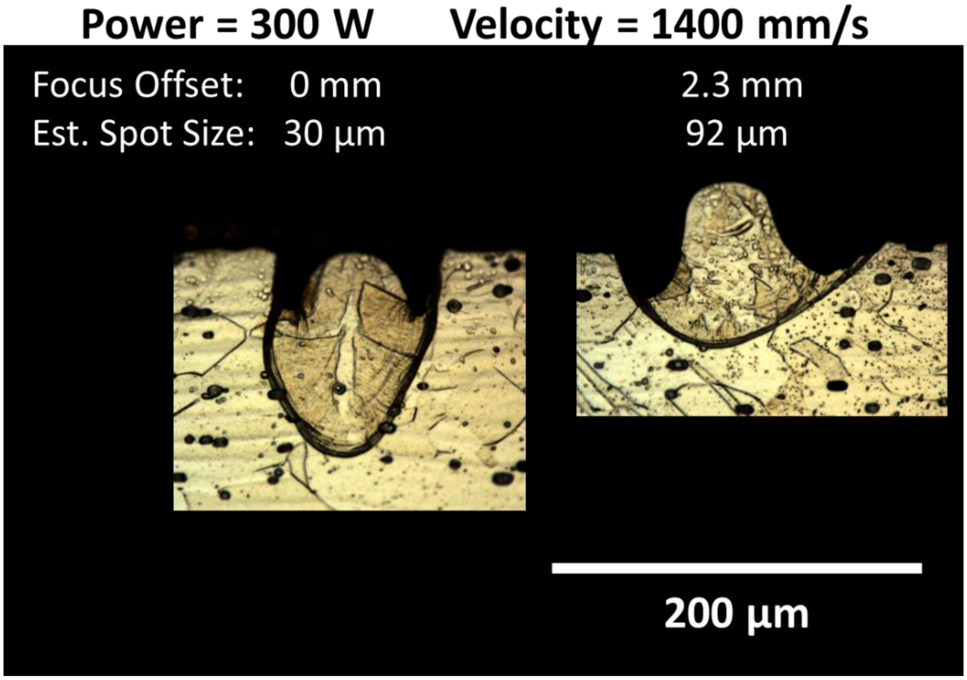

Appendix Figure 15: Melt pools deposited at nominal (left) and expanded (right) spot size at 300 W and 1400 mm/s for 316L stainless steel in the ProX 200 L-PBF process

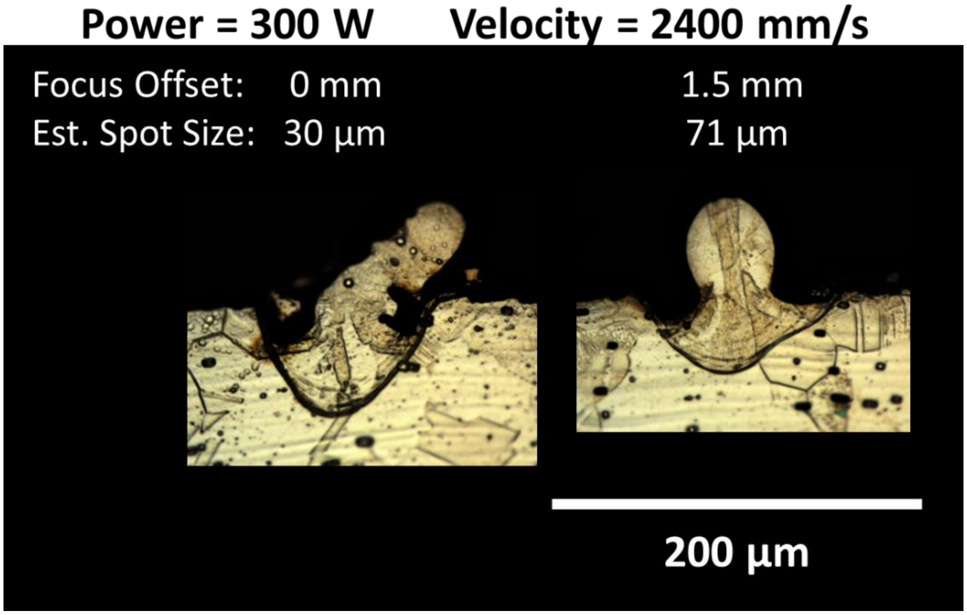

Appendix Figure 16: Melt pools deposited at nominal (left) and expanded (right) spot size at 300 W and 2400 mm/s for 316L stainless steel in the ProX 200 L-PBF process

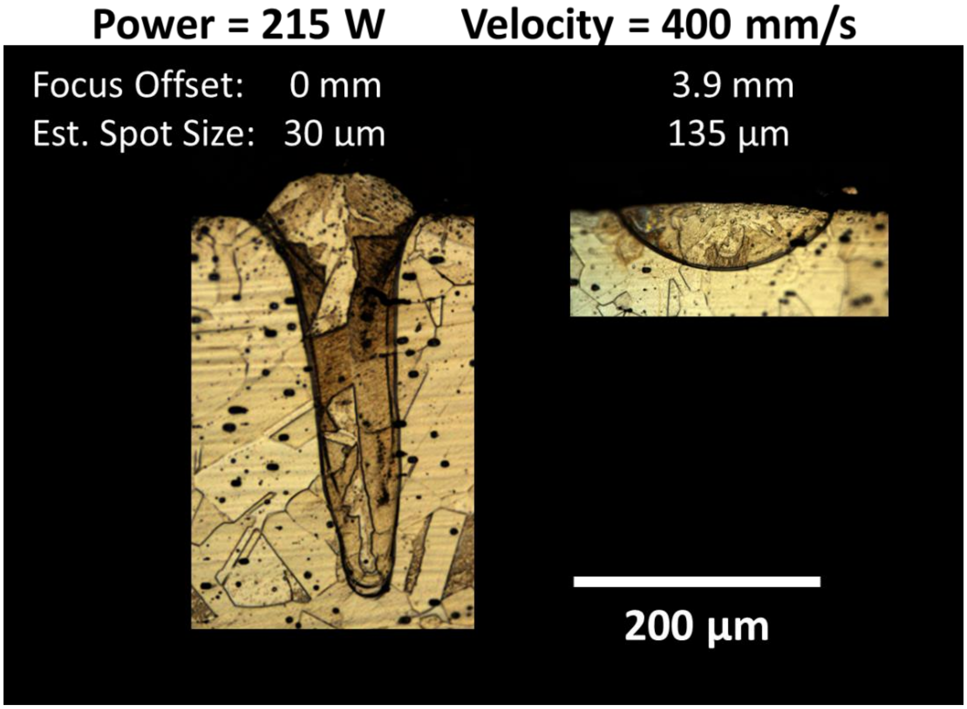

Appendix Figure 17: Melt pools deposited at nominal (left) and expanded (right) spot size at 215 W and 400 mm/s for 316L stainless steel in the ProX 200 L-PBF process

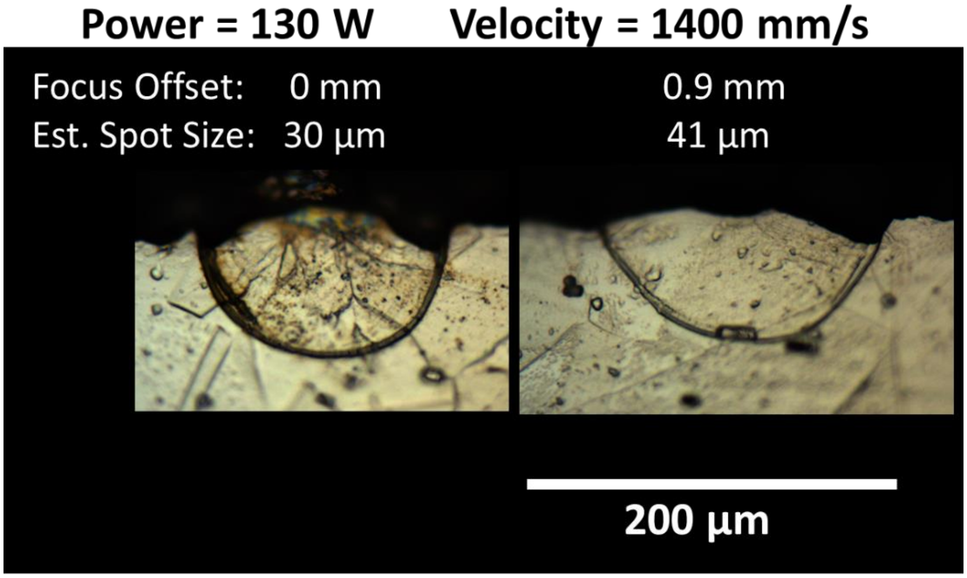

Appendix Figure 18: Melt pools deposited at nominal (left) and expanded (right) spot size at 130 W and 1400 mm/s for 316L stainless steel in the ProX 200 L-PBF process

Appendix 6: Minimum spot sizes to avoid keyholing throughout power-velocity space in the ProX 200 process

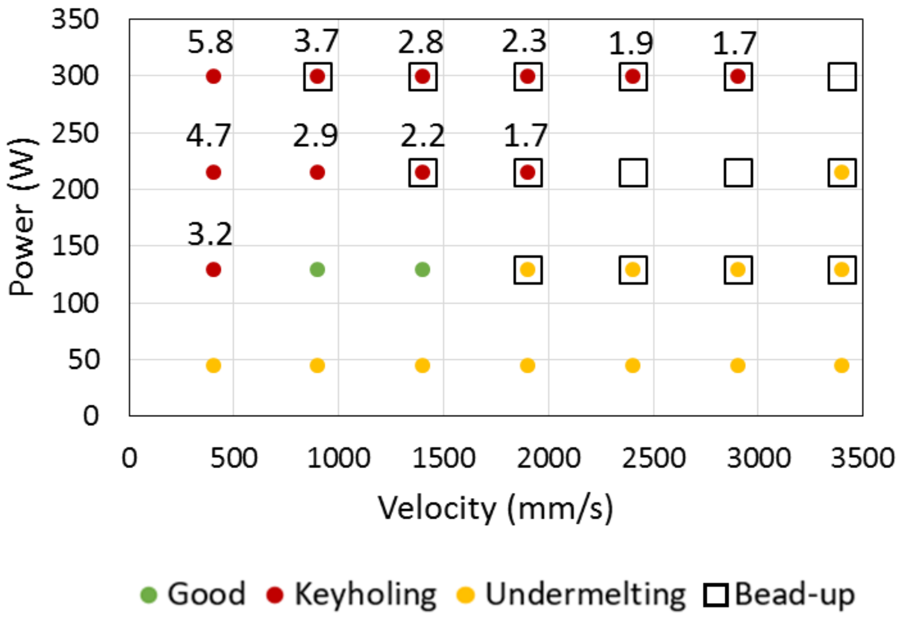

Appendix Figure 19: Focus offset settings (mm) in the ProX200 L-PBF process for 316L stainless steel to prevent keyhole mode melting in melt pools where it was identified at nominal settings

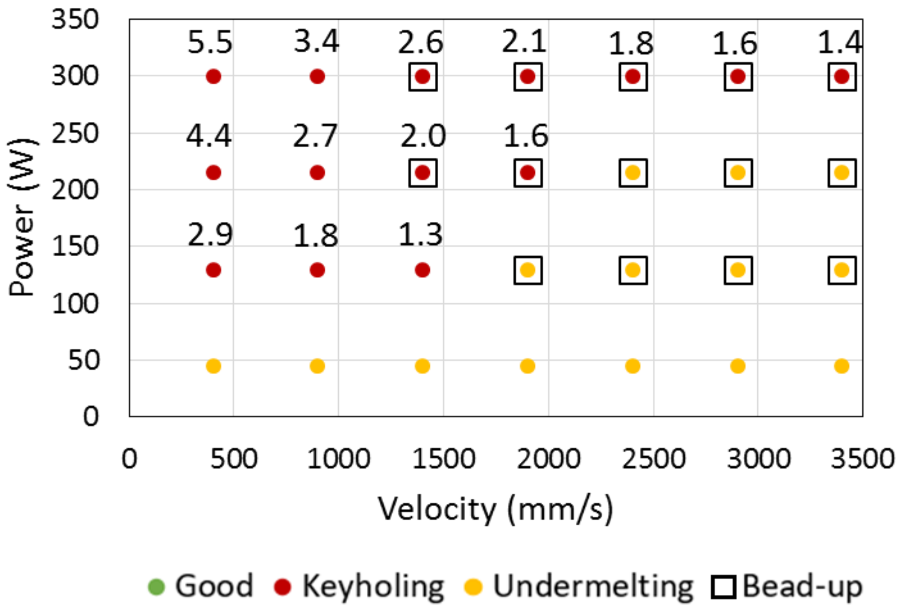

Appendix Figure 20: Focus offset settings (mm) in the ProX200 L-PBF process for 17-4 stainless steel to prevent keyhole mode melting in melt pools where it was identified at nominal settings

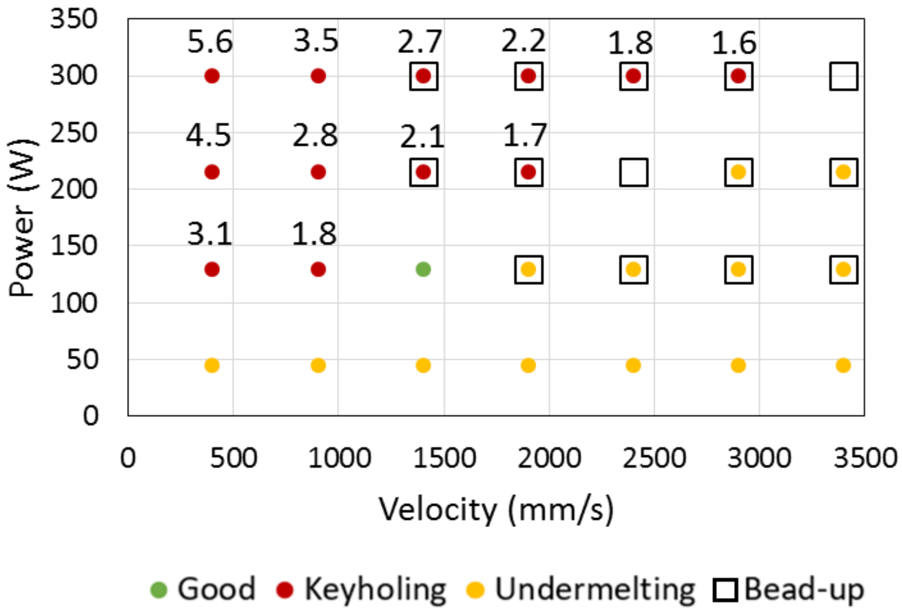

Appendix Figure 21: Focus offset settings (mm) in the ProX200 L-PBF process for 304 stainless steel to prevent keyhole mode melting in melt pools where it was identified at nominal settings